

Optical and Electronic Properties of PbS Colloidal Nanocrystals

Umaima Elfurawi, MSci

*Thesis submitted to the University of Nottingham
for the degree of Doctor of Philosophy*

January 2012

Contents

1	Introduction	1
2	Band structure properties of bulk PbS and PbS quantum dots	5
2.1	Properties of bulk lead sulphide (PbS)	6
2.2	Band Gap Tuning and Quantum Confinement	10
2.2.1	Density of states	10
2.2.2	Exciton	11
2.2.3	Quantum Confinement in Quantum Dots	13
2.3	Colloidal PbS QDs	17
3	Experimental setup and techniques	20
3.1	Photoluminescence (PL)	20
3.1.1	Photoluminescence and absorption setup	22
3.2	Micro-PL	24
3.3	Magneto-PL and circular polarized PL	26
3.4	Current-voltage characteristics	27
3.5	Microscopic techniques	28
3.5.1	Atomic Force Microscopy (AFM)	28
3.5.2	Transmission Electron Microscopy (TEM)	30
3.5.3	Scanning Electron Microscopy (SEM)	31
3.5.4	Energy-dispersive X-ray spectroscopy (EDX)	32

4	Samples	33
4.1	Synthesis of Colloidal PbS QDs	33
4.2	Ordering of QDs	37
4.3	Samples for conductivity studies	40
4.4	Temperature dependence of the QD PL emission	43
5	Thermal annealing of PbS QDs	49
5.1	QD morphology	49
5.2	QD photoluminescence emission	53
5.3	Temperature dependence of the QD PL emission	57
6	Magneto-photoluminescence	61
6.1	Exciton fine structure in PbS QDs	61
6.2	Zeeman Splitting and g -factor	62
6.3	Polarization and selection rules	63
6.3.1	Spin Relaxation and Carrier Recombination Time	64
6.4	The strength of carrier confinement in PbS QDs	66
6.5	Circular polarization of the QD PL emission	68
6.5.1	Resonant excitation of the QDs	73
7	Electronic Transport in PbS QDs	75
7.1	Thin films of PbS QDs	75
7.1.1	Comparing devices with different electrode spacing	79
7.1.2	Space charge and Frenkel effect	81
7.1.3	Current noise	84
7.1.4	Photoresponse	84
7.2	Titanium Dioxide impregnated with PbS QDs	86
7.2.1	Morphological and optical properties	88

7.2.2	Photovoltaic effect	90
7.2.3	Summary	94
8	Conclusions and Prospects for Future work	95
	Bibliography	98

List of Figures

2.1	Calculated band structure of PbS at 73K	7
2.2	a) Rock salt crystal structure. b) First Brillouin zone of the lattice of rock salt crystals	9
2.3	A schematic representation of the DOS in 3D, 2D, 1D and 0D. .	11
2.4	Energy levels of an exciton in a direct band gap semiconductor .	12
2.5	A schematic of a single colloidal QD and a diagram of the energy levels of electrons and holes in a QD	14
2.6	PbS band gap as a function of particle diameter	16
3.1	A schematic diagram showing the photoluminescence process in a direct band gap material	21
3.2	Schematic of the experimental apparatus used for optical studies	24
3.3	a) Horiba Jobin Yuon Lab. Ram. setup. b) Schematic showing the main optics in the micro-PL system	25
3.4	Schematic of a liquid helium cooled magneto cryostat with magnetic fields up to 16 T	26
3.5	Electric circuits used to study a) transport in PbS film samples and b) TiO ₂ /PbS films	28
3.6	HRTEM image of a PbS QD.	30
4.1	a) RT PL spectra of different PbS QDs. b) PL and absorption spectra of PbS QDs	34
4.2	TEM image of Aft-QDs drop-cast on a carbon grid	39
4.3	Optical microscopy images of Aft-QDs drop-cast on a glass substrate.	40

4.4	Optical microscopy image of Aft-PbS QDs and the corresponding micro-PL map.	41
4.5	Photograph of a device with QDs between adjacent electrodes	41
4.6	a) Schematic of a device structure based on PbS/TiO ₂ . b) TiO ₂ films with and without PbS QDs	42
4.7	a) PL spectra at various T , b) T -dependence of the PL peak position, energy peak shift and the FWHM of the Aft-QD PL-emission.	44
4.8	a) PL spectra at various T , b) T -dependence of the PL peak position, energy peak shift and the FWHM of the DHLA-QD PL emission.	47
5.1	TEM images of thiol-capped PbS QDs before and after annealing	50
5.2	A sequence of TEM images for a film of thiol-capped PbS QDs annealed <i>in situ</i> on a carbon grid at various T_A	51
5.3	A HRTEM image of one of the interconnected PbS QDs annealed at $T_A = 90^\circ\text{C}$	53
5.4	Normalized PL spectra of a PbS QD sample annealed at different T_A for $t_A = 1$ h	54
5.5	QD diameter as a function of the annealing temperature, T_A	56
5.6	Normalized PL spectra of as grown and annealed PbS QDs ($T_A = 60^\circ\text{C}$, $t_A = 1$ h) at different lattice temperatures	57
6.1	Schematic of single particle energy states and excitonic states	62
6.2	Low temperature unpolarized PL spectra at $B=0$ and $B=30$ T for PbS QDs with average diameter $d=5$ nm and 9nm.	67
6.3	Circular-polarized PL emission acquired at 7.5 K and various magnetic fields for PbS QDs with average diameter $d= 4$ nm.	69
6.4	a) B -dependence of the DCP of the QD PL emission at low temperature, b) Dependence of g_X on the average QD diameter d	70
6.5	B dependence of the DCP at various energies for one of our PbS QD samples ($T= 4.2$ K).	71
6.6	PL spectra for resonant and non resonant excitation at low T and RT for QDs with $d = 4$ nm.	74

7.1	$I(V)$ characteristics of a PbS QDs sample a) 4K and b) 295K	77
7.2	Log-log plots of the current versus electric field $F = V/L$ for three samples of different gap spacing	79
7.3	Temperature dependence of the current at different biases for a PbS thin film on a 1 μm gap device.	80
7.4	Poole-Frenkel effect	81
7.5	Current density J versus applied voltage for the 1 μm gap device at different T	82
7.6	A comparison between $I(V)$ loops at $T= 237$ K and $T=4$ K. b) Temperature dependence of I and of ΔI on $1/k_B T$	85
7.7	a) PL intensity and absorption spectra of PbS/TiO ₂ film. b) TEM image of a cross-section of a PbS/TiO ₂ film	89
7.8	$J(V)$ characteristics of the PbS/TiO ₂ device in the dark and under laser illumination	90
7.9	T -dependence of the differential conductance	92

List of Tables

2.1	Bulk properties of PbS	8
2.2	Percentage of atoms on the surface of CdSe and PbSe QDs for given values of R/R_{ex}	15
4.1	Molar ratio, PL peak position of thiol-PbS or Aft-PbS QDs and their corresponding particle diameter d and density.	36
4.2	Values of Γ_{inh} and Γ_{LO}	48

Abstract

This thesis describes the optical and electrical properties of colloidal PbS nanocrystals synthesized in aqueous solution and comprising different capping ligands and/or matrices.

Post-synthesis thermal annealing of thiol-capped PbS colloidal quantum dots (QDs) is discussed and shown to provide a novel means of tailoring the morphological and electronic properties of the QDs. Two different regimes are reported: at low annealing temperatures ($< 80^\circ\text{C}$), the annealing provides a simple strategy for controlling and narrowing the QD size distribution and photoluminescence emission. At higher annealing temperatures, the displacement of the thiol-ligands promotes the fusion of nearby quantum dots thus leading to interconnected nanocrystals.

A study of the circularly polarized magneto-photoluminescence of colloidal PbS nanocrystals under the influence of a magnetic field up to 30T is presented. A semiclassical model for the population of polarized excitons is used to account for the measured magnetic field and temperature dependence of the degree of circular polarization of the QD photoluminescence. The g -factor, g_X , of the exciton and its dependence on the QD size is reported for the first time. The value of g_X increases from 0.1 to 0.3 at low temperature with decreasing the nanocrystal diameter from 9 to 4 nm.

The transport properties of a PbS QDs thin film deposited between two electrodes are investigated. This study reveals a non-linear dependence of the current on the applied bias. At low temperature ($T < 100$ K), the conduction is limited by the charging energy (~ 20 meV) of the quantum dot. The fabrication of a solid-state device based on porous TiO_2 impregnated with PbS QDs is discussed. The photovoltaic response of the device in the visible and near infrared wavelength range is obtained by exploiting the Schottky junction that forms at the interface between the PbS/ TiO_2 film and a metallic contact.

Acknowledgements

During these years of PhD studies, I experienced and learnt several things which have really shaped me as a person and expanded my knowledge. I would like to take this opportunity to thank all those who gave me the possibility to complete this thesis.

First of all, I would like to offer my sincerest gratitude to my supervisor Amalia Patanè for her supervision, patience, knowledge, inspiration and great support during the period of my studies. The good advice, support and friendship of Lyudmila Turyanska have been invaluable on both the academic and personal levels, for which I am extremely grateful. I would like also to express my gratitude to Oleg Makarovsky for his great help and support throughout these years. A big thank goes also to Laurence Eaves for his useful advices.

Many thanks to Mei Li from the University of Bristol and to Michel Fay from the University of Nottingham. These external collaborators offered great help with the TEM studies of my samples. I would like also to thank Janneke Blokland and Peter Christianen from Radboud University in Nijmegen for their collaboration on the high magnetic field experiments.

I would like to thank the Medical Research Council (MRC), the Engineering and Physical Sciences Research Council (EPSRC) and the Libyan government for supporting this work.

I acknowledge the Department of Physics and the electronic workshop for providing the support and equipment needed to produce and complete my project.

I would like to thank the cheerful and friendly fellow students and post-docs in the lab.: Ateeq Nasir and Nilanthi Balakrishnan, Giorgio Pettinari and Weber Feu, with whom I shared and enjoyed countless, nice moments and conversations.

Above all, I would like to give a special warm thank to my husband Mohamed for his personal support and great patience at all times. Also, many thanks to my parents, brother and sisters for their endless love and care. Collective and individual acknowledgments are also owed to my friends outside physics here in the UK and back in Libya for their support and encouragement.

List of Publications

Publications

1. Turyanska L., Elfurawi U., Li M., Fay M., Thomas N. R., Mann S., Blokland J. H., Christianen P.C.M. and Patanè A., "Tailoring the physical properties of thiol-capped PbS quantum dots by thermal annealing" *Nanotechnology*, **20**, 315604, (2009).
2. Turyanska L., Blokland J. H., Elfurawi U., Makarovskiy O., Christianen P. C. M. and Patanè A., "Photoluminescence of PbS nanocrystals at high magnetic fields up to 30 T" *Physical Review B*, **82**, 193302 (2010).
3. Turyanska L., Makarovskiy O., Elfurawi U., Patanè A., Fay M. W., Bowers J. W. and Upadhyaya H. M. "Imaging the photovoltaic response of PbS-sensitized porous titania" *Physica Status Solidi A*, **208**, 2450 (2011)

To my precious little twins Bisan and Aban who have left much too early, but will always live in my heart.

Chapter 1

Introduction

The investigation of materials at the nano-scale has gained a great deal of interest as it fills the gap between bulk and atoms or molecules, thus improving our understanding of fundamental properties and providing new physical effects. This has been one of the hottest areas of research in the last twenty years [1, 2], fueled by the shrinking approach in device fabrication for optoelectronics and electronics. Up to date, many achievements have been reported in this field, which were a joint effort of physicists, chemists, biologists and material-scientists. By controlling their size/shape and/or their chemical compositions, the electronic and optical properties of semiconductor nanocrystals, also called quantum dots (QDs), can be manipulated [1, 3]. In particular, the confinement of the electron and hole in all spatial directions is responsible for atomic-like energy levels and physical properties.

Quantum dots can be produced by different techniques. Colloidal chemistry provides an attractive method of fabricating high quality nanocrystals. Being not attached to any surface, colloidal QDs are promising candidates to be used as building blocks for ordered structures, such as superlattices [3, 4].

Colloidal QDs could offer a number of advantages over nanostructures formed by lithographic processing or by self-assembly, including flexibility in tailoring the functionality of the nanoparticles by surface chemistry and a relatively inexpensive synthesis that is up-scalable.

Bulk Lead Chalcogenides have already been employed in several applications, for instance, thermoelectronics, infrared (IR) lasers, IR-light emitting diodes, IR detectors, solar energy panels etc [1]. The ability to tune the photon emission of Lead Chalcogenide QDs in the near infrared region of the electromagnetic spectrum makes this type of QD suitable for several applications.

PbS colloidal QDs belong to a class of IV-VI nanocrystals with narrow energy gaps of relevance for optical applications in the near-IR region of the electromagnetic spectrum such as long wavelength (1.3 and 1.55 μm) telecommunications [1], photovoltaics [5] and bioimaging in the spectroscopic window of low absorption of biological systems (1-1.2 μm) [6].

Bulk lead sulfide (PbS) has a small hole mass, which is almost equal to the mass of the electron. This leads to a large exciton Bohr radius $R_{ex} \sim 20$ nm. Owing to these properties, electrons and holes, and hence the exciton, can be strongly confined. This is not always feasible in other semiconductors because of the different electron and hole effective masses [7]. Thus this system provides an ideal platform to investigate the exciton in the strong confinement regime.

This thesis presents an experimental investigation of the optical and electronic properties of colloidal PbS nanocrystals synthesized in aqueous solution and comprising different capping ligands and/or matrices. Photoluminescence, magneto-photoluminescence, temperature and annealing effects are investigated. In addition, this thesis explores the electronic conduction in thin films based on PbS QDs and TiO_2 matrices impregnated with PbS QDs.

This thesis is structured as follows. Chapter 2 presents an introduction to the electronic properties of PbS including information about the band structure of bulk PbS and exciton. Confinement effects are also discussed using theoretical models from the literature.

Chapter 3 describes the experimental techniques and apparatus used in this thesis, such as photoluminescence spectroscopy and different microscopic techniques.

Chapter 4 describes the synthesis of the quantum dots used in this work. A detailed description of their optical and morphological properties is also given. Then studies of the temperature dependence of the photoluminescence emission of various types of quantum dots are discussed.

Chapter 5 presents a novel technique for tailoring the electronic and morphological properties of the QDs by post-synthesis thermal annealing. Transmission electron microscopy (TEM) images reveal how annealing facilitates the nanoparticle aggregation along preferential crystallographic directions. Also, annealing causes an increase in the particle size and an interesting narrowing of the QD photoluminescence emission.

In Chapter 6 the effect of high magnetic fields on the QDs is introduced. Some important parameters, such as the exciton g -factor, are extracted through the analysis of the degree of circular polarization of the QD magnetophotoluminescence and of the diamagnetic shift of the QD photoluminescence emission.

Chapter 7 explores the electronic transport in PbS QD thin films and TiO₂ matrices impregnated with PbS QDs. Current-voltage characteristics and temperature-dependent conductivity measurements are presented. Also, the photovoltaic response of solid state devices based on porous TiO₂ and PbS QDs

is discussed.

Chapter 8 provides a conclusion of this thesis and gives prospects for future investigations.

Chapter 2

Band structure properties of bulk PbS and PbS quantum dots

Research on nanostructures is motivated by the exceptional properties that a material gains when its size is reduced to nanoscale lengths. Quantum dots are nano-sized semiconductors or metals that have diameter in the range between 1 and 100 nm, and contain a limited number of atoms. The trend in reducing the size of semiconductors is fueled by the (sub) micron-fabrication and computing industry. Thus studying the properties of these materials is crucial. Also, as the electronic confinement modifies their optical, electrical and magnetic properties [8, 3], several interesting fundamental and novel physical aspects worth of investigation emerge. This chapter describes the electronic properties of quantum dots based on lead chalcogenides.

2.1 Properties of bulk lead sulphide (PbS)

Lead (*Pb*) is one of the post-transition metals and with its 82 electrons in the configuration $[\text{Xe}] 4f^{14}, 5d^{10}, 6s^2 6p^2$, the remotest electrons have the tendency to remain unshared (inert pair effect). Relativistic effects are important in PbS and act to localize the $6s$ orbital of Pb beneath the highest state of the occupied valence band, at 6-8 eV below the highest occupied molecular orbital [9], see the red dashed line in Figure 2.1. This state is chemically inactive and as a result the IV-VI compounds appear like pseudo II-VI compounds, i.e. cadmium selenide (CdSe) and cadmium sulphide (CdS), with only active p^2 orbital [10]. Nonetheless, there are huge differences in the properties of the two systems.

The occupied s -state in the valence band plays a significant role in forming the band gap, which is at the L -point in the Brillouin zone. Although there are several bands as candidates for the *valence band maximum* (VBM), the highest state of the *valence band* (VB) L_6^+ is the only one that has an identical symmetry as that of the s -level. Since the levels of the same symmetry repel (anticrossing repulsion), the L_6^+ state is pushed upward to form the VBM. In contrast, in the *conduction band* (CB), the relativistic effect represented by the spin orbit interaction creates upper energy levels of equal symmetries to the CB L_6^- state driving it downwards to form the *conduction band minimum* (CBM).

All *lead chalcogenides* (PbX), i.e. *lead selenide* (PbSe), *lead telluride* (PbTe) and *lead sulphide* (PbS) have a very similar band structure [10]. This is responsible for unusual properties. For example, increasing the number of electrons in II-VI compounds leads to a monotonic band gap shrinking, which is instead inapplicable to PbX. Also, applying an external pressure to II-VI or III-V compounds increases their energy gaps, while the opposite was observed in PbX [10].

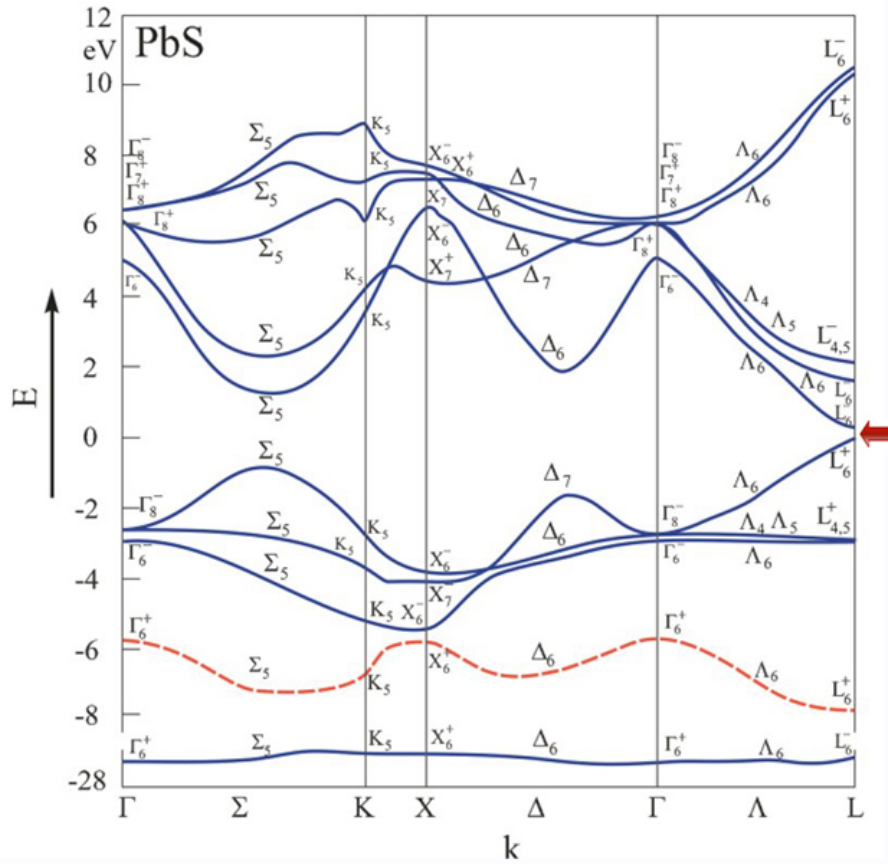


Figure 2.1: Calculated band gap structure of PbS at 73K. Reproduced from Ref. [11]. The red dashed line represents an occupied molecular orbital. The red arrow indicates the band gap.

These anomalies and some other properties are accounted for by the presence of the Pb 6s level below the VBM.

Energy levels at the L -point in bulk lead chalcogenides are fourfold degenerate (or eight including spin) resulting from the four equivalent valleys in its face centered cubic (fcc) Brillouin zone, Figure 2.1, 2.2b. A further splitting occurs due to the following reasons: (a) intervalley coupling; (b) the interaction between the conduction and valence bands; (c) the anisotropic nature of the L -band; the surface of equal energies for electrons and holes is a prolate spheroid with its major axis at the L -point, which leads to two types of masses: the transverse and longitudinal effective mass [9, 10, 12].

Lead chalcogenides are narrow band gap semiconductors, i.e. $E_g = 0.278, 0.311$ and 0.42 eV at room temperature and $E_g = 0.145, 0.18$ and 0.286 eV at 4.2K for bulk PbSe, PbTe and PbS, respectively [11]. This thesis focuses on quantum dots based on PbS. Bulk PbS is a compound that has a rock salt structure (see Figure 2.2a) with a lattice constant $a = 5.936 \text{ \AA}$. It is available in nature in a highly symmetrical crystallized form. It has a large dielectric constant $\varepsilon = \varepsilon_0 \varepsilon_r$ where $\varepsilon_r(0) = 169$ and $\varepsilon_r(\infty) = 17.2$ [11]. The electron and hole masses are comparable and relatively small ($m_{e(h)}^* \approx 0.08 m_0$), where m_0 is the electron mass in vacuum. This leads to a large Bohr radius of the exciton ($R_{ex} = 20 \text{ nm}$) and a strong regime of confinement where both electrons and holes are confined in quantum dots. Table 2.1 summarizes key properties of bulk PbS.

Table 2.1: Electronic properties of bulk PbS.

E_g (Energy gap)	0.286 eV at 4.2K 0.420 eV at 300K
$\frac{\partial E}{\partial T}$	+0.52 meV/K for $T = 100 - 400 \text{ K}$
E_b (bulk exciton binding energy)	3.968 meV (calculated)
m_e^* (electron effective mass)	0.080 m_0
m_h^* (hole effective mass)	0.075 m_0
R_{ex} (exciton Bohr radius)	20 nm
$\varepsilon_r(0)$ (dielectric constant)	169
$\varepsilon_r(\infty)$	17

Pb^{++} and S^{--} ions occupy the lattice sites in the rock-salt crystal structure alternatively [13]. Each Pb atom is surrounded by 6 atoms of S, which are arranged at the corners of the surrounding octahedron and viceversa. The PbS lattice is shown in Figure 2.2a. The Bravais lattice has a fcc Brillouin zone with a Pb ion at $(0 \ 0 \ 0)$ and a S ion at $(\frac{1}{2} \ \frac{1}{2} \ \frac{1}{2})$. Figure 2.2a shows the first Brillouin zone. The highly symmetrical points of the lattice are denoted in the graph as white circles. Γ is the centre of the Brillouin zone, while L is the centre of an hexagonal face. Dashed and solid lines represent the main directions and vectors

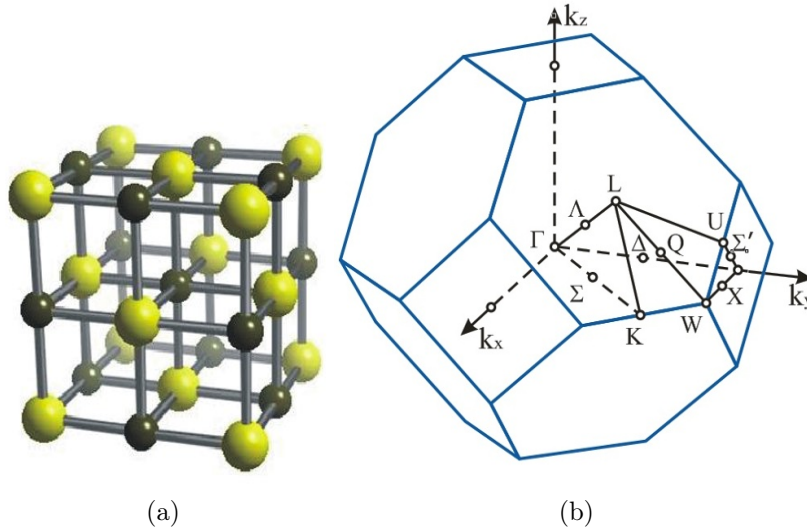


Figure 2.2: (a) Rock salt crystal structure. (b) A truncated octahedron showing the first Brillouin zone of the lattice of rock salt crystals. Points of high symmetry are also indicated. Reproduced from Ref. [11]

in k -space. The 3D band structure is represented by plotting the energy levels in k -space along these directions. Figure 2.1 shows the calculated electronic band structure of PbS reproduced after ref [11].

The CBM and the VBM are both located at the L -point, which make PbS a direct band gap semiconductor. The energy gap is $E_g = 0.42$ eV at $T = 300$ K. At $T = 4.2$ K, the energy gap is reduced to 0.28 eV. This implies that $\partial E/\partial T$ is positive. This is a unique property of lead chalcogenides, which is determined by the effect of temperature on the bond length and level repulsion.

Up to date, bulk PbX have been employed in several applications, including near infrared (IR) LEDs, photodetectors, lasers, photovoltaic and window coatings [1]. Thus modifying the band gap of these materials opens up possibilities for even a wider range of applications.

2.2 Band Gap Tuning and Quantum Confinement

2.2.1 Density of states

It is important here to introduce the concept of the density of states (DOS) as it helps to highlight the effect of quantum confinement on the electronic properties of a low dimensional system. The density of states of a particular system describes the density of available energy states per unit energy [13, 14]. The electron density of states, $g(E)$, for a three dimensional (3D) system of volume L^3 is directly proportion to the square root of the energy, i.e.:

$$g(E) = \frac{1}{2\pi^2} \left(\frac{2m^*}{\hbar^2} \right)^{3/2} \sqrt{E}, \quad (2.1)$$

so the electron can occupy a continuum of energy levels. Reducing the dimensionality of the system to 2D, e.g. for a quantum well where an electron is confined in one direction and free to move in the other two spatial dimensions, the DOS exhibits a step-like dependence. Each step in the DOS is described by:

$$g(E) = \frac{m^*}{\pi \hbar^2}. \quad (2.2)$$

These equal height staircases correspond to the quantized electronic states in the direction of confinement. In 1D systems, where electron is only free to move along one direction, for example in nano-wires, the density of states resembles an array of spikes, each representing a quantized electronic state in the direction of confinement, i.e.

$$g(E) = \frac{1}{\hbar \pi} \sqrt{\frac{m^*}{2E}}. \quad (2.3)$$

For a 0D system, such as quantum dots, where the electron is confined in the three spatial dimensions, the DOS is described by δ -functions. The electron

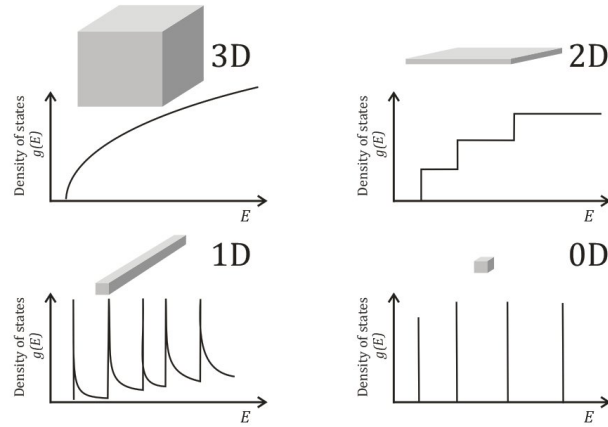


Figure 2.3: A schematic representation of the DOS in 3D, 2D, 1D and 0D.

confinement produces a series of discrete energy levels, which explain the atomic-like behavior of quantum dots and their unique optical and electrical properties [8]. Figure 2.3 is a schematic diagram showing the electron density of states for 3D, 2D, 1D and 0D systems.

2.2.2 Exciton

In semiconductors, an electron-hole pair created by the absorption of a photon is known as an exciton. The energy required for the exciton creation is slightly lower than the material band gap energy due to the Coulomb interaction between the electron and hole. Eventually the exciton vanishes through electron-hole recombination. In a direct band gap semiconductor, a photon with energy higher than E_g is needed in order to create a free electron and a free hole. On the other hand, the phonon energy is subtracted from the energy threshold in an indirect band gap semiconductor where a phonon contribution is needed to fulfill the transition [13, 15].

The electron and hole in an exciton are held together by an attractive Coulomb

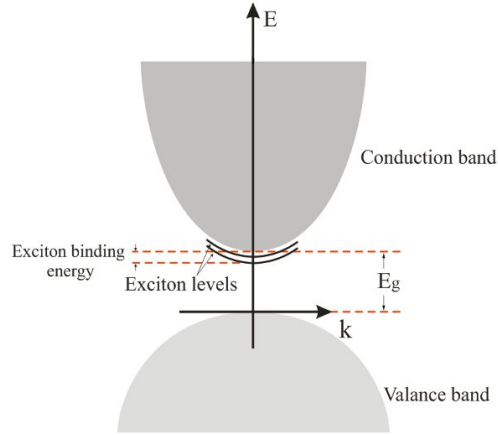


Figure 2.4: Energy levels of an exciton in a direct band gap semiconductor with conduction and valence bands at $k = 0$. Reproduced from Ref. [13]

interaction. It is convenient to compare an exciton to the well studied hydrogen atom where the proton is substituted by the hole. However, the exciton binding energy E_{ex} is much smaller due to the smaller masses of electrons and holes in semiconductors and Coulomb screening of the electron-hole interaction by the surrounding medium [16].

Based on the the exciton binding energy, excitons can be classified into two types:

- **Frenkel Exciton:** In this case the Coulomb interaction between electrons and holes is strong due to a small dielectric constant. Consequently, the exciton is tightly bound and localized around a single atom [13, 15].
- **Mott-Wannier Exciton:** In this case the Coulomb interaction between electrons and holes is screened due to a large dielectric constant. Therefore, electrons and holes are weakly bound, and the exciton wavefunction spreads spatially over a larger distance than the lattice constant [13, 15]. This type of exciton is that one relevant to the system studied in this thesis.

For a 3D system, the exciton binding energy can be expressed as:

$$E_{ex} = \frac{-\mu e^4}{8\varepsilon_r^2\varepsilon_0^2\hbar^2}, \quad (2.4)$$

where ε_r is the relative dielectric constant and R_{ex} is the exciton Bohr radius given by:

$$R_{ex} = \frac{\hbar^2\varepsilon_r}{\mu e^2}. \quad (2.5)$$

Here $\mu = m_e^*m_h^*/(m_e^* + m_h^*)$ is the exciton reduced mass and m_e^*, m_h^* are the electron and hole effective masses, respectively [15]. For bulk lead sulphide, the binding energy of the exciton is $E_{ex} = -1.8$ meV, which is smaller than the thermal energy $kT \approx 26$ meV at $T = 300$ K. The binding energy is largely enhanced in a confined system compared to the bulk.

2.2.3 Quantum Confinement in Quantum Dots

In the previous section, the concepts of DOS and exciton were introduced as they are essential to understand quantum confinement effects in semiconductors. Suitable models to illustrate the quantum confinement of carriers are also necessary to describe the optical and electrical properties of a confined system. The atomic-like behaviour of QDs arise from the discrete energy levels that emerge from the electron confinement in the three spatial dimensions. Also, the confinement induces a shift of the optical absorption towards higher energies.

Confinement effects can be probed by optical experiments, e.g. by photoluminescence or absorption in single QDs or ensembles of QDs. Valuable information about the basic physics of a QD can be also extracted by modeling the system as a semiconductor sphere surrounded by a matrix. Figure 2.5 sketches a single

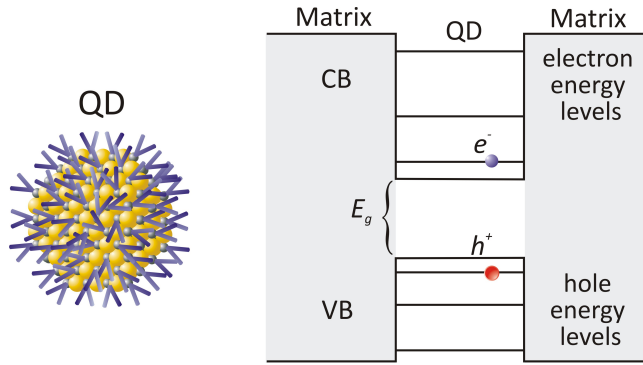


Figure 2.5: A schematic of a single colloidal QD with its surrounding matrix (capping ligands). The diagram on the right represents the potential well for each of the three spatial dimensions, and the quantized energy levels of electrons and holes in a QD.

spherical QD, its capping matrix and the energy levels diagram [17].

Several theoretical models have been proposed to describe the QD energy levels and their dependence on the QD size. The well known particle in a sphere model (infinite potential barrier) provides a simple description. By setting the appropriate boundary conditions, the energy of a particle (electron/hole or exciton) can be obtained analytically. This leads to a dependence of the energy on the radius R of the sphere of the type $E \propto R^{-2}$ [3, 17]. In this model, the mass of the carriers is the effective mass that can be derived from the curvature of the VBM and CBM.

The three dimensional infinite potential well model within the single band approximation can be useful to describe the weak confinement regime, i.e. QDs for which $R/R_{ex} \gg 1$, where R is the quantum dot radius. In this model, the electron-hole pair is treated as a single quasi-particle [18]. On the other hand, if $R/R_{ex} \ll 1$, which is known as the strong confinement regime, electrons and holes are treated separately and their energy bands are very sensitive to the boundary conditions. In this regime, the particle in an infinite potential well model is not accurate [19, 18].

The strong confinement limit is difficult to achieve in some systems. For instance, for CdSe with $R_{ex} \sim 6$ nm, the strong confinement limit can be reached only in very small quantum dots with $R \ll 6$ nm. However, this is unfeasible for InSe as its exciton Bohr radius is $R_{ex} \sim 4$ nm. In PbS or PbSe, due to the relatively large exciton Bohr radii, $R_{ex} \sim 20$ nm, the strong confinement regime is easy to be realized without the necessity of the extreme size reduction.

Table 2.2: Percentage of atoms on the surface of CdSe and PbSe QDs for given values of R/R_{ex} . Reproduced from Ref. [19].

R/R_{ex}	CdSe	PbSe
1	30%	5%
0.3	90%	15%
0.1	—	45%

Table 2.2 compares the percentage of atoms on the surface of PbSe and CdSe for different values of R/R_{ex} . Surface states are considered as one of the largest problems in the QD fabrication. As it is obvious from table 2.2, the percentage of surface atoms can be very high in small QDs. This may introduce additional states inside a material band gap, which affect electrical and optical properties of the QDs. In this case, an adequate surface passivation can reduce surface effects dramatically [8, 2].

A more realistic model of the energy levels of a QD, which consider the Coulomb interaction was proposed in 1984 by Brus [20]. In this model, the energy of the electron-hole recombination can be described as:

$$E_{QD} \approx E_g + \frac{\hbar^2 \pi^2}{2R^2 \mu} - \frac{1.8e^2}{\epsilon_r R}. \quad (2.6)$$

Figure 2.6 shows the measured and calculated dependence of E_{QD} on the QD

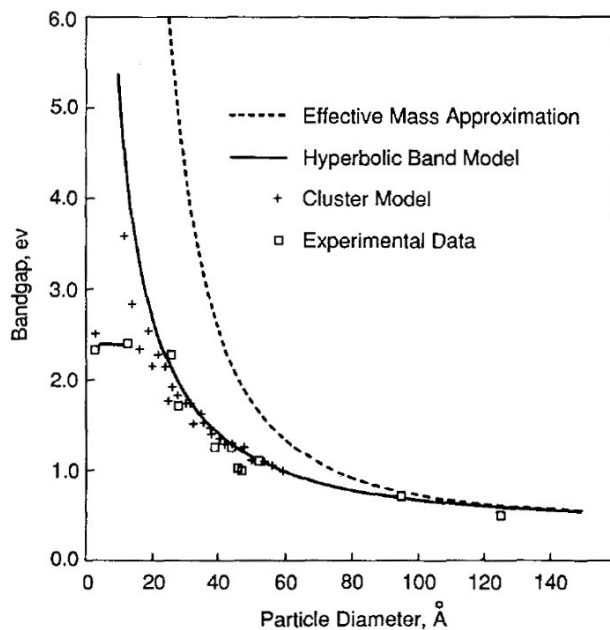


Figure 2.6: PbS band gap as a function of particle diameter. The white squares represent the measured data. The dotted line represents the exciton in a sphere model. The solid line represents the hyperbolic band model. The plus symbols show the cluster model. Reproduced from Ref [21].

diameter for PbS nanoparticles. In this Figure, the calculated curves refer to two theoretical models. From the Figure, it can be seen that the electron-hole effective mass approximation model by Brus (see dashed line) fails in describing the experimental data. This is mainly because this model does not take into account the non-parabolicity of the conduction and valence bands. When this effect is taken into account (hyperbolic model) a better agreement is achieved (see continuous line) [21]. In the hyperbolic model, E_{QD} can be written as

$$E_{QD} = \sqrt{E_g^2 + \frac{2\hbar^2 E_g \pi^2}{\mu R^2}}. \quad (2.7)$$

In all models, the combination of the large exciton Bohr radius and the narrow band gap leads to large confinement energies for carriers and hence to an absorption edge at energies much larger than that of bulk PbS.

2.3 Colloidal PbS QDs

The quantum confinement of carriers in a QD provides a means of tuning electrical and optical properties. Therefore QDs offer great potential for future technologies.

QDs can be prepared by various techniques, including molecular beam epitaxy (MBE), lithography, metalorganic -chemical vapor deposition (MOCVD) and colloidal chemistry [3, 22]. QDs synthesized by colloidal chemistry present several advantages: there is no need for them to be attached to a surface as they are synthesized in solution; thus they can be used as nanometer size building blocks for interesting structures and electronic devices [1, 23]; also their production is cheap as does not require expensive technologies [24].

High-quality colloiddally synthesized nanocrystals must fulfill the following requirements: a high degree of size mono-dispersity with a standard deviation (σ) of less than 5%, solubility in solvents, a highly crystalline core, and a well passivated surface [23, 25].

Surface dangling bonds lead to the formation of midgap levels and consequently degrade the quality of the nanocrystals fluorescence because of the increase of non-radiative carrier recombination on the surface defects. For this reason, the surface of a QD has to be passivated with a larger band gap organic or inorganic material. Passivation is very important during nanoparticle growth as well as it makes the material less active chemically, thus preventing any further atoms accumulation or larger cluster formation. In addition, choosing a suitable capping agent assists the functionalization of the dots, their solubilization and enhances carrier confinement [8, 2, 23].

Earlier research on colloidal QDs focused on those emitting in the visible region

of the electromagnetic spectrum, for example InP, and the extensively studied CdS and CdSe QDs. For QDs with visible emission the confinement effect can be visualized instantly through the change of the color of the QD solution [1]. It was only during the past 15 years that QDs with emission in the near infrared (NIR) such as PbS QDs, were identified as potentially important candidates for future applications [1, 23, 26, 27, 28]. They are promising for telecommunications as the silica fibre transmission bands are centred at $1.3 \mu\text{m}$ and $1.55 \mu\text{m}$ [29] and for deep tissue imaging as the optical window for low absorption and scattering from water and hemoglobin is between 1050 and 1200 nm [23]. Moreover, they could be utilized in many other applications such as LEDs, photo-detection and solar cells. In principle it is possible to build up a photovoltaic cell that covers almost the whole solar spectrum by using three different layers made up of three different sizes of PbS QDs [30].

Colloidally synthesized nanocrystals that emit in the NIR region of the electromagnetic spectrum can be produced using a wide range of materials e.g. II-VI, III-V and IV-VI compounds. Among them, IV-VI QDs, i.e. PbX QDs, drew a great deal of attention recently due to their outstanding electronic properties [1].

In IV-VI semiconductors, the strong confinement regime is easy to achieve for several reasons. They have a larger exciton Bohr radius compared to other systems, e.g. II-VI compounds; the small and comparable effective masses for electrons and holes involve a strong confinement energy divided evenly between carriers, in contrast to most II-VI and III-V semiconductors that have quite large and different electron and hole effective masses [1, 23], thus leading to a weak confinement of one of the carriers; due to the lack of necessity of extreme size reduction for achieving strong confinement in PbS and PbSe, surface effects can be avoided in IV-VIs. As can be seen in table 2.2, the difference in the

percentage of atoms on the surface of PbSe and CdSe QDs is significant. Another interesting property reported for PbS and PbSe QDs is the phenomenon of multiexciton generation, i.e. the generation of several excitons following the absorption of a single photon with energy $h\nu \geq 3E_g$ [31, 32]. This property could be employed to improve the efficiency of solar cells based on PbX QDs.

One of the major reasons behind the previously disregarded PbX QDs was the difficulty of producing monodispersed QDs [1, 33]. However, following the novel production of high quality PbSe QDs with a relatively uniform size and shape [25], significant progress in the field has been achieved. PbS, as it was previously addressed, has the largest band gap among PbX compounds such as PbSe, and a reduced level of toxicity thanks to the fact that sulfur is less toxic than selenium [34]. Previous studies have reported that the PbS QD emission can be tuned in the range 0.68 - 1.54 eV (800 - 1800 nm) corresponding to a particle diameter in the range 2 to 10nm [1]. PbS QDs were also produced in different shapes and hosted in various capping agents. They have been capped in a silicate glass matrix [35, 36], polymers [37], aqueous solution [27, 7, 38], organics [39], solvents [1], DNA, gelatine [27] and many others. Additionally, because of its rock-salt crystal structure, PbS has been prepared in different shapes varying from cubes, truncated octahedrons [40, 41], nanorod-based mono and multi-pods, stars [41], nanosized random shapes [28] and spheres [27, 25, 38].

Finally colloiddally synthesized PbS QDs in water-based solutions exhibit a lower toxicity rate, narrower photoluminescence emission and higher stability than their counter parts synthesized by the organometallic route [23, 27, 7].

The PbS QDs studied in this thesis are described in chapter 4. They are synthesized in water-solution. Their electronic and optical properties are investigated in detail. This thesis also explores their potential for applications in electronics, photonics and photovoltaics.

Chapter 3

Experimental setup and techniques

This chapter describes the basic experimental setups and techniques used to study the system under investigation in this thesis. The measurements were performed at Nottingham, the Nijmegen High Magnetic Field Laboratory and the University of Bristol.

3.1 Photoluminescence (PL)

Luminescence is a spontaneous radiative recombination process that involves electrons and holes [42, 43]. The excitation of carriers prior recombination requires an excitation source, which can be thermal, optical or electrical. The luminescence that occurs following an electrical excitation is known as electroluminescence, while the one that takes place after the absorption of a photon is known as *photoluminescence* (*PL*) [42].

An electron, which is excited above the CBM, and a hole, which is excited below the VBM, can gain a kinetic energy that is higher than the thermal energy $k_B T$.

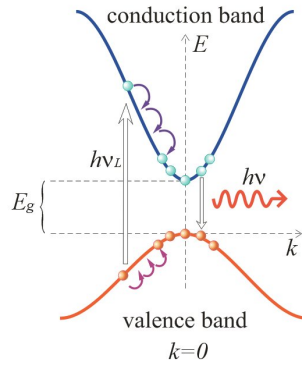


Figure 3.1: A schematic diagram showing the photoluminescence process in a direct band gap material. Carriers are excited using laser light with energy $h\nu_L$. Then they relax through phonon emission to the bottom of the conduction and valence bands. This process is followed by a radiative recombination and emission of photons with energy $h\nu$. Reproduced from Ref. [43]

Then they both tend to lose this energy very rapidly by releasing acoustic and longitudinal phonons. This process is known as carrier relaxation [43] and it is few orders of magnitudes faster than the radiative recombination. Thus, carriers may thermally redistribute prior recombining and emitting photons. Figure 3.1 presents a schematic of the photoluminescence process in a direct band gap semiconductor.

PL spectroscopy is a powerful technique to probe the electronic properties of semiconductors. It involves a simple experiment and needs minimum sample preparation as, in principle, any sample is able to emit light, can be detected regardless of its geometry, thickness or surface roughness. It can be performed at various temperatures, thus it can provide useful information on the temperature dependence of fundamental electronic properties, such as the energy of the band gap [42].

By probing the energy levels, PL offers valuable information about the composition of the semiconductor and the effect of confinement. Also, the linewidth of the PL emission can be used to understand the role of disorder (inhomogeneous

linewidth) and lattice vibrations (homogeneous linewidth) on the radiative recombination process [42].

The PL technique can be used in conjunction with an external magnetic field to extract valuable information about the spin polarization and magneto-confinement of carriers. An applied electrical field can also be used to probe the electron-hole dipole and carrier dynamics. Also, trap levels that can be activated thermally, can be studied through temperature dependent PL experiments [44].

Lasers are excellent sources for PL excitation because of their well known unique properties, i.e. they produce focused, monochromatic and intense light. The laser excitation energy determines the initial excited state, which is important to excite resonantly or non-resonantly the system under investigation. Also, the laser power controls the density of excited carriers and hence the intensity and form of the PL spectrum.

3.1.1 Photoluminescence and absorption setup

For the PL measurements at Nottingham, an Oxford Instruments continuous gas-flow cryostat was used. Cooling was provided by a helium gas flow from a liquid helium dewar. The latter was connected to the cryostat with a transfer line. A flow-meter and a pump were used to control the He flux into the cryostat. In this system, the temperature can be controlled precisely (<1 K) in the range 3.5 K to 300 K. An Oxford Instrument temperature controller connected to a rhodium iron thermometer and heater are employed to control the temperature. The cryostat is equipped with three circular optical windows with one at the front of the cryostat and the other two at the two sides. Each window is made of two layers of quartz. The inner layer is connected to the sample space while the outer is connected to the outer casing of the cryostat. Vacuum insulation

around these optical windows is secured by an indium seal. The sample was excited through the front optical window using either a He-Ne laser ($\lambda = 633$ nm) with power in the range 0.1- 5 mW, an Argon laser ($\lambda = 514$ nm) with power in the range 0.1 - 50 mW or an infrared diode laser ($\lambda = 1064$ nm) with power of up to 30mW.

For light dispersion, a 0.5m monochromator and a liquid nitrogen cooled silicon CCD array photodetector were used for PL detection in the wavelength range 400-1100 nm. For PL in the near infrared (NIR) region (800-1500 nm), a liquid nitrogen cooled InGaAs photodetector was used. Figure 3.2 shows a schematic of the optical setup. Using conventional lenses, the laser spot diameter was reduced down to $100 \mu\text{m}$. The laser power density on the semiconductor was varied in the range 130 W/cm^2 to 600 W/cm^2 .

An alternative system with a similar setup configuration was used occasionally to measure the PL. Excitation was provided by an He-Ne laser with a power on the sample up to 30 mW. The signal was focused using collecting lenses and was dispersed by a 0.75 m Spex 1702 dual-pass spectrometer. The latter is supplied with two diffraction gratings 1200 g/mm and 600 g/mm . The signal was detected by a Horiba J. Y. Ltd. Symphony multiarray InGaAs detector. For room temperature experiments, the sample was mounted on a micro-adjustable positioner for a precise sample movement in the three spatial dimensions.

For absorption experiments, the same setup sketched in Figure 3.2 was used, but in a slightly different configuration. The sample was mounted at the entrance of the monochromator and the excitation was provided by a white halogen lamp source (Newport Inc.) with a power of 250 W. Lenses were used to focus the light beam and a small hole of $\sim 100 \mu\text{m}$ diameter was mounted on the spectrometer entrance slit to control the intensity and size of the incident light. A clean

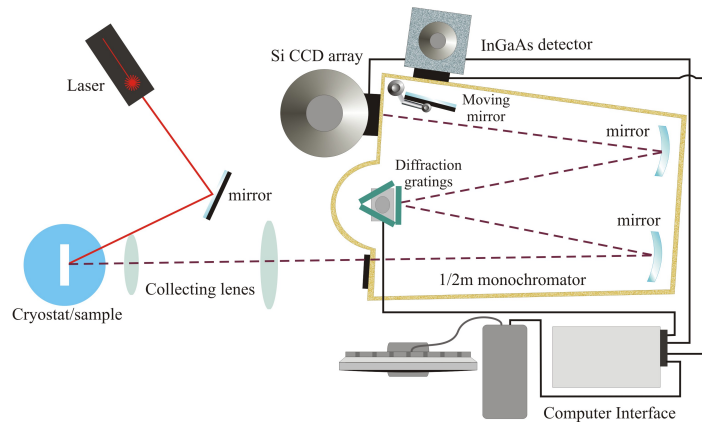


Figure 3.2: Schematic of the experimental apparatus used for optical studies.

empty substrate was used as a control sample.

One more thing worth mentioning is that detectors produce a background noise, which can be reduced dramatically by cooling the detector down to < 100 K using liquid nitrogen. Also, the computer software that controls the setup has an option to subtract this background noise from the measured signal.

3.2 Micro-PL

For micro-PL experiments at Nottingham, a Horiba Jobin Yuon Ltd.(HR800) Lab. Ram. setup was used. The micro-PL system is an integrated system designed for Raman spectroscopy and micro-photoluminescence studies, see Figure 3.3a. The power of this setup lies on its capability of performing a confocal PL mapping of a selected area on the sample with sub-micron spatial resolution. Figure 3.3b shows a schematic of the main optics of the system. For sample excitation, the system is equipped with a He-Ne laser ($\lambda = 633$ nm) with a power on the sample of up to 14.5 mW and a correspondent power density of up to 2×10^6 W/cm² for a laser spot diameter of 1 μ m. The laser beam

reaches the sample surface through a microscope. The latter is provided with three objectives with different magnifications and numerical apertures (NA): $10\times$ (NA0.25), $50\times$ (NA0.70) and $100\times$ (NA0.90), corresponding to a focused laser spot diameter varying from $3\ \mu\text{m}$ to $\simeq 0.9\ \mu\text{m}$.

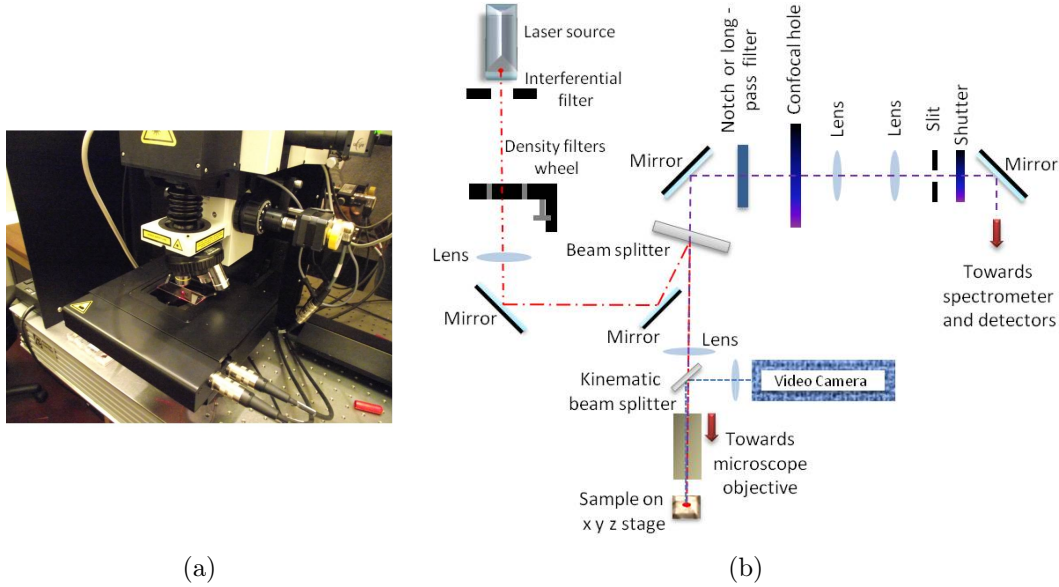


Figure 3.3: a) Horiba Jobin Yuon (HR800) Lab. Ram. setup. b) Schematic showing the main optics in the micro-PL system.

The PL signal is collected through the microscope objective, then reflected by optical components and reaches a confocal hole and hence the spectrometer and photodetectors. The focal hole diameter can be changed between 0 and $1000\ \mu\text{m}$. Reducing the hole diameter makes the system very sensitive to the variation of the PL intensity as a function of depth and it enhances the spatial resolution. Also, the smaller the hole, the greater the sensitivity of the signal to the focal length. As a result, it is possible to estimate at which depth the PL originates. For light dispersion, a 0.8 m spectrometer and a 1200 g/mm or 150 g/mm diffraction gratings were used, and for detection either a Peltier cooled CCD detector (200-1100 nm) or a liquid nitrogen cooled InGaAs array detector (800 -1600 nm) were used.

The micro-PL system has a motorized stage that can be used for micro-PL mapping. Alternatively, a laser head can move laterally to form a 2D map of the PL signal. A colored video camera and a white lamp source were utilized to acquire optical images of the sample.

3.3 Magneto-PL and circular polarized PL

For low temperature magneto-photoluminescence experiments carried out in Nottingham, a stainless steel cryostat of 1.25 m height and 0.535 m in diameter was used. The cryostat is equipped with a superconducting magnet that has the capacity to provide a magnetic field in the range 0- 14 T in a central bore of diameter 0.033 m. Also, by pumping the λ -plate, 16 T can be achieved at 2.2 K. Two coils of superconducting materials, niobium tin (Nb_3Sn) conductor aligned coaxially outside a niobium titanium ($NbTi$) conductor, are responsible for creating the magnetic field when they are cooled down below their critical points. These coils produce a high magnetic field in the core with a current up to 100 A. A superconducting switch attached to a heater is used to short circuit the coils loop so it can be operated when the heater is off. Thus, a stable magnetic field can be achieved without using the power supply.

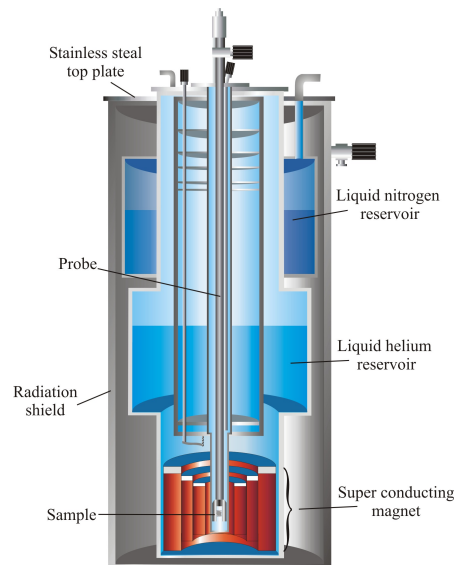


Figure 3.4: Schematic of a liquid helium cooled magneto cryostat with magnetic fields up to 16 T.

This mode of operation is known as the persistent mode.

The sample is mounted on the mounting stage at the end of a sample probe and optical access is provided by an optical fibre. The sample is cooled gradually as

it slides down into the sample space through the sliding seal. The sample space is isolated from the main helium bath by a vacuum shield. Helium flow from the main bath to the sample space is controlled by a needle valve. Using the heater in the sample space, it is possible to run experiments at various temperatures. Figure 3.4 shows a cross section of the magneto cryostat highlighting its main parts.

The facilities available at the *Nijmegen High Magnetic Field Laboratory* were used for measurements at magnetic fields up to 30 T. The magnet is a water cooled resistive bitter coils that requires 17 MW to achieve 30 T. This produces an homogeneous magnetic field in a bore of diameter 0.032 m.

Two circular polarizations, σ^+ and σ^- , of the PL emission were measured in the Faraday configuration using a circular polarizer at two successive sweeps of magnetic field with opposite directions. This study was performed in the temperature range 4.2 - 120 K.

3.4 Current-voltage characteristics

The electrical properties of our samples were probed by DC current-voltage $I(V)$ measurements. These were performed at the University of Nottingham using the simple electric circuit sketched in Figure 3.5a. The $I(V)$ s were investigated over a wide range of negative and positive applied biases using a Keithley 2400 digital multimeter. The latter was used as a voltage source and as a current meter. Data was acquired using a LabVIEW interface. The measurements were carried out over the temperature range 4.2 to 300 K.

For photoconductivity experiments, our devices were connected in series with a load resistor, a Keithley voltage source and a Keithley multimeter. The voltage

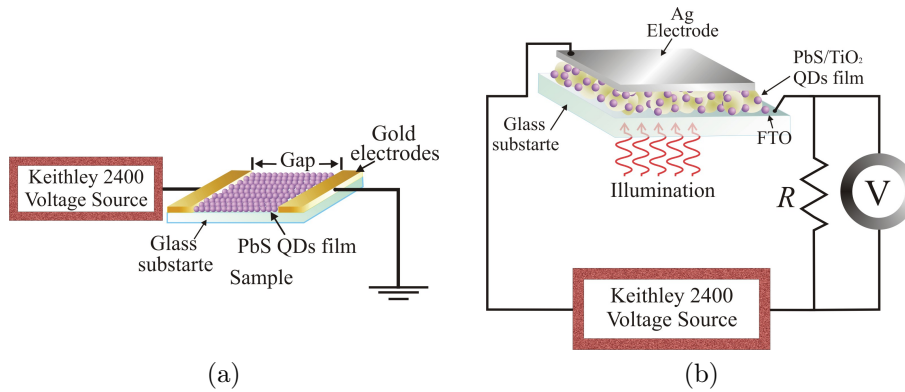


Figure 3.5: Electric circuits used to study a) transport in PbS film samples and b) TiO₂/PbS films.

across the sample was measured as the difference between the applied source voltage and that on the load resistance. For photocurrent measurement, the sample was illuminated with a laser light source ($\lambda = 633$ nm) or with a halogen lamp (Newport Inc.) equipped with a 0.25 m monochromator and grating with a 600 g/mm ($\lambda = 600 - 1200$ nm).

3.5 Microscopic techniques

3.5.1 Atomic Force Microscopy (AFM)

After the invention of *Atomic Force Microscopy* (AFM) in 1986 [45], many successful measurements were carried out. AFM can be used in principle to probe any surface with sub-nanometer resolution. Also, there is no need for sample preparation before the measurement. An AFM image is produced by exploiting the interaction between the AFM tip and the scanned surface. Also, being capable to move in the three spatial dimensions, AFM can produce a three dimensional image with sub-nanometer precision. AFM can work in any environment. However, it is advisable to use it under vacuum conditions to

avoid the adsorption and desorption of atoms, which can lead to a change of the topography of the sample during the measurement. AFM consists of three main parts: 1) a *cantilever* and a *tip*, the probe of the system; 2) a *piezoelectric transducer* to control the cantilever movements in x , y and z ; 3) a *laser* and a *detector* to detect the cantilever deflection due to the interaction of the AFM tip with the scanned surface.

AFM tips are normally fabricated by chemical etching and lithography. They are made of silicon or silicon nitride (Si_3N_4) and are approximately $10\ \mu\text{m}$ long and 2 - 40 nm in diameter. The tip is connected to the elastic cantilever, which has a low spring constant between 0.01 and 100 N/m. The sharpness of the chosen tip controls the quality of the AFM image, i.e. only one atom of the cantilever tip should interact with the specimen surface. The forces contributing to the interaction between the tip and the atoms on the measured surfaces are electrostatic and Van der Waals forces. The deflection of the cantilever is detected by a laser beam and a split photodiode. The latter is connected to a feedback loop, which modifies the tip height to keep a constant force. This adjustable height draws the sample surface map. AFM can operate in different modes. The conventional mode of operation is the *contact mode*. A sharp tip gently touches the sample, which is scanned line by line. The height of the piezoelectric transducer and the attached cantilever are adjusted manually and a further adjustment is done remotely using a computer. During the measurement, the distance between the tip and the surface is fixed. Measuring the cantilever deflections due to the variation of the repulsive or contact forces through the feedback loop, a topographical image can be built up. The forces between the tip and the surface can be calculated easily using Hook's law $F = -kx$, where k is the spring constant and x is the cantilever deflection.

AFM can also be operated in the *tapping mode* and the *lift off mode*. In the

tapping mode the cantilever oscillates at a certain frequency so it is not in contact with the surface at all times. This can avoid damage of the sample surface that can occur when the AFM tip is always in contact with the sample. In this case the feedback loop maintains the oscillation amplitude constant by lifting the tip in the z -direction. This is the mode used at Nottingham to obtain the AFM images presented in this thesis.

3.5.2 Transmission Electron Microscopy (TEM)

Transmission Electron Microscopy (TEM) is a technique that adopts the same operating principle of a conventional optical microscope. In a TEM microscope, light is replaced by an electron beam and traditional lenses are replaced by electromagnetic lenses to produce an axial magnetic field that controls the focus of the electron beam. The resolution is considerably higher than any powerful optical microscope as it is not limited by the wavelength of the visible light or lens numerical aperture.

The electron beam is produced by an electron gun located at the top of the microscope. The beam is focused on the specimen using condenser lenses. The output image is magnified over three stages. An objective lens works on magnifying the image. This image is then magnified further by the diffraction lens and finally by the projector lens before it is displayed on a fluorescent screen. An objective or a diffraction aperture can be used at the back focal plane or before the diffraction lens to improve the contrast of the final image [46].

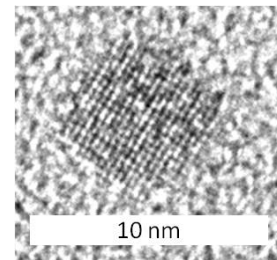


Figure 3.6: HRTEM image of a PbS QD.

TEM can be operated in a mode of imaging known as *high resolution TEM*

(*HRTEM*) or *phase contrast*. In this mode, interference between the direct beam and the diffracted ones produces an image of the sample that reflects the periodicity of the lattice with high resolution. Thus, it is possible to study crystal structure and defects. Figure 3.6 shows a HRTEM image of a single PbS quantum dot (QD) with diameter $d = 8$ nm. This measurement was performed at the University of Bristol (Dr. M. Li). Additional measurements were performed at Nottingham and will be discussed in chapter 5.

3.5.3 Scanning Electron Microscopy (SEM)

Scanning Electron Microscopy (SEM) is a technique capable to provide up to $\sim 300,000\times$ image magnification with ~ 5 nm resolution. Similar to TEM, an electron tower and a PC control unit are the major parts of the system. A tungsten electron gun is located at the top of the microscope and is responsible for the electron beam emission. This is followed by magnetic lenses, which have different roles with respect to their counterpart in TEM, as they are not accountable for magnification, but for focusing electrons into a narrow beam of less than 10 nm in diameter. Magnification is obtained by modifying the ratio of the raster (the scanned line) on the specimen to that on the display screen. Then by adjusting the size of the scanned area, the magnification can be controlled [47]. The microscope is equipped with a pair of deflecting coils that work on scanning the surface of the sample line by line to form a rectangular image. The incident electron beam interacts with the surface of the specimen and scattered elastically and inelastically forming back is scattered and secondary electrons. In addition, Auger electrons, heat and electromagnetic radiation, including X-ray, can be detected to generate energy dispersive X-ray (EDX) and X-ray diffraction (XRD) spectra. Back scattered electrons (BSE) or the reflected electrons can be detected to form an image of the specimen's surface.

However, having a smaller kinetic energy (< 50 eV) and being produced in a smaller volume compared to that of the BSE, secondary electrons tend to generate higher resolution images.

Non-conductive samples tend to accumulate charge leading to poor quality images, thus sample preparation is required prior imaging, which can be done by coating the sample with a conductive material, normally gold, and grounding it to avoid charging [47]. In this work, SEM was used at Nottingham to image a TiO_2 substrate impregnated with PbS colloidal quantum dots, which will be discussed in detail in chapter 7.

3.5.4 Energy-dispersive X-ray spectroscopy (EDX)

Energy dispersive X-ray (EDX) or (EDS) is a technique used to extract information about a specimen composition from its X-ray emission. For this purpose, an EDX detector is installed as an integrated part of SEM. Thus employing the scanning ability of the SEM, it is possible to form an elemental composition map.

X-rays are emitted when an electron from an outer atomic shell falls into an inner shell vacancy that is created by interaction between a charged beam and an electron in this shell. Thus the X-ray energy is determined by the energy difference between these two shells, which is unique for each element. An EDX graph is normally represented as X-ray counts as a function of its energy in keV. Elements can be identified from the graph by their narrow peaks at given energies. EDX and X-ray experiments were performed at Nottingham and the University of Bristol (Dr. M. Li).

Chapter 4

Samples

This chapter describes the samples studied in this thesis including a brief summary of the synthesis by colloidal chemistry of PbS QDs and their general physical properties. In addition, this chapter describes the techniques used to fabricate the structures for the conductivity studies of PbS QD films and titania matrix films impregnated with PbS QDs.

4.1 Synthesis of Colloidal PbS QDs

The PbS QDs used in this thesis were fabricated at the University of Nottingham by Dr. L. Turyanska using colloidal chemistry. The PbS nanocrystals were synthesized in aqueous solution and were capped either with thiols or dihydrolipoic acid ligands.

Thiol-capped PbS QDs were prepared by the method described by Bakueva et al [27] using thioglycerol (TGL) and dithioglycerol (DTG). These are organic compounds that have a functional group of sulfur and hydrogen atoms. They

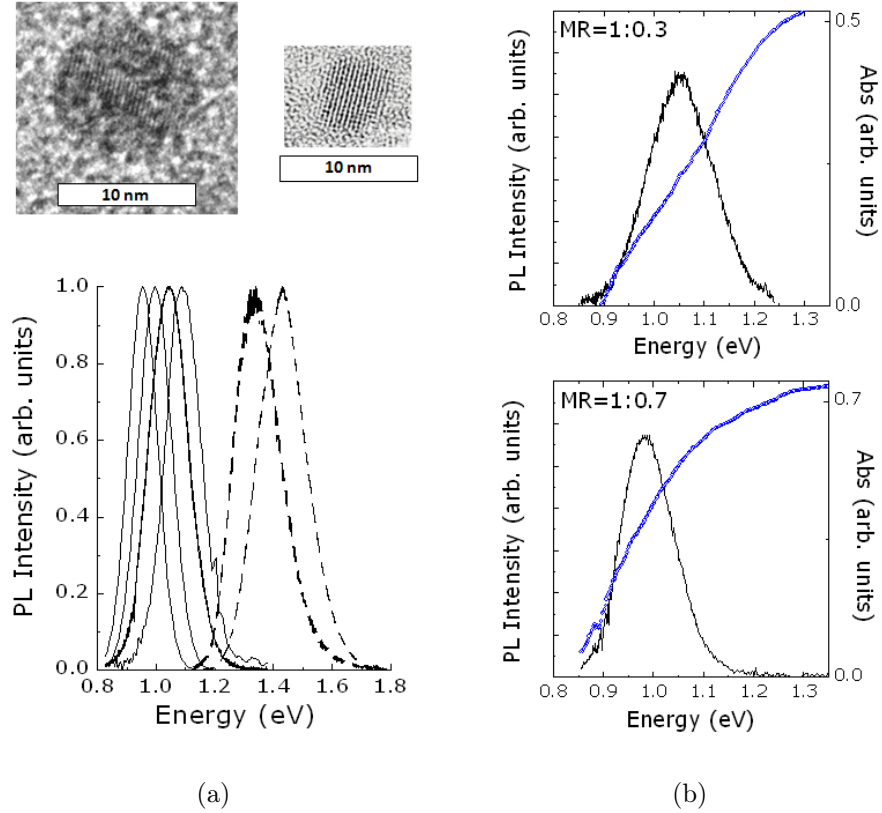


Figure 4.1: a) Room temperature PL spectra of PbS QDs capped with thiols (continuous lines) and dihydrolipoic acids (dashed lines). The top inset shows the HRTEM images of two thiol-capped PbS QDs with different sizes. b) PL and absorption spectra of thiol-capped PbS QDs with Pb:S MR =1:0.3 and Pb:S MR =1:0.7.

are about 2nm long, toxic and have a strong unpleasant odour. The method of preparation can be summarized as follows: a 15ml solution was made by a mixture of 2.5×10^{-4} mol lead acetate trihydrate $\text{Pb}(\text{CH}_3\text{COO})_2$ and thiols (1.5×10^{-3} mol TGL and 5×10^{-4} mol DTG). The pH of the solution was maintained at 11 by adding triethylamine. The final step was a rapid injection of 0.1M of sodium sulfide Na_2S solution. The outcome is a brown colloidal solution of thiol-capped PbS QDs [38]. The PbS QDs size was controlled by modifying the molar ratio of Pb:S in the range 1:0.7 to 1:0.2. Correspondingly, the PL emission of the QDs can be tuned in the range 0.9 eV ($1.3 \mu\text{m}$) to 1.12 eV ($1.1 \mu\text{m}$) (see Figure 4.1a) corresponding to QDs with diameter d in the

range 3 to 12 nm. AFM, HRTEM and EDX studies have provided detailed information on the composition of the QDs. The QDs have circular shape and a highly crystalline core. This has the same interplanar distances of rock-salt crystal in bulk PbS (see Figure 4.1 and table 4.1).

Thiol-capped PbS QDs have a PL emission with *Full Width at Half Maximum* (FWHM) of about 130 meV at room temperature. This is narrower than the linewidths for QDs produced through organometallic routes [7], thus reflecting a higher monodispersity of the QD size. However, thiol ligands tend to form disulfide compounds and oxidize when they are exposed to air and/or under strong illumination. This also leads to precipitation of the QDs in the solution [7]. Appropriate storage conditions can be used to avoid these effects. The colloidal solutions were kept under a nitrogen atmosphere and the stability of these dots was checked regularly over a period of six months. Fresh solutions were prepared each four/six months as the PL peak emission of PbS QDs tends to red shift with time, indicating particles coalescence due to *Ostwald ripening*, a phenomenon in which smaller particles are consumed in favour of larger ones to minimize the surface energy [48]. Figure 4.1b shows the PL and absorption spectra of two samples based on thiol-capped PbS QDs of different sizes. Note that the PL emission is red-shifted relative to the absorption and that the latter does not reveal a clear excitonic absorption peak. The absence of a clear absorption peak in the spectrum can be due to the broad distribution of QD sizes and strong scattering of the incident light by the non-uniform surface of the nanocrystal film.

QDs with a shorter wavelength emission ($\leq 0.9 \mu\text{m}$) were prepared at room temperature using a different stabilizing agent. Following the approach by Deng et al [49], high quality PbS QDs passivated with the long non-toxic water soluble organic ligand *Dihydrolipoic Acid* (DHLA), which has the chemical formula

HSCH₂CH₂CH(SH)(CH₂)₄COOH, were produced. Under continuous stirring, 1mL of a lead acetate solution was added to 0.3 mmol of a DHLA solution at pH =9. A 2 mL of Na₂S solution was added as small drops. This changed the color of the solution from a yellowish brown to a dark brown, thus indicating the formation of QDs with absorption in the NIR. The optical properties of these dots can be tuned by modifying the molar ratio of Pb:S:DHLA and the pH of the solution [49]. The PL emission was found to be stable for up to two months if the QDs were stored at 4°C. As for other types of QDs, DHLA-QDs should be kept under nitrogen atmosphere to avoid surface oxidation and the formation of surface defects, which can arise from long exposure to air. Also, keeping QDs at low temperature slows down the nanocrystal coalescence and the Ostwald ripening process, thus avoiding the change in the photoluminescence properties [7]. Typical PL spectra at $T=300$ K are shown in Figure 4.1a (see dashed lines).

Table 4.1: Molar ratio, PL peak position of thiol or thiol/apoferritin capped PbS QDs and their corresponding particle diameter d (from AFM) and density (estimated).

MR	$PL_{peak}(eV)$	d (nm)	Density (L ⁻¹)
1:0.7	0.95	12±1	0.7×10^{16}
1:0.6	1.00	9 ±1	1.3×10^{16}
1:0.5	1.04	5 ±1	10×10^{16}
1:0.3	1.08	4 ±1	20×10^{16}
1:0.2	1.12	3 ±1	$> 20 \times 10^{16}$

Some of our thiol colloidal PbS QDs were encapsulated in the protein shell apoferritin. Ferritin is the protein responsible for iron storage in living animal species and it is made of a shell that contains an oxide iron core. The empty ferritin shell is called *apoferritin* [50]. Encapsulating dots in the protein shell apoferritin has many advantages: it restricts the growth of PbS QDs to a size smaller than the inner diameter (8nm) of the apoferritin cage; it can minimize the response of the immune system as a result of the reduced toxicity; it can

enhance the stability of the QDs [50]. Horse spleen apoferritin, which was used in this work, consists of 24 polypeptide subunits of two types: light-chain (L-subunit) and heavy chain (H-subunit). They assemble together to form a hollow sphere with inner diameter of 7 - 8 nm and an outer diameter of 12-13 nm. Apoferritin shell has small channels that can be used to transfer iron from and into the body in order to protect it from high concentration of toxic iron [50]. These channels were employed to form PbS QDs inside the apoferritin. This method is known as *nanoreactor route*. Alternatively, it is possible to form apoferritin QDs (Aft-QD) by decomposing apoferritin into its 24 subunits and reassembling them again around the dots. This can be done as apoferritin tends to disassemble in solution at pH=2 and reassemble again at pH greater than 5. This method is known as *reassembly route*.

The successful incorporation of QDs in apoferritin was proved in a previous Nottingham study [39]. Figure 4.2 shows a TEM image of an uranyl acetate stained Aft-QD film on a carbon grid substrate. A schematic drawing of an Aft-QD cross-section highlighting the apoferritin subunits and the delivery channels is sketched in the top inset of Figure 4.7a. Aft-QDs has very similar properties to those of PbS QDs. However, the PL emission of larger dots, e.g. with $d \sim 10$ nm, is blue shifted because of the additional size growth restriction that apoferritin shell offers.

4.2 Ordering of QDs

As they are produced in solutions, colloidal QDs are potential candidates for creating ordered assemblies of nanoparticles. Many attempts have been made to assist the assembly of colloidal quantum dots into an ordered structure. These include template-guided self-assembly using plasma lithographic patterns [51];

also, relying on the natural tendency to form ordered structures, biotemplates impregnated with QDs were employed. For example: viruses, DNA and proteins were used to encapsulate nanocrystals and aid the formation of an ordered structure [52, 53]. The ordering can be improved further by varying the environment around the dots, e.g. by modifying ligands length and/or solvent. Moreover, the deposition mechanism can affect the ordering. It has been reported that spin coating with different solution concentrations, chemical treatment or even heat could enhance the ordering process [25]. The free assembly process of passivated colloidal QDs drop-cast on a substrate following a solvent evaporation is still another widely used option [54].

Superlattices that consist of a single or multi-layer(s) of closely packed nanocrystals could have properties that differ from those of individual particles [53]. It was reported that a red shift and a narrowing of the PL spectrum of self assembled InAs QDs can be achieved due to the vertical electronic coupling between the dots [55].

Capping ligands, which are responsible for the stability of the dots, act like a tunnel barrier thus reducing the electronic coupling between the dots [56]. The ligands length is one of the important parameters that must be taken into account to study the coupling effect. Another factor that should be considered is the monodispersity of the QDs as a larger size distribution reduces the electronic coupling between the QDs [57].

To study ordering effects, several samples have been produced and studied. In these samples, QDs of different type were drop-cast on a C-grid or a glass substrate using diluted solutions. Among the studied samples, we have observed an interesting self-assembling of Aft-PbS QDs into an hexagonal structure, see Figure 4.2. The TEM image of Figure 4.2 shows that the nanocrystals are

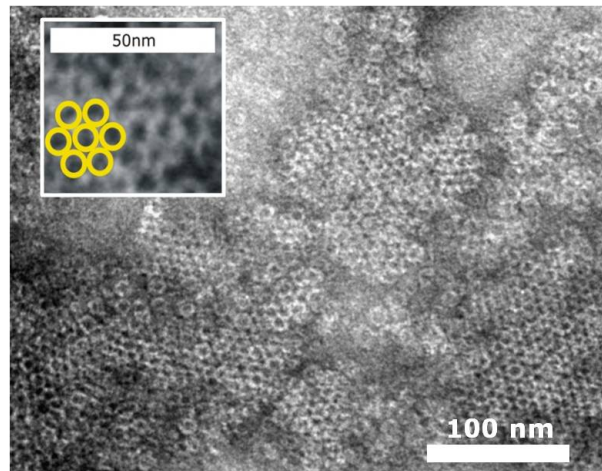


Figure 4.2: TEM image of Aft-QDs drop-cast on a carbon grid. The inset shows the hexagonal packing of Aft-QDs.

closely packed together with a typical interdistance (core to core) of ~ 10 nm. However, no sign of electronic coupling was observed in our optical studies.

When imaged over several microns, Aft-QDs deposited on glass substrates have shown different drying patterns, e.g. Christmas trees and city blocks. These patterns are illustrated in the optical microscopy images of Figure 4.3. It is interesting to note that when drying, Aft-QDs can assemble together to form elongated structures. For example in the right bottom image of Figure 4.3, these elongated structures have width of $\sim 15 \mu\text{m}$ and length of $\sim 150 \mu\text{m}$. These patterns are not always reproducible and further studies are required to control the QD self-assembly.

Figure 4.4a shows an optical microscopy image of a dendrite structure formed by self-assembling Aft-PbS QDs on a glass substrate. The micro-PL map of the area indicated by the white frame is shown in Figure 4.4b. This optical study confirms that the observed patterns arise from Aft-PbS and that these are optically active.

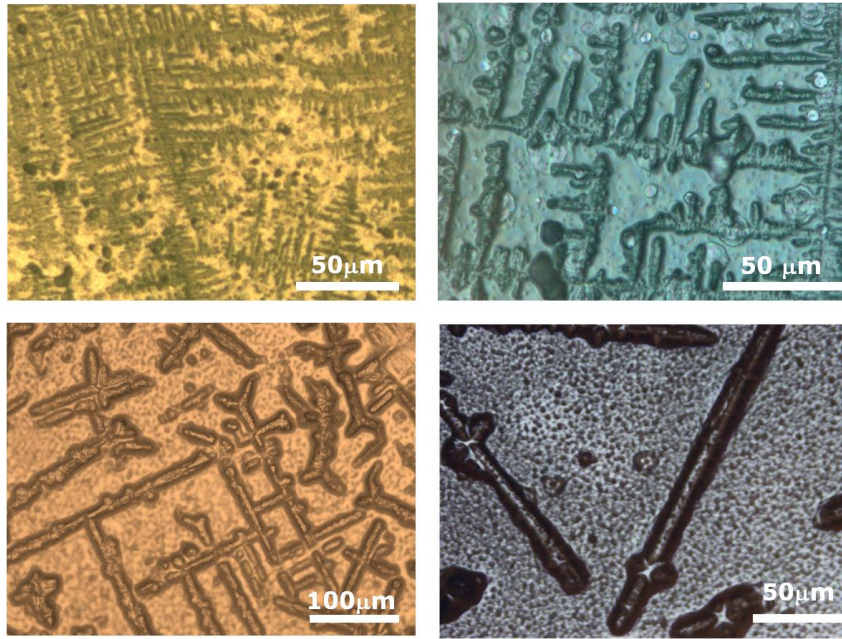


Figure 4.3: Optical microscopy images of Aft-QDs drop-cast on a glass substrate.

4.3 Samples for conductivity studies

For electrical conductivity measurements of PbS QDs films, we used a glass substrate with finely spaced gold contacts pre-deposited on its surface, see Figure 4.5. These substrates were fabricated in the Department of Electronic and Electrical Engineering at the University of Sheffield. Three different sets of devices were produced with various contacts distances $L = 10 \mu\text{m}$, $1 \mu\text{m}$ and $0.15 \mu\text{m}$ and electrode width $W = 20 \mu\text{m}$. These narrow gaps were designed to allow high electric fields and to facilitate a uniform distribution of QDs between the two electrodes.

The QDs were deposited on top of the gold contacts using the edge of a small paper impregnated with the QD solution. A thin film with an area in the range between 0.15 to 0.30 mm^2 was produced in a controllable way. Then

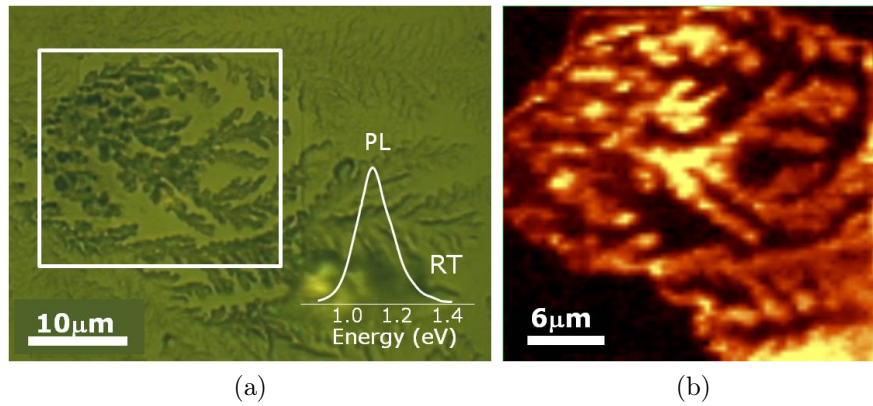


Figure 4.4: a) Optical microscopy image of Aft-PbS QDs and b) the corresponding micro-PL map. The inset is the PL spectrum of Aft-QDs at RT.

the film was let to dry in ambient atmosphere. The substrate was mounted onto a TO5 header for electrical measurements. It was wire-bonded using a 25 micron aluminum wire by using a wedge bonding technique to avoid heating the sample. Figure 4.5 shows a photograph of a device with $L = 0.15 \mu\text{m}$.

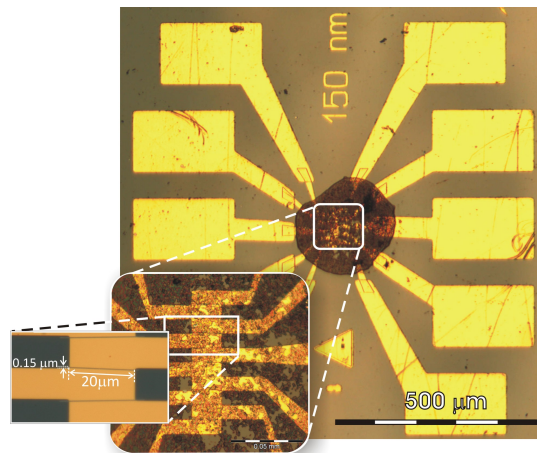


Figure 4.5: Photograph of a device with QDs between adjacent electrodes

A second set of samples was fabricated for photoconductivity studies of TiO_2/PbS films. A 3mm thick glass coated with a conductive transparent film of a fluorinated tin oxide $\text{SnO}_2:\text{F}$ (FTO) (TEC-8, Pilkington Group Limited) was used

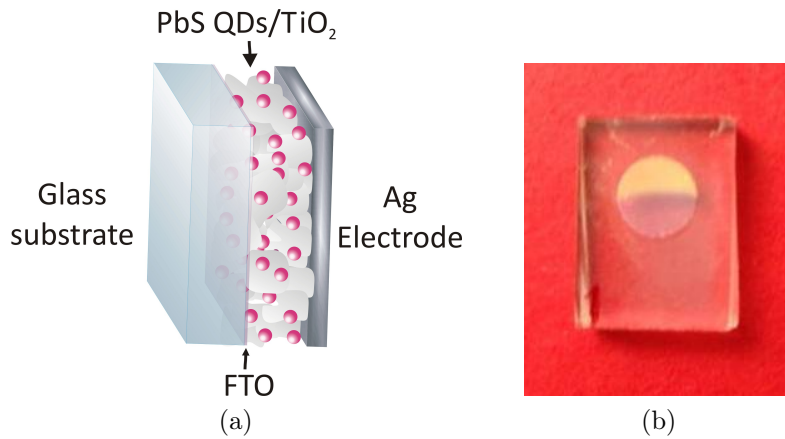


Figure 4.6: a) Schematic of a device structure based on PbS/TiO₂. b) TiO₂ films with (upper-part) and without (bottom-part) PbS QDs.

as a substrate. The FTO layer (sheet resistance of $\sim 8\Omega/\text{sq}$) was treated with TiCl_4 for 30 minutes at 70°C to improve adhesion of titania (TiO_2), which was then screen printed on the top of a FTO film. The substrate was annealed at 500°C for half an hour. Once again the film was treated with TiCl_4 for 30 minutes at 70°C . Then it was cooled down to room temperature and annealed for a second time at 500°C for half an hour. Finally, the substrate was immersed in the PbS QD solution at 4°C under a nitrogen atmosphere (to avoid dots oxidation during the filling process) for 7 days. Later, the sample was washed gently and dried in air. Finally, an Ag electrode was deposited on the top of TiO_2 using a conductive epoxy. A schematic of the device is sketched in Figure 4.6a. Figure 4.6b shows a photo of a TiO_2 film partially impregnated with PbS QDs. It can be seen that the presence of the QDs changes the colour of the TiO_2 film from white to yellow.

4.4 Temperature dependence of the QD

PL emission

This section describes the temperature dependence of the PL emission of PbS QDs and Aft-QDs nanocomposites. In particular, it describes how the peak intensity, linewidth and peak energy of the QD PL emission depend on temperature in the range 3.6 K to 300 K.

Figure 4.7 shows typical PL spectra for Aft-PbS nanocomposites at various T . It can be seen that the PL peak emission blue shifts when the temperature is increased from 4 K to 300 K. The energy shift for temperatures higher than 50 K can be described by a temperature coefficient $\alpha = (\frac{\partial E}{\partial T}) \approx 0.25$ meV/K. This value is smaller than that of bulk PbS [11], but is comparable to that reported earlier for thiol-capped PbS QDs [38] and PbS QDs in glass [58].

The energy shift of the PL emission with temperature can be caused by several mechanisms: 1) lattice thermal expansion; the distance between atoms in a nanocrystal increases by $< 10\%$ for a temperature increase from 4 K to 300 K. This in turn is responsible for a change in dE/dT of a few hundreds of $\mu\text{eV}/\text{K}$ [59], which decreases with decreasing size of the QD; 2) wave-function envelope thermal expansion, i.e. the shift of the confined energy levels as a result of the temperature change. We can express this energy shift as $dE_d/dT = (\frac{\partial E}{\partial d}) \cdot (\frac{\partial d}{\partial T}) = \frac{\partial E}{\partial d} \gamma d$, where d is the QD diameter [59] and $\gamma = 3 \times 10^{-4} \text{K}^{-1}$ [60]. For our dots, the energy varies linearly with the diameter, i.e. $\partial E/\partial d = -19.5$ meV/nm. Thus $dE_d/dT \simeq -23.4$ $\mu\text{eV}/\text{K}$ for $d=4$ nm. This is a very small contribution which tends to decrease with decreasing d ; 3) strain due to thermal expansion mismatch between the QD and its outer shell or capping agent, which is material dependent and more effective in the case of a rigid

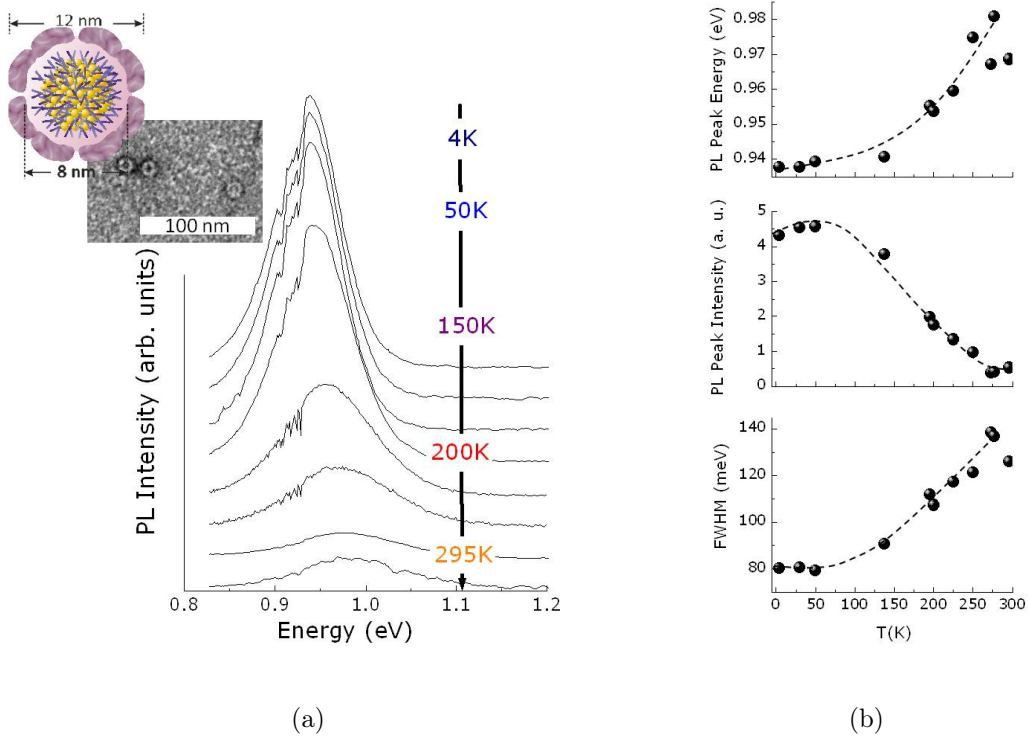


Figure 4.7: a) PL spectra at various T for Aft-QDs (laser power density $P=140\text{W}/\text{cm}^2$). The top inset is a TEM image of stained Aft-QDs on a carbon grid and a schematic of an Aft-QD. b) Top: T dependence of the PL peak positions. Middle: T -dependence of the PL peak intensity. Bottom: T -dependence of the PL FWHM. Dashed lines are guides to the eye.

matrix. Olkhovets et al. have reported that for PbS QDs in a rigid matrix (i.e. glass), the contribution of the mechanical strain is $-70 \mu\text{eV}/\text{K}$ [59]; thus we expect that strain represents a small contribution to $\partial E/\partial T$, particularly as strain should be smaller in the case of an organic matrix; 4) electron-phonon coupling; in bulk PbS, this gives a contribution of $\approx 0.15 \mu\text{eV}/\text{K}$; in reference [59] it was found that this contribution is significantly reduced in the QDs. These effects (1-4) combined together can account for the weaker dependence on T of the energy emission of the QD PL emission compared to that measured in the bulk.

The energy shift of the PL emission is accompanied by a non-monotonic T -

dependence of the PL intensity. This reaches a maximum at a temperature of 50 K followed by a monotonic decrease at $T > 50$ K, see middle graph of Figure 4.7b. The increase of the PL intensity for $T < 50$ K indicates that with increasing T , carriers that are trapped in defects of the QD overcome energy barriers and hence fall into the QD ground state, thus increasing the QD PL intensity. The quenching of the PL intensity at $T > 50$ K is attributed to the activation of non-radiative recombination processes. The temperature dependence of the PL emission intensity could also partially be caused by the redistribution of carriers between the dark (optically forbidden) and bright (optically allowed) exciton states, which are separated by a few meV [9].

The linewidth of the PL signal is also T -dependent. The QD PL emission shows a gradual increase of the FWHM at low temperature followed by strong enhancement for T larger than 100K. An increase of FWHM of 55 ± 5 meV was observed. A similar broadening was also noticed previously in thiol-capped PbS QDs [38].

Unlike isolated atoms, carriers in QDs couple to the vibrational modes of the crystal lattice [61], and interact with longitudinal optical (LO) and acoustic (LA) phonons, thus broadening the optical linewidth with temperature. It was reported that the typical PL spectra of a single quantum dot consist of a strong sharp Lorentzian peak, which is known as the zero phonon line (ZPL), and weaker Gaussian sideband(s). Both peaks get broader with temperature [61]. The sideband can be very strong in some QDs, such as CdSe QDs [62]. In such a system, the LO-phonon population increases dramatically at higher temperatures, thus high energy QD states that lay in the range of the LO-phonon energy can be populated causing an enhancement of the spectra sidebands. In contrast, this is not the case for PbS QDs as the separation between the energy levels is far too large (~ 0.4 eV) in comparison to the LO-phonon energy (\sim

30 meV) leading to a weaker coupling to the LO-phonon. This is known as phonon bottleneck [38, 63, 64]. However, a considerable PL-line broadening is observed at high temperature due to carrier-phonon interaction. This induces an *homogeneous broadening*, which is an intrinsic property of the material. The PL linewidth is also controlled by an *inhomogeneous broadening* due to the size/shape distribution of the QDs. Peterson et al. have reported that the PL spectrum for a single quantum dot is a single broad (~ 100 meV) non-Lorentzian peak at room temperature [63]. This broad PL band for a single QD is comparable to the broad emission of our QD ensembles. We modeled the temperature dependence of the PL linewidth, Γ , using the following relation [65]

$$\Gamma(T) = \Gamma_{inh} + \eta T + \frac{\Gamma_{LO}}{\exp(\hbar\omega_{LO}/k_B T) - 1}, \quad (4.1)$$

where Γ_{inh} is the inhomogeneous contribution to the PL linewidth (the temperature independent broadening), η describes the exciton interaction with acoustic phonons, Γ_{LO} is the exciton LO phonon coupling strength, and $\hbar\omega_{LO}$ is the LO-phonon energy. For bulk PbS, the LO phonon energy at the L -point is $\hbar\omega_{LO} = 29$ meV [11]. The term $[\exp(\hbar\omega_{LO}/k_B T) - 1]^{-1}$ represents the LO-phonon Bose-Einstein distribution function. This model is known as the *independent Boson model* and describes the thermal broadening of the PL emission spectra due to interaction of carriers with phonons [61].

By fitting the measured data using eq.(4.1), we find that the linear term, ηT , which represents the broadening due to LA-phonon scattering, contributes with a small value to $\Gamma(T)$ (less than 5 meV at RT). Thus it can be neglected with respect to Γ_{LO} , which is responsible for a value greater than 50 meV at RT.

The measured FWHM of Aft-QDs was fitted by equation 4.1 with $\eta=0$. It was found that $\Gamma_{inh} = 80$ meV and $\Gamma_{LO} = (124 \pm 5.5)$ meV.

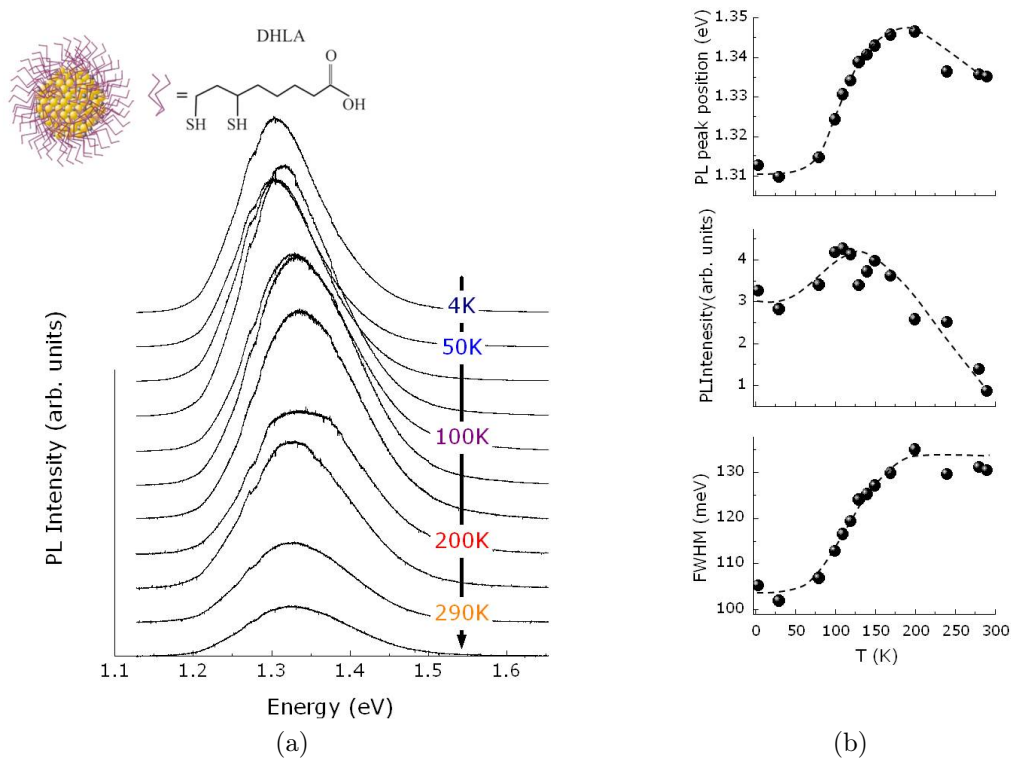


Figure 4.8: a) PL spectra at various T for DHLA-QDs ($P=140 \text{ W/cm}^2$). The top inset is a schematic of an DHLA-QD. b) Top: T dependence of the PL peak position. Middle: T -dependence of the PL peak intensity. Bottom: T -dependence of the PL FWHM. Dashed lines are given as a guides to the eye.

We now consider the T -dependence of the PL emission of DHLA-PbS QDs. Two sets of DHLA-QDs samples were used with molar ratios Pb:S:DHLA of 1:0.2:3 and 1:0.5:3. Figure 4.8a shows the PL temperature dependent spectra of PbS QDs with MR 1:0.5:3 including a schematic of the dot, the PL peak position, the PL peak intensity and the FWHM as a function of temperature in the range 4 - 290 K. The PL peak position blue shifts by $\sim 40 \text{ meV}$ corresponding to a value of α of $0.22 \pm 0.01 \text{ meV/K}$ for temperatures in the range between 20 and 200 K. This value is smaller than that for the bulk and other QDs studied before. This could be explained if we consider that these dots are smaller in size. Thus they experience a stronger confinement. Similar values of α were found for QDs with MR1:0.2:3.

As observed for thiol-capped PbS QDs and Aft-PbS QDs, DHLA-QDs show a PL intensity increase at low T followed by a monotonic decrease. The temperature at which the PL intensity reaches a maximum is different for QDs with different diameter and tends to be larger for smaller dots. Also, these QDs have revealed a photobleaching effect, i.e. the PL intensity was observed to decrease after exposure to light.

Table 4.2 summarizes the value of Γ_{inh} and Γ_{LO} as derived from a fit to the data for different QDs.

Table 4.2: Values of Γ_{inh} and Γ_{LO} as derived from a fit to the data for different QD samples. The PL peak energy at RT is also given.

Sample	MR	$PL_{peak}(eV)$	$\Gamma_{inh}(\text{meV})$	$\Gamma_{LO}(\text{meV})$
DHLA-PbS	1:0.2:3	1.45	134	88 ± 5
	1:0.5:3	1.33	103	87 ± 13
Thiol-PbS	1:0.2	1.03	72	123 ± 5
Aft-PbS	1:0.3	1.08	80	124 ± 5

The unusual red- shift of the PL peak position and the saturation of the FWHM for the DHLA-QDs at $T > 200$ K (see figure 4.8) could be due to the presence of a multi-modal distribution of QDs. The T dependence of the PL emission may originate from the contribution of two PL bands with different behaviors. It is not surprising that this anomalous dependence is observed only in the DHLA-QDs, which have significantly broader FWHMs than the thiol-capped PbS QDs.

In general, DHLA-QDs samples exhibit a larger value of Γ_{inh} , which reflects a lower QD size monodispersity. On the other hand, they show slightly smaller Γ_{LO} values, which means that they have a weaker coupling to phonons. These values are still within the error bar of those reported before for other PbS QDs samples ($\Gamma_{LO} = 110 \pm 20$ meV) [38].

Chapter 5

Thermal annealing of PbS QDs

Post synthesis thermal annealing of colloidal quantum dots can enhance the electronic coupling between the dots through the decomposition of the capping ligands, thus reducing the inter-dot distance and leading to closely packed QDs with a better uniformity [66]. This chapter examines the effects of thermal annealing on the physical properties of PbS QDs. It describes in detail how thermal annealing provides a means of narrowing the QD size distribution, increasing the size of the QDs and facilitating the QD coalescence.

5.1 QD morphology

In this section we examine the morphological properties of PbS QDs subject to a thermal annealing. Two main protocols to anneal the dots were followed:

1. Hydrothermal annealing; thiol-capped or Aft-PbS nano-composites in solution were annealed in a syringe in an oxygen free environment.
2. Annealing of thin films; dried thiol-capped or Aft-PbS nano-composites,

drop-casted or spin coated on a glass or a carbon grid, were annealed in air in a pre-heated oven.

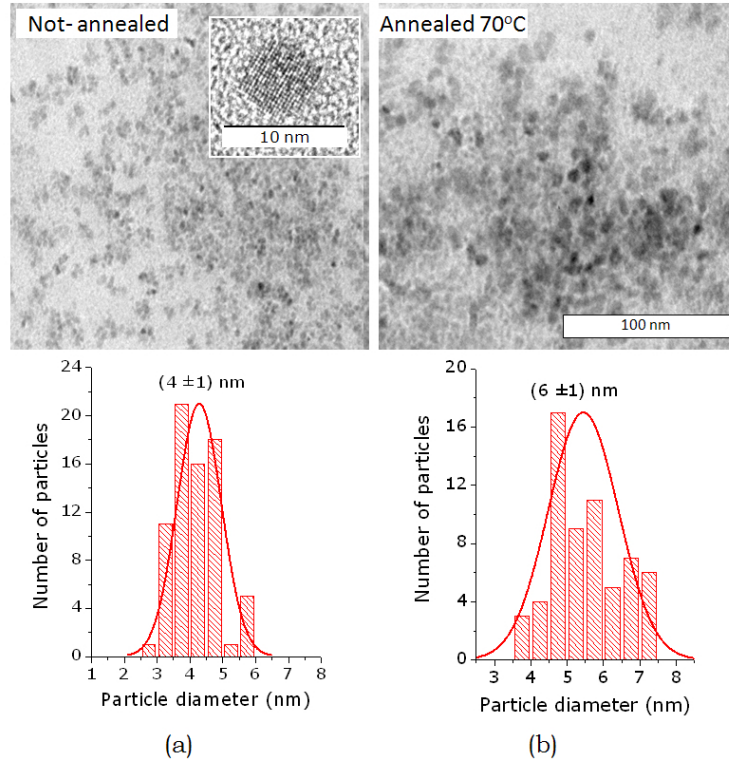


Figure 5.1: TEM images of thiol-capped PbS QDs (molar ratio MR:1:0.3) deposited on carbon grids before (a) and after the annealing (b). The inset is a HRTEM image of one of the as-prepared dots. The bottom graphs are statistical histograms representing the number of particles vs the QD diameter before (a) and after the annealing (b).

For these studies, we considered annealing temperatures, T_A , and annealing times, t_A , in the range $60^\circ - 200^\circ\text{C}$ and 15min–125h, respectively. Samples based on PbS QDs of different sizes were studied. Figure 5.1a shows the TEM images of as synthesized thiol-capped PbS QDs (Pb:S MR 1:0.3) deposited on a carbon grid. The inset of Figure 5.1 shows a HRTEM image of one of these nanoparticles. From these images it can be seen that these particles are predominately single nanocrystals of PbS and nearly spherical with an average particle diameter $d = 4 \pm 1$ nm. The observed lattice fringes in the HRTEM

image show the crystalline core of the dots. The interplanar distance extracted from the HRTEM images and the *selective area electron diffraction* (SAED) patterns is $2.94 \pm 0.04 \text{ \AA}$, which corresponds to the (100) planes of bulk PbS [67]. Hydrothermal annealing of PbS QDs at a moderate temperature $T_A = 70^\circ\text{C}$ and for a time $t_A = 10 \text{ min}$ leads to an increase in the average particle diameter to $d = 6 \pm 1 \text{ nm}$ (see Figure 5.1b).

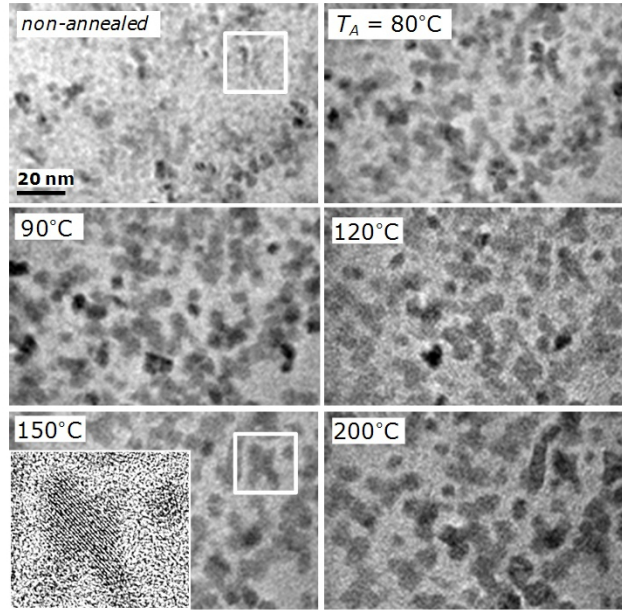


Figure 5.2: A sequence of TEM images for a film of thiol-capped PbS QDs annealed *in situ* on a carbon grid at various T_A . A small area of the QD film is indicated by white frames and imaged with higher resolution at $T_A = 150^\circ\text{C}$ (see the inset).

PbS QDs thermally annealed in air as thin films display very similar morphological changes to those annealed in solution. However, in this case the changes take longer annealing times due to the difference in particles mobility in liquid and in the film. Figure 5.2 shows a series of TEM images illustrating the morphological changes during in situ annealing TEM experiments at T_A up to 200°C . The observed increase of the PbS QDs size during the in-situ annealing is caused by coarsening. *Coarsening* is a phenomenon that accounts for many

phenomena in nature such as liquid- liquid mixture phase separation [68].

Two different coarsening phenomena can be identified:

- **Ostwald ripening**; at moderate annealing temperature ($T_A < 80^\circ\text{C}$), larger quantum dots grow at the expenses of smaller ones. This process is controlled by the particle surface energy and leads to a narrowing of the quantum dot size distribution, with the small nanoparticles gradually disappearing. On the other hand, the capping thiols around the QDs tend to stabilize more effectively smaller QDs thus slowing down the coarsening phenomenon. This was observed earlier in PbSe QDs [69].
- **Coalescence**; at higher annealing temperatures ($T_A > 80^\circ\text{C}$), which is enough for thiols or apoferritin to start decomposing, larger particles tend to coalesce together to form interconnected nanocrystals. The white frame in Figure 5.2 shows an area where few dots merge together to form a cross-like particle resulting from interconnected nanocrystals. HRTEM images and EDX spectroscopy proof that the interconnected nanocrystals are crystallographically coherent with the crystal structure of bulk PbS. This can also be seen from the well resolved lattice fringes in the HRTEM images, the EDX spectra and SAED patterns in Figure 5.3. Driven by dipole-dipole interactions, the closest annealed dots reorient, align and fuse forming a coherent island that has defects free interfaces. Pb/S ions that diffuse asymmetrically on the $\{111\}$ lattice facet lead to a net dipole along the $\langle 100 \rangle$ crystallographic axes of the rock-salt crystal structure [70, 71]. The net dipole moment along a given direction forces the dots to align. The alignment process is most likely to occur prior fusion. A similar process was reported during nanowire fabrication using PbSe QDs following ligand removal [69, 71].

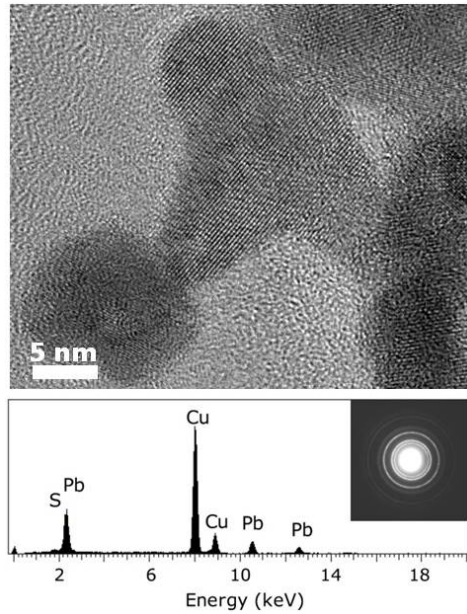


Figure 5.3: The top graph shows a HRTEM image of one of the interconnected PbS QDs annealed at $T_A = 90^\circ\text{C}$. The bottom graph shows EDX spectra and a SAED pattern of the annealed QDs.

We note that the thermal expansion coefficient for PbS QDs is $\beta = 3 \times 10^{-4}\text{K}^{-1}$ [60], hence thermal expansion induces only small changes of the particle size in comparison with the observed size enlargement. For example, a thermal annealing at $T = 100^\circ\text{C}$ would increase the QD diameter by $\approx 3\%$, which is considerably smaller than the increase of the QD size measured in the experiments ($\sim 30\%$).

5.2 QD photoluminescence emission

The morphological changes of thiol-capped PbS QDs and Aft-PbS nano-composites following thermal annealing are accompanied by remarkable changes in the electronic and optical properties, which can be assessed by PL studies. As shown in Figure 5.4, the PbS QDs PL emission shifts to lower energy with increasing annealing temperature T_A (Figure 5.4a) and/or annealing time t_A (Figure 5.4b,c).

For QDs annealed on a substrate the energy shift exhibits a large increase for $T_A > 60^\circ\text{C}$ (Figure 5.4c). Lower annealing temperature, i.e. $T_A > 40^\circ\text{C}$, are required to observe similar shifts for QDs annealed in solution. Similar effects were observed for QDs embedded in apoferritin, see Figure 5.4b. For the case of Aft-PbS QDs, the annealing is likely to decompose the Aft-shell.

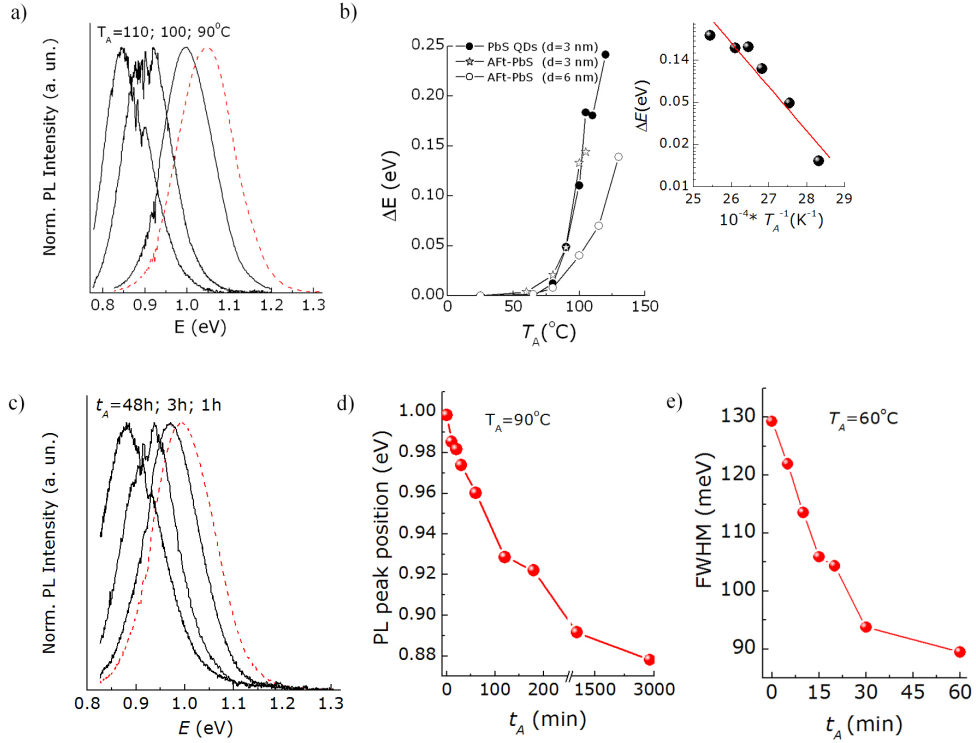


Figure 5.4: a) Normalized PL spectra of a PbS QD sample annealed at different T_A for $t_A = 1$ h. b) Energy shift versus annealing temperature for different samples. The inset shows an Arrhenius plot of the energy shift versus $1/T_A$. c) PL spectra of a PbS QD sample at fixed $T_A = 90^\circ\text{C}$ and different t_A . d) PL peak energy versus t_A . e) FWHM for the same sample shown in c) versus t_A ($T_A = 60^\circ\text{C}$). The red dotted line in a) and b) refers to the PL spectra of the control samples.

For PbS QDs annealed on a substrate, the observed energy shift (ΔE) is up to 300 meV and it tends to be larger for QDs with smaller sizes. The dependence of ΔE on T_A can be described by $\Delta E = A \exp(-E_A/k_B T_A)$, where E_A is a characteristic activation energy and A is a constant ($A \approx 8 \times 10^{11}$ eV). The

value of A is not significant. From a fit to the data, we find that $E_A = 0.8 - 0.9$ eV.

Important aspects of the thermal annealing of PbS QDs are the irreversible decrease of the PL intensity and the linewidth narrowing of the PL emission (see figure 5.4e). Both findings can be explained in terms of morphological changes. The particle growth due Ostwald ripening leads to an overall reduction in the number of particles that contribute to the PL signal, thus leading to a reduction of the PL intensity. The narrowing is instead associated with the growth in the particle size and change in the particle size distribution. These morphological changes are caused by the dynamical balance between two competing processes: the minimization of the free energy induces larger particles to grow with time at expenses of the smaller ones; on the other hand, the capping thiols tend to stabilize more effectively smaller nanoparticles [72] thus slowing down the coarsening of the dots. The narrowing of the QD size distribution and the corresponding narrowing of the QD emission are observed at annealing temperatures up to $\sim 80^\circ\text{C}$, above which we observe the fusion of nearby nanocrystals (Figure 5.3). A similar coalescence effect was reported for PbSe nanoparticles during oleic acid capping ligands displacement and was associated with the reassembly of the dots on a substrate due to a dipole-dipole interaction that occurs along preferential crystallographic directions [69]. In our samples, the thiols have high affinity for Pb^{2+} ions and provide the PbS nanocrystals with a steric shielding that screens the Van der Waals attractions between nearby nanoparticles. Annealing at high T_A can act to partially remove capping thiols from the surface of the nanocrystal, thus promoting a stronger interaction between the dots and their coalescence to form larger islands; this can be seen in the HRTEM images in the inset of Figures 5.2 and 5.3, showing crystallographic coherent nanoparticles merged to form a single island.

Under these annealing conditions the PL emission is strongly red-shifted and reduced in intensity. Thus it is likely that the emission from the largest interconnected islands is not revealed in the measured spectra within the wavelength range of detection of our measurement system.

The QD diameters were extracted from the TEM images and compared with the diameters estimated from the measured PL peak emissions. To estimate the average QD diameter from PL, a hyperbolic model for a confined exciton in a spherical QD with infinite potential barrier was used [21]. According to this model, the energy, E_{QD} , of the electron-hole recombination in a QD of diameter d is given by

$$E_{QD} = \sqrt{E_g^2 + \frac{8\hbar^2 E_g \pi^2}{\mu d^2}}, \quad (5.1)$$

where E_g is the energy band gap for bulk PbS and μ is an isotropic average mass for electrons and holes, i.e. $\mu/m_0 = 0.0387$. Figure 5.5 shows a good agreement between the values of d extracted from the TEM images (stars) and those obtained from the PL data for PbS QDs annealed (circles and triangles) at T_A up to 120°C and $t_A = 1$ h using equation 5.1.

Despite the large increase in the size of the QDs induced by the annealing, excitons remain still strongly confined as the exciton Bohr radius in PbS (~ 20 nm) is larger than the radius of all our dots. The strong regime of exciton confinement is confirmed by magneto-PL studies, which will be presented in chapter 6.

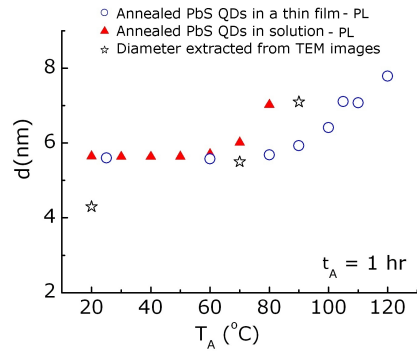


Figure 5.5: QD diameter as a function of the annealing temperature, T_A .

5.3 Temperature dependence of the QD PL emission

Figure 5.6a and b show the T -dependence of the PL spectra for as grown and annealed thiol-capped PbS QDs. All QDs exhibit a blue shift of the PL emission energy as the lattice temperature (T) grows from 4.2 K to 295 K. This shift is due to the band gap energy increase with temperature as also observed in bulk PbS [11, 38]. The rate of the energy change with T is $\partial E/\partial T = 0.3$ meV/K for both annealed and as-synthesized QDs, in agreement with observations reported previously for PbS QDs [38].

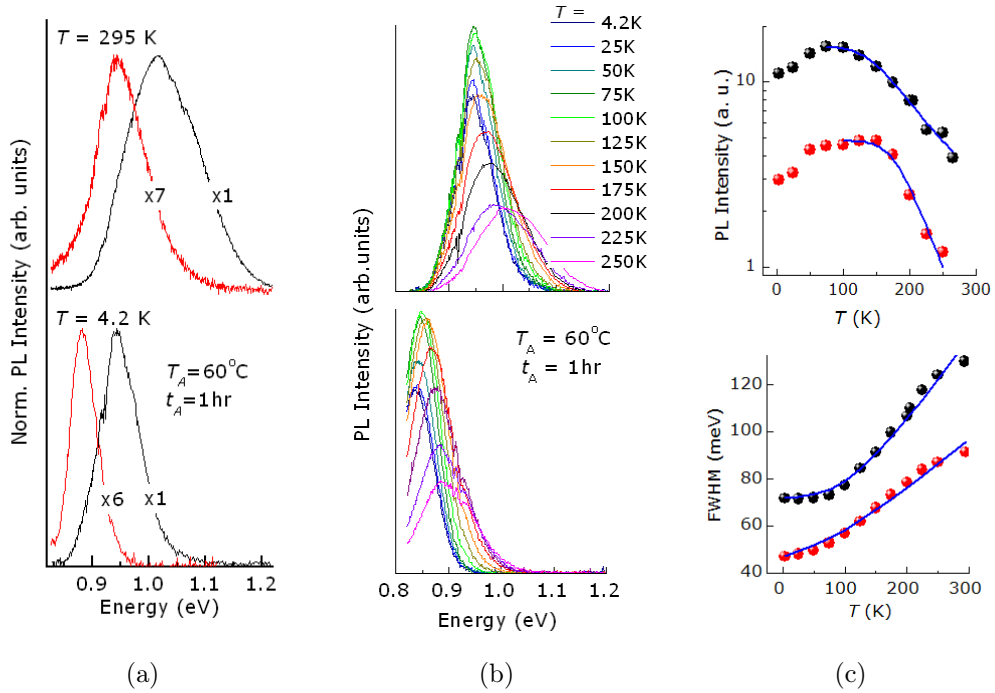


Figure 5.6: a) Normalized PL spectra of as grown (black) and annealed (red) PbS QDs ($T_A = 60^\circ\text{C}$, $t_A = 1$ h) at different lattice temperatures. b) PL dependence study of as grown PbS QDs (top), and annealed PbS QDs ($T_A = 60^\circ\text{C}$, $t_A = 1$ h) (bottom). c) top: PL intensity at different T ; bottom: FWHM at different T (black dots: as grown QDs; red dots: annealed QDs). Blue lines represent a fit to the data with simple functions, as described in the text.

The bottom graph in Figure 5.6c shows the effect of the lattice temperature

on the PL FWHM of PbS QDs as-synthesized (black) and annealed in solution (red) at 60°C for 1h. A strong increase of the FWHM was observed in all samples at $T > 100$ K. We attribute the thermally activated broadening of the PL emission to the dephasing of the quantum electronic states by electron/ hole coupling to thermally activated longitudinal optical phonons.

We fit the temperature dependence of the PL FWHM using the equation $\Gamma(T) = \Gamma_{inh} + \eta T + \Gamma_{LO}/(\exp(\hbar\omega_{LO}/k_B T) - 1)$ [65], where $\hbar\omega_{LO} = 29$ meV for bulk PbS at the L -point [11]. For annealed QDs, we find an inhomogeneous broadening $\Gamma_{inh} = 47$ meV and that the strength of carrier interaction with LO phonon is $\Gamma_{LO} \sim 46$ meV. The value of η that represents the acoustic phonon -carrier interaction is instead very small and can be neglected. The value of Γ_{LO} is approximately half of that for non-annealed PbS QDs thus indicating that for the annealed dots, the coupling of excitons to LO-phonons is lower than for the as grown sample. This finding supports previous results revealing that larger dots exhibit weaker carrier-phonon coupling [38].

The dependence of Γ_{LO} on the dot size reported in ref [38] for thiol capped PbS QDs is not observed for DHLA-QDs (see table 4.2). Here the smaller DHLA-QDs show a weaker carrier-LO phonon interaction ($\Gamma_{LO} \sim 90$ meV) compared to that found in the larger thiol capped PbS QDs ($\Gamma_{LO} \sim 120$ meV). We note that for PbS QDs embedded in a glass matrix with diameter $d = 5$ nm, Liu et. al [73] has reported $\Gamma_{LO} \sim 50$ meV. This is less than half of the value measured for thiol-PbS QDs of comparable size [38]. Oleic-acid-capped PbS QDs have shown $\Gamma_{LO} \sim 70$ meV for QDs with size comparable to that of our DHLA-PbS QDs [74]. Thus we conclude that the value of Γ_{LO} depends not only on the particle diameter, but also on the capping agent.

Interestingly, for the annealed dots, the RT FWHM (~ 90 meV) compares

with the linewidth (~ 100 meV) reported for a single PbS QD emission [63]. Therefore for these QDs, the RT FWHM is mainly limited by an intrinsic scattering process due to carrier interaction with phonons rather than by the QD size/shape distribution.

We now consider the T -dependence of the QD PL intensity. The top graph of Figure 5.6c shows that with increasing temperature from 4.2 K up to $T \sim 100$ K, the PL peak intensity of as-synthesized and annealed PbS QDs exhibits an increase, followed by a monotonic decrease at higher T . The PL intensity enhancement at intermediate T is attributed to the thermal excitation of carriers out of QD defect states followed by carrier relaxation into the QD ground state. In contrast, the PL intensity decay at higher T is associated with the excitation of carriers out of the dots into non-radiative recombination centres. The temperature dependence of the PL intensity for annealed samples is similar to that of as synthesized PbS QDs [38]. However, for annealed dots a higher T is required to reach a maximum in the PL intensity. A possible explanation is that thermal annealing introduces deeper trap levels into the QDs. Also, note that at all temperatures, the PL intensity of the annealed QDs is smaller than the PL intensity of the as-synthesized ones. Increasing annealing temperature/time (T_A/t_A) leads to a more pronounced quenching of the PL signal. This could be due to an increasing number of surface defects caused by the ligand displacement [70]. The T -dependence of the QD PL intensity at high T (> 100 K) can be described by a simple model [75], i.e. $B/(A \exp(-E_A/k_B T) + 1)$, where A and B are constants and E_A is a characteristic activation energy. For the as grown sample $E_A \sim 70$ meV, which is significantly smaller than that found for annealed dots ($E_A \sim 120$ meV).

To conclude, thermal annealing can be used to tune the electronic and the morphological properties of thiol-capped PbS QDs and Aft-PbS nano-composites.

Annealing at relatively moderate temperatures ($T_A < 80^\circ\text{C}$) provides a means of red-shifting and narrowing the QD PL emission. At higher annealing temperatures, interconnected nanocrystals are formed due to ligand displacement. This leads to strong quenching of the PL signal.

Chapter 6

Magneto-photoluminescence

This chapter investigates the magneto-PL properties of colloidal PbS nanocrystals. It reports the temperature dependence of the circularly polarized magneto-PL and a semi-classical model to describe the population of polarized excitons. This study allows us to find the exciton g -factor and its dependence on the QD size.

6.1 Exciton fine structure in PbS QDs

Compared to II-VI and III-V semiconductors, PbS and other chalcogenides QDs exhibit a complex exciton fine structure. The lowest excitonic energy level in bulk PbS has 64 degeneracy. This degeneracy arises from the fact that the CBM and VBM are at the L-point and are 8-fold degenerate each. The degeneracy can be lifted by quantum confinement, intervalley coupling, effective mass anisotropy (longitudinal and transverse masses), electron-hole Coulomb interaction and exchange interaction. If we consider the ground state of an exciton in a QD, the 4-fold degeneracy of this state is split into a three-fold

degenerate upper level and a dark non-degenerate lower level with an energy splitting $\Delta_X \leq 20$ meV between these two levels [9, 76]. Figure 6.1 shows a schematic of the single particle energy levels and of the singlet dark (optically forbidden) and triplet bright (optically allowed) exciton levels in a PbS QD.

Magneto-PL has proven to be a useful technique to extract valuable information about excitons in QDs. It can be used to probe the exciton fine structure [77], the exciton g -factor and its dependence on lattice temperature [78], electric field [79], quantum confinement and size/shape of QDs [80]. Our PL experiments in magnetic fields are used to explore these phenomena in PbS QDs. Before presenting the data, in the following sections 6.2 and 6.3 we review briefly basic concepts on Zeeman splitting, g -factor and polarization of light.

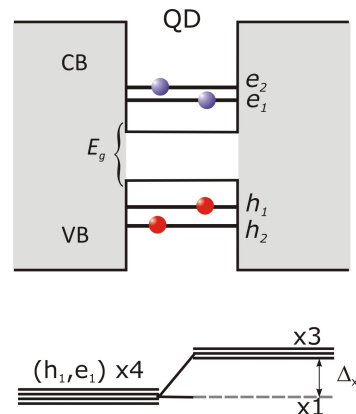


Figure 6.1: Schematic of single particle energy states and excitonic states. Bright and dark exciton state are split by Δ_X . Reproduced from Ref. [76]

6.2 Zeeman Splitting and g -factor

An electron interacts with a magnetic field B through its magnetic moment $\mu_B = e\hbar/2m_0$. Depending on the spin direction (up or down), the magnetic field lifts or lowers the electron energy by $g\mu_B B$, where g is the g -factor. This creates an energy difference between spin-up and spin-down states known as Zeeman splitting.

The value of the g -factor is affected by carrier confinement due to the quantization of the energy levels and the modification of the spin-orbit coupling. Thus the g -factor in a quantized system can be very different from that of the bulk.

For instance, Au nano-particles have a g -value that is significantly smaller than that of the bulk. In contrast, it was found that for InAs nanowires the g -factor is strongly enhanced [64].

Determining the value of the g -factor in a semiconductor has a great importance especially in the field of spintronics as it provides valuable information about the spin and magnetic field related degeneracy lifting [79].

6.3 Polarization and selection rules

Polarization is an important property of light and can be used to study and manipulate the population of polarized excitons. Light can be linearly, circularly or elliptically polarized. Circularly polarized light can have either left or right helicity corresponding to photons with angular momentum along the direction of propagation that is positive (right helicity σ^+) or negative (left helicity σ^-). It is possible to change a linearly polarized light into a circularly polarized (and vice versa) by using a wave-plate (retarder), which is a uniaxial crystal with an axis-dependent refractive index. Light propagation through such a crystal makes the light to travel slower or faster depending on the traveling direction. In our experiment, σ^+ and σ^- light were measured using a circular polarizer composed of a $\lambda/4$ (quarter wave) plate and a linear polarizer.

The momentum of a photon can be transferred to an exciton and shared between its electron and hole through spin-orbit interaction [81]. Following the absorption of circularly polarized light σ^+ or σ^- with energy $h\nu$ greater than the semiconductor band gap E_g , the spin population of the exciton energy levels changes according to selection rules, and only transitions satisfying the condition $\Delta m_j = \pm 1$ are permitted, where m_j is the angular momentum quantum

number.

In a PL experiment the uneven population of excitons due to the difference of their spin orientation (spin up σ^+ and spin down σ^-) leads to a difference in the PL intensities. Under the influence of an external magnetic field, the polarization of the PL emission occurs as a result of the Zeeman splitting of the conduction and the valence bands [82]. The degree of circular polarization, *DCP*, of the PL intensity can be calculated as

$$DCP = \frac{I_{\sigma^-} - I_{\sigma^+}}{I_{\sigma^+} + I_{\sigma^-}}, \quad (6.1)$$

where I_{σ^+} and I_{σ^-} represent the peak intensities of the right and left circular polarized QD PL emission, respectively. The signal of the *DCP* changes depending on the dominant spin population, e.g. *DCP* is positive if I_{σ^+} is larger than I_{σ^-} .

6.3.1 Spin Relaxation and Carrier Recombination Time

The time required by the spin to relax is known as the spin relaxation time τ_s . This time is an important parameter in studying the polarization and spin dynamics. At $B=0$ T, the exciton loses its polarization very quickly, i.e. $\tau_s \ll \tau$, where τ is the exciton recombination time, thus the *DCP*=0. On the other hand, the polarization is enhanced by magnetic field as τ_s becomes much longer than τ [83, 81]. The spin relaxation time can range from few picoseconds to microseconds. It has been reported that it takes few nanoseconds for the spin to relax in most of non-magnetic semiconductors [81]. For the polarization to be detected, τ_s has to be longer than the exciton recombination time τ . Thus studying the polarization of the PL can provide information about the spin

population, the spin relaxation time, the g -factor and the exciton recombination time [81].

Using τ_s and τ we can express the DCP as $DCP = P_0/(1 + \tau/\tau_s)$, where P_0 represents the maximum degree of polarization [83].

Spin relaxation mechanisms can vary in different systems. The most common mechanisms are briefly described below. Spin relaxation by phonons originates from the effective magnetic field created by the electric field associated with lattice vibrations through spin-orbit coupling [83]. This is generally a very weak effect. Spin relaxation can occur by charged impurity. These create a magnetic field which affects the electron spin through spin-orbit interaction. This type of relaxation mechanism depends on the impurities concentration. It is known as Elliott-Yafet mechanism and it can be dominant in some semiconductors, such as GaAs [83]. Relaxation through the Dyakonov-Perel mechanism involves electron spin-flips without collisions. It is common in non-centrosymmetric semiconductors such as GaAs, but less in centrosymmetric semiconductors such as Si, Ge and PbS [81, 84]. Relaxation can occur by the Bir-Aronov-Pikus mechanism. In this case the spin relaxation is due to electron-hole exchange interaction. It increases with increasing the number of holes, thus it is significant in the case of p-type semiconductors [83]. Spin relaxation due to the hyperfine interaction (or interaction with nuclear spin) involves electron spin-flips due to electron interaction with the magnetic field of the nuclear spin. Last but not least, the hole spin in the valence band can also relax due to the spin-orbit interaction. This process tends to be faster than for electrons [83].

The spin relaxation time is usually of the order of 10 ps in bulk semiconductors, which is considered to be very fast. This time tends to increase in the presence of quantum confinement of carriers [85]. The measurement of this important

parameter is still missing in several quantum confined systems.

6.4 The strength of carrier confinement in PbS QDs

An energy blue-shift accompanied by an increase in intensity of the QD emission can be anticipated due to the extra confinement exerted by magnetic field on the carriers. This shift is called diamagnetic shift and it exhibits a linear dependence on B at very high magnetic field. However, at magnetic field up to few teslas it is proportional to the square of B , i.e.

$$\delta E = \frac{e^2}{8\mu} \langle \rho^2 \rangle B^2, \quad (6.2)$$

where $2\sqrt{\langle \rho^2 \rangle}$ is the expectation value of the square of the electron-hole distance in the plane perpendicular to B and μ is the exciton reduced mass [86]. For a QD, the diamagnetic shift is expected to be smaller than that of the bulk due to quantum confinement, thus a relatively high magnetic field should be employed in order to detect a measurable shift.

A static magnetic field, B , up to 30 T was used to investigate the unpolarized and circularly polarized magneto-PL of colloidal PbS nanocrystals with emission in the NIR (1000-1300 nm) and average diameter ranging from 4 nm to 9 nm. The magneto-PL study was performed under non-resonant excitation conditions on PbS QDs drop-cast on a glass substrate in a temperature range 4.2-120 K. The optical excitation was provided by the 532 nm line of a solid state laser ($P=5 \times 10^4$ W/m²). The luminescence was dispersed by a 150 g/mm grating and detected by a nitrogen cooled (InGa)As array photodiode. The samples were

mounted on an optical probe and cooled inside a liquid helium bath cryostat in a 33 T Bitter-type electromagnet. Two circular polarizations, σ^+ and σ^- , of the QD PL emission were measured in the Faraday configuration using a circular polarizer at two successive sweeps of magnetic field with opposite directions.

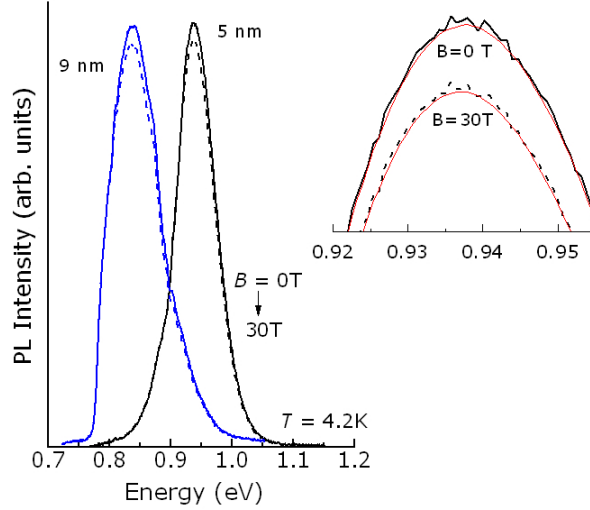


Figure 6.2: Low temperature ($T = 4.2$ K) unpolarized PL spectra at $B=0$ (continuous lines) and $B=30$ T (dashed line) for PbS QDs with average diameter $d=5$ nm and 9 nm. The inset shows the PL spectra around the peak for the sample with $d=5$ nm and fits to the data by Gaussians.

Figure 6.2 shows the low temperature ($T=4.2$ K) unpolarized PL spectra of two ensembles of thiol-capped PbS QDs with average diameter $d= 5$ nm and 9 nm under applied magnetic fields $B = 0$ and 30T. The magnetic field has two main effects on the QD PL spectrum. It red-shifts the PL emission by 1meV and decreases its intensity by $\sim 5\%$. At first sight, these effects are counterintuitive. In fact, as mentioned before, an energy blue-shift and an increase in intensity of the QD PL emission would be expected due to the extra confinement exerted by the magnetic field on the carriers. Using equation 6.2, it is found that $\delta E = 2-10$ meV at $B=30$ T with $\rho_X = \sqrt{\langle \rho^2 \rangle} \sim d/2$, d in the

range 4 - 9 nm, and $\mu = 0.038 m_0$. Such energy-shifts were not observed in any of the measured samples. This observation combined with the small redshift of the QD emission measured at high B suggests the existence of a competing physical mechanism counteracting the diamagnetic shift of the exciton states. The absence of an energy shift also implies that the exciton wave-function is confined over distances smaller than the magnetic length $\ell_B = \sqrt{\hbar/eB}$. For $B = 30$ T, corresponding to the largest field used in an experiment, we find $\ell_B = 5$ nm.

6.5 Circular polarization of the QD PL emission

To explore further the magnetic field dependence of the exciton states, we have studied the circular polarization properties of the QD PL emission. Figure 6.3 shows the low temperature ($T = 7.5$ K) circularly polarized PL spectra at applied magnetic fields up to 30 T for QDs with average diameter $d = 4$ nm. The top inset of Figure 6.3 shows the field dependent PL peak intensity for σ^- and σ^+ at 7.5 K. From the graph it can be seen that for σ^- , the PL emission grows sharply with the applied magnetic field and it shows an increase of up to 60% at the maximum field $B=30$ T. In contrast, for σ^+ the PL peak intensity demonstrates smaller changes and a sign of saturation at $B > 24$ T.

As shown in the bottom inset of Figure 6.3, at low T , the DCP increases linearly with B at low fields ($B < 10$ T); a further increase of B leads to a sublinear increase of the DCP up to a value of $\sim 30\%$ at $B=30$ T. With increasing T , the DCP decreases and the DCP tends to saturate at higher values of B . All our samples showed similar dependencies of the DCP on T and B . Figure 6.4a shows the B -dependence of the low temperature DCP for PbS QDs with different diameter. The value of the DCP at $B=30$ T is in the range 25-35%

and is comparable to that measured before for CdSe QDs ($DCP > 50\%$ at $B = 30$ T) [87, 88, 78]. Differences among various colloidal nanocrystals can be caused by material properties and light scattering effects.

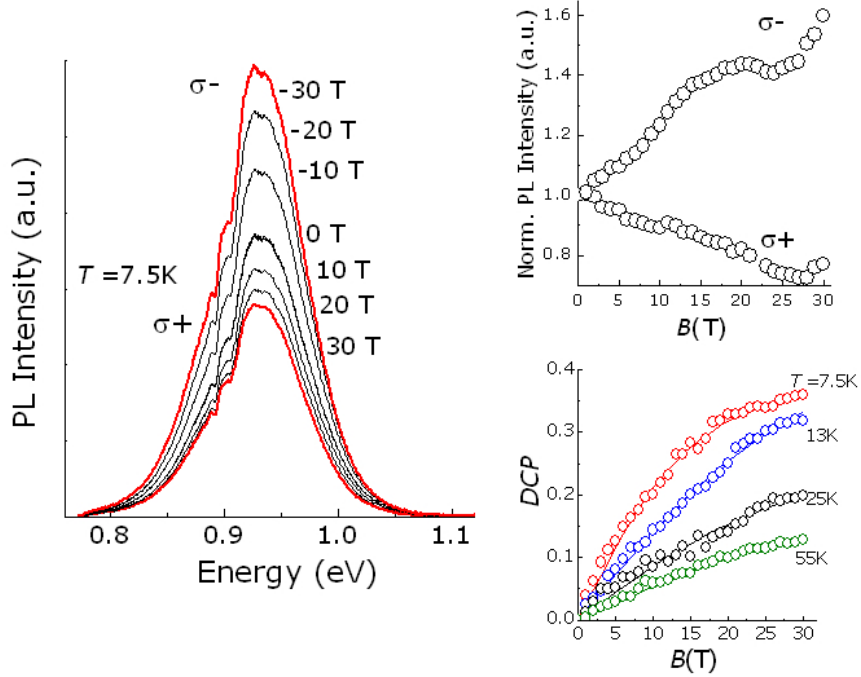


Figure 6.3: Circular-polarized PL emission acquired at 7.5K and various magnetic fields for PbS QDs with average diameter $d = 4$ nm. The top inset shows the PL peak intensities in σ^- and σ^+ circular polarization as a function of the applied magnetic field at 7.5 K. The bottom inset shows the B -dependence of the DCP at various temperatures. Continuous lines are fit to the data by the model described by equation 6.3

To provide a quantitative description of the DCP data, we use the semiclassical model of ref. [89]. The Zeeman interaction of the electron and hole spin with the magnetic field splits the degenerate bright exciton states with total angular momentum $+1$ and -1 . The lowest optically allowed bright excitons correspond to excitons with spin = ± 1 and Zeeman energy splitting given by $\Delta E_\theta = g_X \mu_B B \cos \theta$, where g_X is the exciton g -factor, μ_B is the Bohr magneton and θ represents the angle between B and the preferential axis of polarization of the nanocrystal. Since in these transitions electrons and holes have both spin

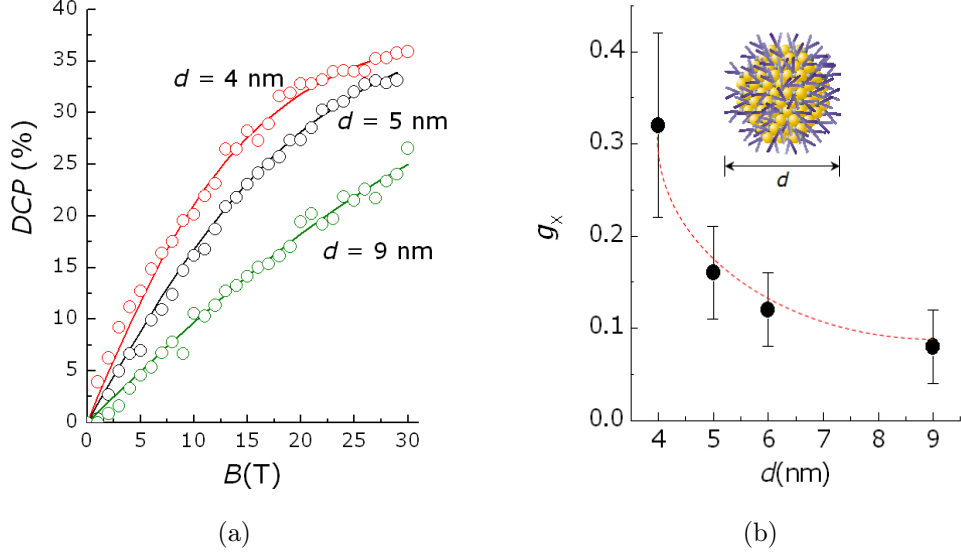


Figure 6.4: a) B -dependence of the degree of circular polarization of the QD PL emission at low temperature for PbS QD samples with different values of d . Continuous lines are fit to the data by the model described in the main text. b) Dependence of the exciton g -factor on the average QD diameter d ($T < 8\text{K}$). The line is a guide to the eye.

$s=1/2$ or $s=-1/2$, the exciton g -factor can be also expressed as $g_X = |g_e - g_h|$. To account for the random orientation of the nanocrystals, the value of θ is averaged out to generate the following expression for the DCP [90]:

$$DCP = \frac{\int_0^\pi 2 \cos\theta \tanh(\Delta E_\theta/2k_B T) \sin\theta d\theta}{\int_0^\pi (1 + \cos^2\theta) \sin^2\theta d\theta} \frac{1}{1 + \frac{\tau_s}{\tau}}. \quad (6.3)$$

Here τ_s and τ represent the spin relaxation and recombination time of the exciton, respectively. It can be seen from equation 6.3 that at low B , i.e. $\Delta E_\theta \ll k_B T$, the DCP exhibits a linear dependence on B given by $g_X \mu_B B / [4k_B T (1 + \tau_s/\tau)]$. In contrast, in the limit of high B , i.e. $\Delta E_\theta \gg k_B T$, the DCP exhibits only very small changes and approaches a constant value proportional to $1/(1 + \tau_s/\tau)$. The calculated dependences of the DCP on B and T reproduce accurately the measured data. The $DCP(B)$ curves at various T are shown in the bottom inset of Figure 6.3 for a QD sample with average diameter $d=4$ nm.

The calculated and measured low temperature $DCP(B)$ curves for QD samples with different d are shown in Figure 6.4a.

Let's first consider the QD sample with $d = 4$ nm (Figure 6.3). At $T = 7.5$ K and 13.5 K, the least-square fit to the data by equation 6.3 is obtained with $g_X = 0.32 \pm 0.05$ and $\tau_s/\tau = 0.8 \pm 0.2$, and $g_X = 0.28 \pm 0.05$ and $\tau_s/\tau = 0.6 \pm 0.2$, respectively. At higher T , these parameters cannot be determined univocally due to the change in the form of the measured $DCP(B)$ curve. We have also derived the $DCP(B)$ curves by considering the PL intensity at different energies within the same QD PL band, see for example the $DCP(B)$ curves of Figure 6.5. For each curve, the measured data are reproduced accurately by the calculated dependence of the DCP on B with the same value of g_X (within the error bar), but slightly different values of τ_s/τ .

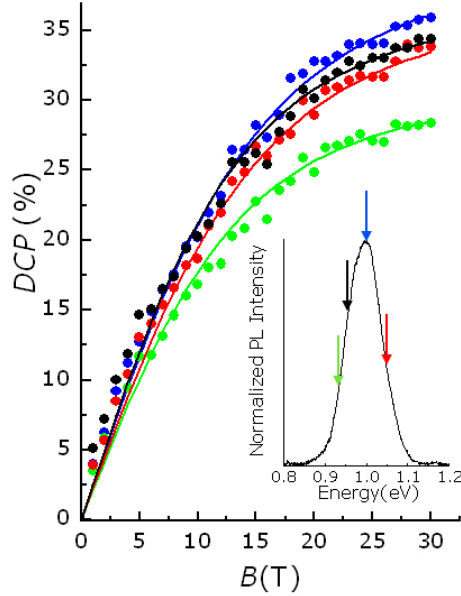


Figure 6.5: B dependence of the DCP at various energies for one of our PbS QD samples ($T = 4.2$ K). Continuous lines are fit to the data by the model described in the text. Inset: QD PL spectrum with lines showing the energy at which the DCP was measured.

The data and analysis for all QD samples indicate a systematic increase of g_X with decreasing the average QD diameter. The value of g_X increases from $g_X = 0.12 \pm 0.05$ for $d = 9$ nm to $g_X = 0.32 \pm 0.05$ for $d = 4$ nm ($T < 8$ K), see Figure 6.4b. An increase of g_X with decreasing the QD size was reported for InP nanocrystals [80]; also, measurements on self-assembled InGaAs/GaAs QDs have shown a high degree of tunability of g_X by varying the QD morphology [80] or by applying an external electric field [79]. These effects arise from quantum confinement and material properties [78], but were never reported before for PbS QDs. Also, since for bulk PbS it was shown that $g_X \sim 0$ [91], we infer that the quantum confinement of carriers in PbS QDs has a strong effect on the g -factor of the exciton.

These results are relevant to recent calculations of the excitonic exchange splitting and radiative lifetime of lead chalcogenides QDs, which have predicted a novel type of excitonic exchange splitting pattern that is highly sensitive to the QD size [76]. Although our measurements on the QD ensemble do not reveal the exciton fine structure, the polarization data indicate a systematic dependence of the exciton polarization properties on the QD size, which has never been reported before for this type of nanocrystals. We also note that the values of g_X derived from the analysis of the *DCP* correspond to Zeeman energy splittings ΔE less than 0.5 meV at $B = 30$ T. These energies are much smaller than the estimated diamagnetic shift of the QD PL emission at $B = 30$ T ($2 \text{ meV} < \delta E < 10 \text{ meV}$).

Therefore we conclude that the Zeeman splitting of the bright exciton cannot be the only physical mechanism counteracting the diamagnetic shift of the QD PL emission. We propose that the admixing of the dark and bright exciton states at high B could provide a plausible explanation for the red-shift and decrease in intensity of the QD PL emission observed at high B (Figure 6.2).

This phenomenon merits further investigation by optical spectroscopy of individual QDs and life-time measurements to resolve the exciton fine structure and also to identify alternative recombination processes, i.e. phonon-assisted peaks, emission related to surface states, etc. Model calculations are also needed to describe the effect of a magnetic field on the exciton fine structure in PbS QDs and other IV-VI QDs, such as PbSe QDs, reported in the recent literature [92].

6.5.1 Resonant excitation of the QDs

An external magnetic field induces small changes in the PL spectra, which can be hard to reveal due to the PL broadening. The homogeneous broadening is caused by lattice vibrations and can be reduced by cooling the sample [86]. In an attempt to reduce the inhomogeneous broadening caused by the random distribution of sizes and shapes of the QDs, we performed PL experiments by exciting resonantly the QDs, i.e. by using a laser with $\lambda = 1064$ nm ($E = 1.165$ eV). In this experiment, only QDs whose energy levels coincide with the energy of the laser and smaller should be excited.

Figure 6.6 shows the PL spectra of PbS QDs ($d = 4$ nm) excited by an Ar^+ laser ($\lambda = 514$ nm/ 2.41 eV) and by an infrared laser ($\lambda = 1064$ nm/1.165 eV) at RT ($T = 300$ K). The two spectra are almost identical. By cooling the system down to 4 K, we have observed a narrowing of the PL emission in both spectra. However, there was no narrowing in the spectra because of the resonant excitation. The top and bottom insets of Figure 6.6 display the peak position and the FWHM as a function of temperature for the two excitation conditions. The two graphs show the same T -dependence.

The similarity in the spectra suggest that although the resonant excitation selects a small number of QDs in the ensemble, electron-hole recombination

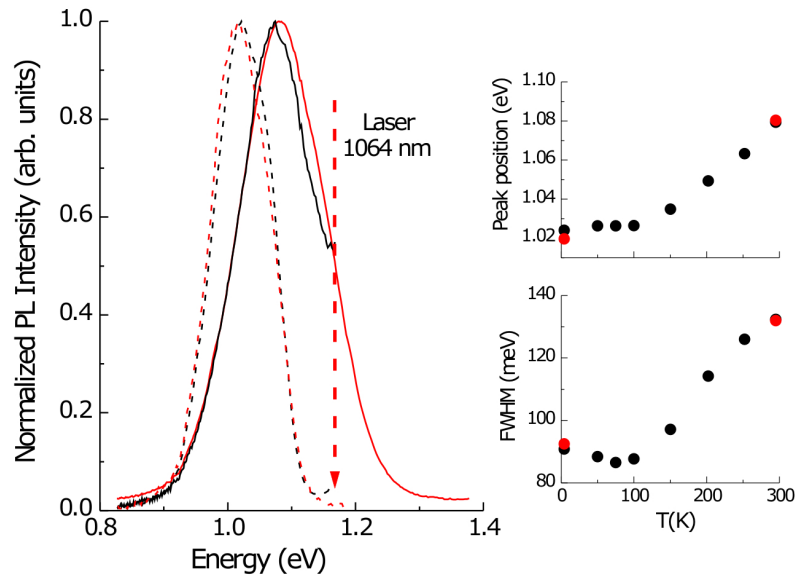


Figure 6.6: PL spectra for resonant (red line) and non resonant (black line) excitation at low T (dashed lines) and RT (solid lines) for QDs with $d = 4$ nm. The insets show the T -dependence of the energy and FWHM of the QD PL emission for resonant (red) and non-resonant (black) excitation.

takes place in all QDs. This could be explained by dipole-dipole coupling between the QDs [93], a phenomenon that merits further investigation.

Chapter 7

Electronic Transport in PbS QDs

This chapter explores the electronic conduction in thin films based on PbS QDs and TiO₂ matrices impregnated with PbS QDs. Current - voltage characteristics and temperature dependent conductivity measurements are presented. Also, the photovoltaic response of solid state devices based on porous TiO₂ and PbS QDs is discussed.

7.1 Thin films of PbS QDs

Thin films of PbS QDs were produced by drop-casting the QDs from solution into interdigitated devices, followed by water evaporation in air. Prior to the deposition of the QDs, the current leakage between the contacts was examined. For a 1 μ m gap device, see figure 3.5a, it was estimated to be less than 90 pA at biases up to 20 V. Using AFM, the electrode thickness was measured to be about 80 ± 5 nm corresponding to approximately 20 monolayers of PbS QDs with diameter $d = 4$ nm that are closely packed together. For the shortest transport path, electrons have to tunnel through ~ 200 nanocrystals, which is

the number of QDs in each monolayer.

Current-voltage characteristics $I(V)$ of samples based on QDs with different size, capping ligands and device gaps ($L = 0.15, 1$ and $10 \mu\text{m}$) were studied in detail. In most of the studied samples, the $I(V)$ curves under negative and positive biases were highly symmetric (see Figure 7.1) and a very small hysteresis effect was observed when sweeping the bias at a rate of 0.1 V/s . In this section we focus on 4nm diameter thiol-capped PbS QDs on $1 \mu\text{m}$ gap devices, which we refer to in the text as sample A.

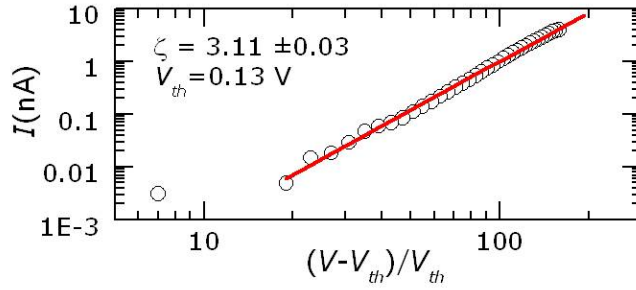
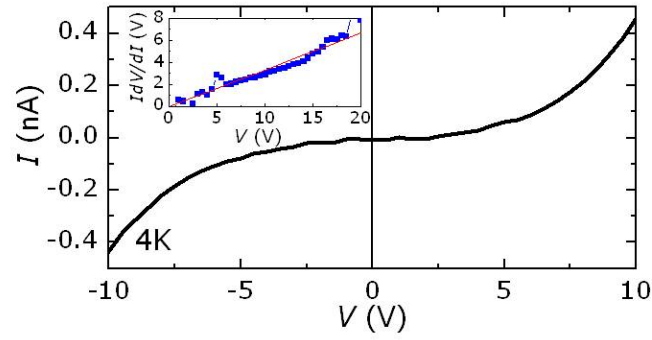
Figure 7.1 shows the $I(V)$ characteristics for this device at $T = 4.2 \text{ K}$ and 295 K . The $I(V)$ s reveal a clear non-ohmic behaviour and a rapid increase of the current for biases above a threshold voltage (V_{th}). With increasing the applied voltage, the current increases according to a power law dependence, which can be described by the formula proposed by Middleton and Wingreen (MW) [94]:

$$I = I_0 \left(\frac{V - V_{th}}{V_{th}} \right)^\zeta, \quad (7.1)$$

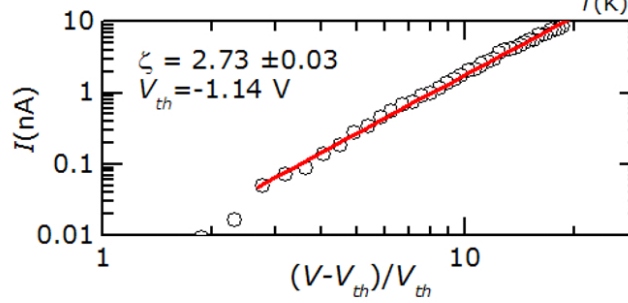
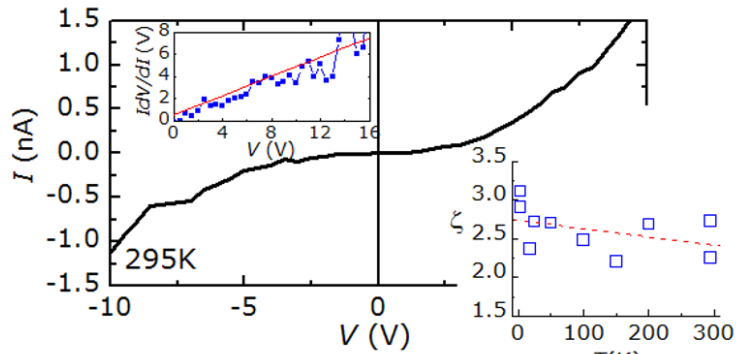
where ζ is a scaling exponent larger than unity, V_{th} is a constant voltage and I_0 is a constant current. This model was originally developed to describe the non-linear charge transport of a square array of small metallic dots coupled by capacitors between two metallic plate contacts and has been used widely to describe the electronic transport in disordered systems [95, 96].

The threshold voltage can be determined by plotting $I(dV/dI)$ versus V . From the top insets of Figure 7.1a, we find that $V_{th} \approx 130 \text{ mV}$ at 4 K and this value tends to decrease at higher temperatures. A similar trend was reported in the literature for Au nanoparticles [97] and PbSe QDs [98].

By plotting the measured current against the reduced voltage $(V - V_{th})/V_{th}$ on



(a)



(b)

Figure 7.1: $I(V)$ characteristics of sample A at a) 4 K and b) 295 K. The top insets in the two graphs show $I(dI/dV)$ versus V , from which V_{th} can be extracted accurately. The bottom graphs represent I versus the reduced voltage $(V - V_{th})/V_{th}$ and display the power-law dependence and the scaling exponent ζ . The right hand inset shows the dependence of ζ on temperature.

a logarithmic scale, we can identify a linear relation over 3 orders of magnitude, see Figure 7.1. A similar behaviour was observed in all our samples. For the sample of Figure 7.1, the value of ζ was found to depend on temperature and to be in the range $2.25 < \zeta < 3.00$. The values of ζ are similar to those ($2.1 < \zeta < 2.7$) reported earlier for percolation through a system with a dimensionality higher than 2 [56] and to those ($2.5 < \zeta < 4.5$) observed in oleic acid and trioctylphosphine capped colloidal PbSe QDs [99]. The right hand inset of Figure 7.1b shows the variation of ζ with temperature. It can be seen that the value of ζ hardly changes with variations of temperature.

QDs in a thin film couple with each other through a capacitance C , which can be calculated from the classical formula of a parallel plate capacitor, i.e. $C = A\varepsilon_r\varepsilon_0/a$, where a is the distance between the plates, A is the area of the parallel plates and ε_r is the material dielectric constant. We assume that the average distance between two QDs is $a \simeq 1\text{nm}$, which corresponds to 2 layers of thiols (4.3 \AA each [100]), we use $\varepsilon_r = 2.1$ for thiols [101] and consider a spherical QD of diameter $d = 4\text{nm}$ and a sphere-cap area $A = 10^{-17} \text{ m}^2$. The facet area of each QD contributes to the capacitance with $C \simeq 10^{-19} \text{ F}$. The nanocrystal self-capacitance, C_0 , can be calculated from $C_0 = 2\pi\varepsilon_0\varepsilon_r d$. Thus a 4nm PbS QD gives a capacitance $C_0 \sim 4 \times 10^{-18} \text{ F}$. These small self and mutual capacitances are responsible for relatively large charging energies of the QDs. The Coulomb charging energy of a QD can be calculated from the relation $E_C = e^2/2(2C + C_0)$. Using the values of C_0 and C , we find that $E_C \simeq 20 \text{ meV}$. At low temperature, the electron has to overcome this energy in order to conduct. The corresponding temperature equivalent to E_C is $T \simeq 245 \text{ K}$, which may explain why the threshold bias for conduction, V_{th} , decreases with increasing T . This regime is known as Coulomb blockade regime.

7.1.1 Comparing devices with different electrode spacing

In addition to the $1\ \mu\text{m}$ gap device, two more sets of samples with different gaps between the electrodes were studied, i.e. with $L = 0.15$ and $10\ \mu\text{m}$. The corresponding junction areas are $3\ \mu\text{m}^2$ and $200\ \mu\text{m}^2$, respectively. In general, the $I(V)$ characteristics of both samples were found to be similar to those observed in the $1\ \mu\text{m}$ gap device. The current in the $0.15\ \mu\text{m}$ device follows the power law dependence up to three orders of magnitudes with values of ζ similar to those found in the $1\ \mu\text{m}$ gap device. On the other hand, the $10\ \mu\text{m}$ gap devices exhibit a smaller value of $\zeta \approx 1$, a larger hysteresis effect and a higher irreproducibility. Figure 7.2 shows the dependence of I on the applied electric field F for samples with $L = 1, 0.15, 10\ \mu\text{m}$ at room temperature. Here $F = V/L$. Data in Figure 7.2 reveal no systematic dependence of the current on the electrode spacing.

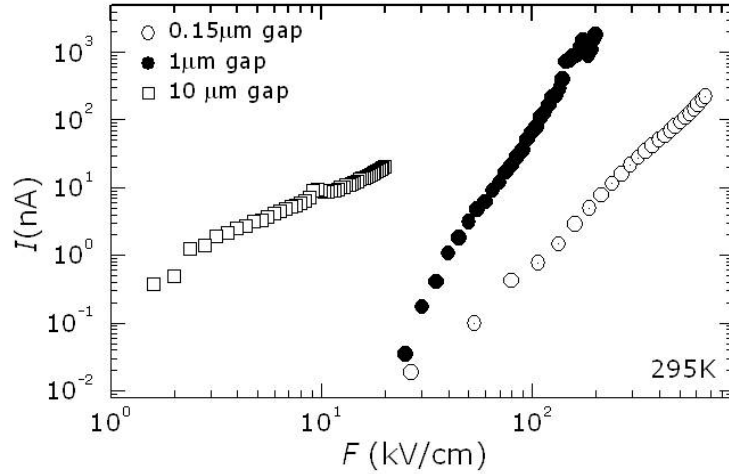


Figure 7.2: Log-log plots of the current versus electric field $F = V/L$ for three samples of different gap spacing: $10\ \mu\text{m}$ (open squares), $1\ \mu\text{m}$ (black dots) and $0.15\ \mu\text{m}$ (open circles).

In most of the measured samples, the current showed an enhancement with increasing temperature, but mainly at high applied biases. Figure 7.3 displays

the temperature dependence of the current measured at 4 different biases. By plotting the current against the reciprocal temperature at a fixed bias, it can be seen that the current is well described by $I = I_0 \exp(-\Delta E/k_B T)$, where I_0 is a pre-exponential factor, ΔE is an activation energy, k_B is Boltzmann constant and T is the lattice temperature. The activation energy was found to be $\Delta E = 20 \pm 5$ meV at high temperature (>100 K). The extracted activation energy is in a good agreement with the charging energy $E_C = 20$ meV calculated before. We note that other mechanisms such as the release of carriers from localized trapping centres can also contribute to the measured T -dependence of the current. The fitting in Figure 7.3 does not cover the whole range of temperature and the deviation from an exponential T -dependence at low temperatures suggests the presence of more than one mechanism of conduction.

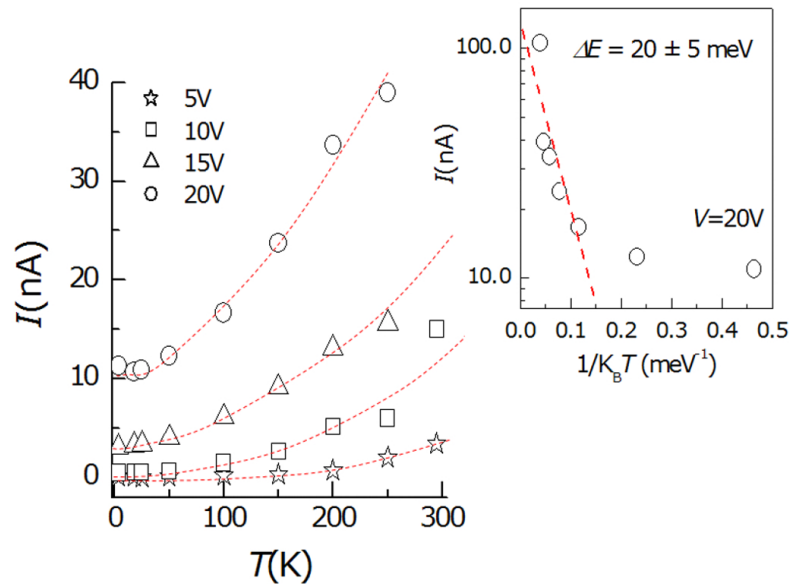


Figure 7.3: Temperature dependence of the current at different biases for a PbS thin film on a $1 \mu\text{m}$ gap device. Lines are guides to the eye. The inset shows the dependence I on $1/k_B T$ at $V=20$ V. The red dashed line is a fit to the data in the range of temperature 100 to 300 K, according to the relation $I = I_0 \exp(-\Delta E/k_B T)$.

Since the conductivity of the PbS QD is very small, its current-voltage characteristics can be dominated by space-charge effects and carrier trapping into

defect states. These phenomena can be accounted for by two models, the Poole-Frenkel model [102, 103] and the Mott-Gurney model [102] describe in section 7.1.2.

7.1.2 Space charge and Frenkel effect

The Poole-Frenkel model is widely used to describe the conduction in metal-insulator-metal systems. This model treats the lowest energy levels of the insulator as trap levels. Carriers that are injected from the metal into the insulator can get trapped in these levels. These carriers can be released into the conduction band and contribute to the current under a large applied electric field and/or the assistance of phonons.

The electric field F causes the potential around the defect to bend down on one side, thus reducing the energy required for an electron trapped into the defect to be released into the conduction band [102]. Figure 7.4 shows a schematic diagram of the Poole-Frenkel mechanism. The black curves represent the Coulomb barrier E_0 in the absence of electric field. This is reduced by E_A under the influence of the electric field (see blue dashed line).

The space-charge limited current model to describe the current-voltage relation for a metal-insulator-metal system was first introduced by Mott-Gurney [102]. The electron current density J is found to be equal to $J = (9/8)\mu\varepsilon_r\varepsilon_0(V^2/L^3)$ for a defect free system, where μ is the carrier mobility, V is the applied voltage and L is the separation between the electrodes. The Mott-Gurney model was later modified to include the Frenkel

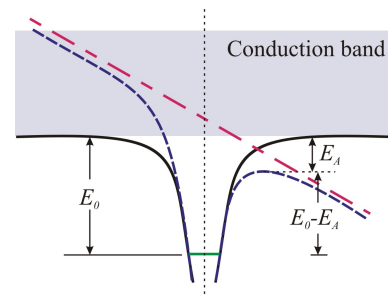
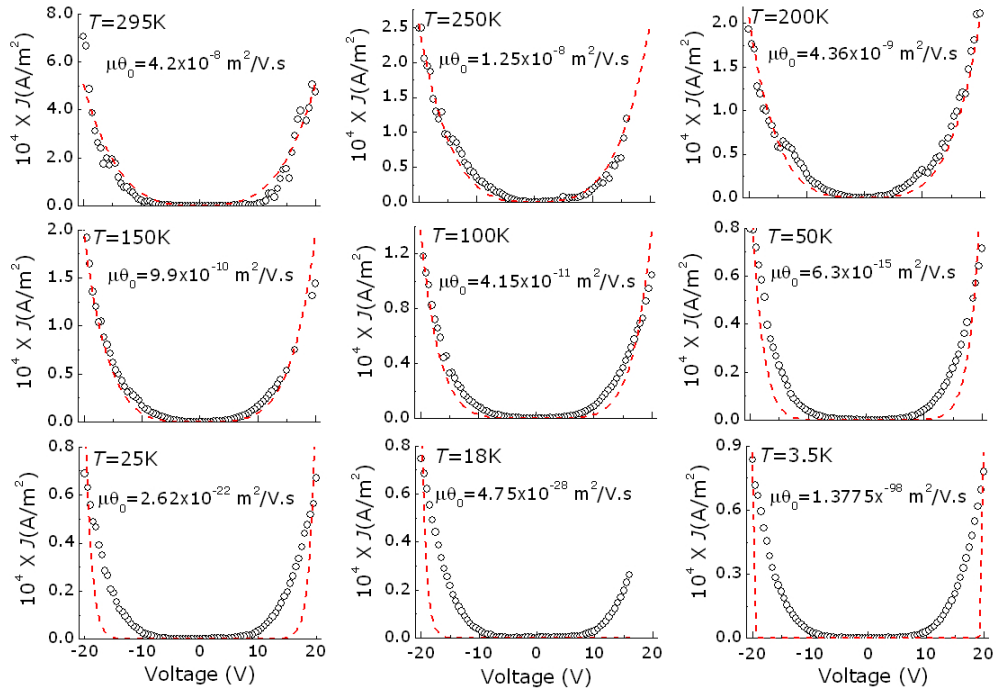
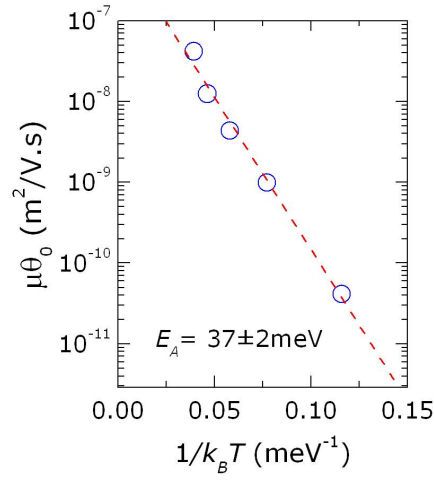


Figure 7.4: Poole-Frenkel effect. The black solid line represents the potential energy without the external field, while the blue dashed line represents the effect of an electric field on the potential. Reproduced after [102].



(a)



(b)

Figure 7.5: a) Current density J versus applied voltage for the $1 \mu\text{m}$ gap device at different T . Red dashed lines represent the fits according to the Poole-Frenkel model. b) The product of the effective mobility and the fraction of free carriers ($\mu\theta_0$) as a function of the reciprocal thermal energy in the T -range 77- 300K.

effect, i.e. the effect of carrier trapping on the current. This gives:

$$J = \frac{9}{8} \mu \varepsilon_r \varepsilon_0 \frac{V^2}{L^3} \theta_0 \exp \left\{ \frac{0.891}{k_B T} \sqrt{\frac{e^3 V}{\pi \varepsilon_r \varepsilon_0 L}} \right\} \quad (7.2)$$

where $\theta_0 = \frac{N_C}{N_t} \exp \frac{-E_0}{k_B T}$ [102], N_C is the effective density of states in the conduction band, N_t is the trap density and E_0 represents the depth of the trap level measured relative to the conduction band minimum. The fraction of free carriers $\frac{\rho_f}{\rho_t + \rho_f}$ that contributes to the current is also given by $\theta_0 \exp \frac{0.891}{k_B T} \sqrt{e^3 V / \pi \varepsilon_r \varepsilon_0 L}$ and depends on T and the energy depth of the trap. Here ρ_f, ρ_t are the free and trapped carrier charge densities, respectively.

Although this model was not developed for semiconductor nanocrystals or organic materials, it has already been used to describe the conduction in many high resistivity materials [104]. We now consider the applicability of this model to our data. We note that at low T (< 100 K) capacitance effects dominate the conduction and are not described by the Poole-Frenkel and Mott-Gurney model.

Figure 7.5a shows the measured and calculated $J(V)$ curves at various T for one of our PbS QD films with $L = 1 \mu\text{m}$. Each curve was fitted to the model using just one fitting parameter, i.e. $\mu\theta_0$, which represents the product of the effective carrier mobility and the fraction of free carriers. It can be seen that the data are well described by this model at $T > 100$ K. In particular, the value of $\mu\theta_0$ is found to increase with increasing T . Figure 7.5b shows the dependence of $\mu\theta_0$ on $1/k_B T$. This suggests an Arrhenius type plot with an activation energy $E_A \approx 40$ meV. Since $\mu\theta_0 = \mu(N_C/N_t) \exp[-E_0/k_B T]$, if we assume that the effective carrier mobility μ does not change with T , then the activation energy extracted from an analysis represents the depth of the defect levels. Thus our data and analysis suggest that at $T > 100$ K, the conduction is limited by space

charge and the activation of carriers out of traps.

Although our discussion focused on the electron transport, a similar picture can apply to holes. As our PbS are not intentionally p or n-type doped, both type of carriers can contribute to the conduction.

7.1.3 Current noise

An interesting phenomenon was observed on the $I(V)$ characteristics of PbS QDs films at high temperatures ($T > 100$ K). Fluctuations in the current emerged in the measured data. Figure 7.6 shows two current-voltage loops at low and high T . The top figure shows a 95% fluctuation in the current at high temperature ($T = 237$ K). This was reduced to less than 15% at 4 K. To investigate this phenomenon in more detail, we monitored the temperature dependence of the current at a fixed bias. As shown in Figure 7.6b, the fluctuation in the current, ΔI , is strongly enhanced at high T . By plotting the dependence of ΔI on $1/k_B T$, we find a thermally activated behaviour for ΔI with a characteristic activation energy E_A in the range 10 - 80 meV.

The noise in the data could be related to the thermally activated Johnson-Nyquist noise observed in any electrical conductor regardless of the applied bias. The noise can also be related to other mechanisms such as carrier trapping and de-trapping from QD states. More studies have to be carried out using QDs with different capping ligands to explore the role of surface states in the conduction.

7.1.4 Photoresponse

Photo-generated carriers can contribute to the current if they have a recombination time that is long enough for carriers (electron/hole) to reach the electrodes.

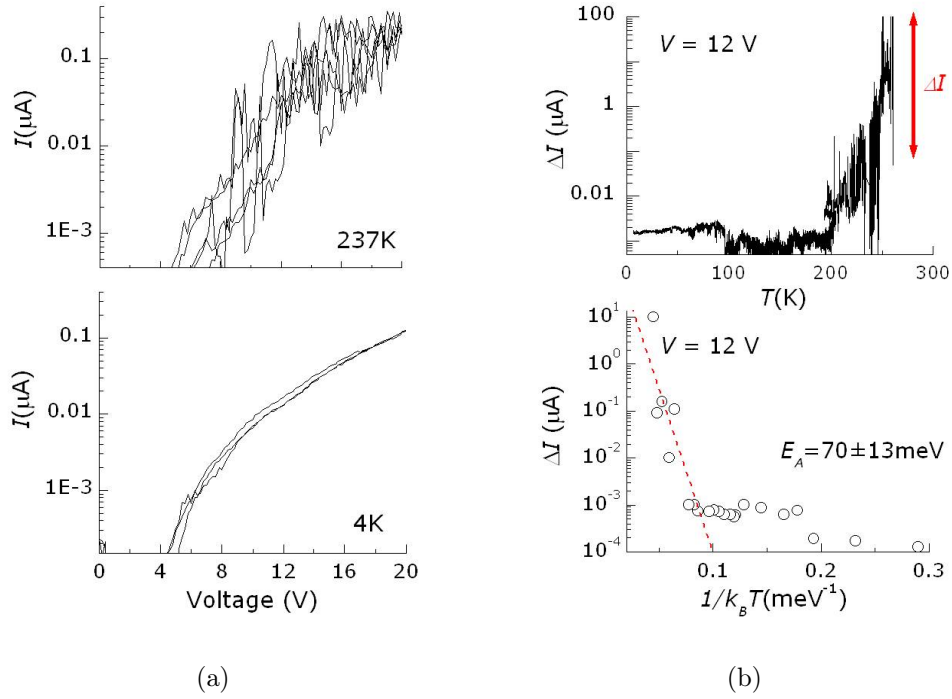


Figure 7.6: a) A comparison between $I(V)$ loops at $T=237\text{K}$ (top) and $T=4\text{K}$ (bottom) for one of our samples. b) Temperature dependence of I (top) and of ΔI on $1/k_B T$ (bottom).

Several parameters can affect the photocurrent: the power and wavelength of the excitation light, the electric field, the mechanism of conduction and the characteristic time for carrier recombination [105]. In our PbS films, we measured a very poor response to photoexcitation with light of wavelengths $\lambda = 514\text{ nm}$ and 633 nm and power densities up to 290 W/cm^2 . On the other hand, in all samples we also observed a strong PL signal, thus suggesting that the time for carrier recombination is shorter than the time required for carriers to reach the electrodes and to contribute to the current. Thus a different approach should be used to improve the photocurrent in films based on PbS QDs. This is discussed in section 7.2.

7.2 Titanium Dioxide impregnated with PbS QDs

In conventional p-n junctions, e.g. silicon-based solar cells (SC), both the photo-generation of carriers and carrier transport occur in the same semiconductor. In contrast, in Grätzel (dye sensitized) SCs, electron-hole photo-generation occurs in an efficient light absorbing material known as a sensitizer, while another material of a wider band gap, such as mesoporous titania (TiO_2), is responsible for delivering the carriers to the electrodes. In a traditional Grätzel SC, the sensitizer is mainly made of a thin film of dyes which is located between the TiO_2 and a liquid electrolyte gel or a solid to transport the photo-injected charges into the anode/cathode [106].

In this type of SCs, light absorption takes place in the dye layer, and the photo-generated electrons/holes are separated at the sensitizer/ TiO_2 interface. Electrons are injected into the conduction band of TiO_2 to be delivered into a top transparent electrode, e.g. fluoride-doped tin dioxide ($\text{SnO}_2:\text{F}$). These electrons are compensated again from the electrolyte in the other side of the sensitizer [106, 30].

The Grätzel SC was first introduced in 1991 [106] and developed dramatically during the past two decades. It attracted considerable interest because of its low fabrication cost and good solar conversion efficiency ($>15\%$). For optimum solar radiation harvesting, it is important to choose the right sensitizer. Thus with the limited availability of dyes with strong absorption in the NIR, the attention was drawn to other materials like colloidal nanocrystals and IV-VI semiconductors. PbS and PbSe QDs can emit in the NIR region of the electromagnetic spectrum, thus they can provide good sensitizers for this kind of SCs especially as $\sim 45\%$ of the sun power lies in the infrared region. To date, the maximum energy transfer efficiency achieved in the infrared region is about

4.2% [107, 108]. Different geometries have been used to make SC devices. The fabrication technique is rather simple. For example, a solar cell can be made by drop-casting, spin or spray coating a semiconductor nanocrystal solution on top of pre-deposited metallic electrodes on a substrate. In this work, we have investigated a device structure based on a mesoporous TiO_2 matrix impregnated with PbS nanocrystals. A photovoltaic response in the visible and near infrared wavelength range was obtained by exploiting the Schottky junction that forms at the interface between the PbS/ TiO_2 film and a metallic contact. This effect is described in section 7.2.2.

Titanium dioxide, also known as titania, is a crystalline semiconductor that can be found in nature or it can be synthesized. It has three crystalline phases: rutile, anatase and brookite. Anatase, for instance, has a tetragonal crystal structure with lattice constants $a = 3.785, 9.514 \text{ \AA}$, a crystal density of $3.79 - 3.97 \text{ g/cm}^3$ and it can be stable at relatively high temperatures [109]. Titania has been used as white pigments, optical coatings, solar cells and other applications [110, 111]. For solar cells, a porous titania with dyes or nanocrystals have been employed extensively [111]. Due to the large surface to volume ratio that porous TiO_2 provides, charge transfer processes and electronic coupling between the dots can be improved [112].

To date several studies of PbS/ TiO_2 as a photovoltaic device have been published [113]. However, the mechanism of photoconduction, transport and the optical properties are still largely unexplored. Moreover, most of the fabricated colloidal QDs devices were solution based solar cells, while the solid state ones are less studied. Recently, Pattantyus-Abraham et al [114] have studied the performance of colloidal PbS QD solar cells where a QD layer was deposited on top of a TiO_2 film to form a depleted heterojunction. They have achieved a solar conversion efficiency of up to 5.1% at air mass coefficient AM 1.5. The

following section describes a different approach to the fabrication and study of a solid state cell based on a TiO_2 matrix impregnated with PbS QDs.

7.2.1 Morphological and optical properties

A solar cell was fabricated by embedding a TiO_2/PbS matrix between two electrodes based on a fluorinated tin oxide (FTO) and an Ag-contacts. Figure 7.7a shows the PL and absorption spectra of the PbS/TiO_2 film. The PL peak position of the QD emission is slightly blue-shifted compared to that for the same dots deposited on a glass substrate. This could be attributed to the fact that smaller dots can be incorporated in TiO_2 more efficiently. However, no narrowing of the PL emission was observed at low or room temperature. This was observed to be identical for the bottom and the top sides of the sample. Visually, the color of the TiO_2 matrix was observed to change from white to a yellowish brown as it was impregnated with PbS QDs, see the top inset of Figure 7.7a. Correspondingly, the conventional TiO_2 absorption threshold at $\sim 500\text{nm}$ shifted towards the near-infrared region of the electromagnetic spectrum, i.e. at $\sim 1000\text{ nm}$ at room temperature.

A cross-section of the PbS/TiO_2 film was examined by SEM and EDX at Nottingham using an FEI Quanta 200 3D Dual Beam FIB/SEM system, while EDX spectra were taken using an Oxford Instruments ultra thin-window WDX detector. The elemental analysis and spatial maps of cross-sections of the PbS/TiO_2 film indicate that the PbS QDs impregnate the TiO_2 down to a depth of $\sim 60\mu\text{m}$ (see Figure 7.7b).

The top TEM image of Figure 7.7b presents a TEM image of the PbS/TiO_2 film cross-section, which highlights the randomly packed and interconnected TiO_2 nanoparticles mixed with PbS QDs. The top inset shows also a HRTEM

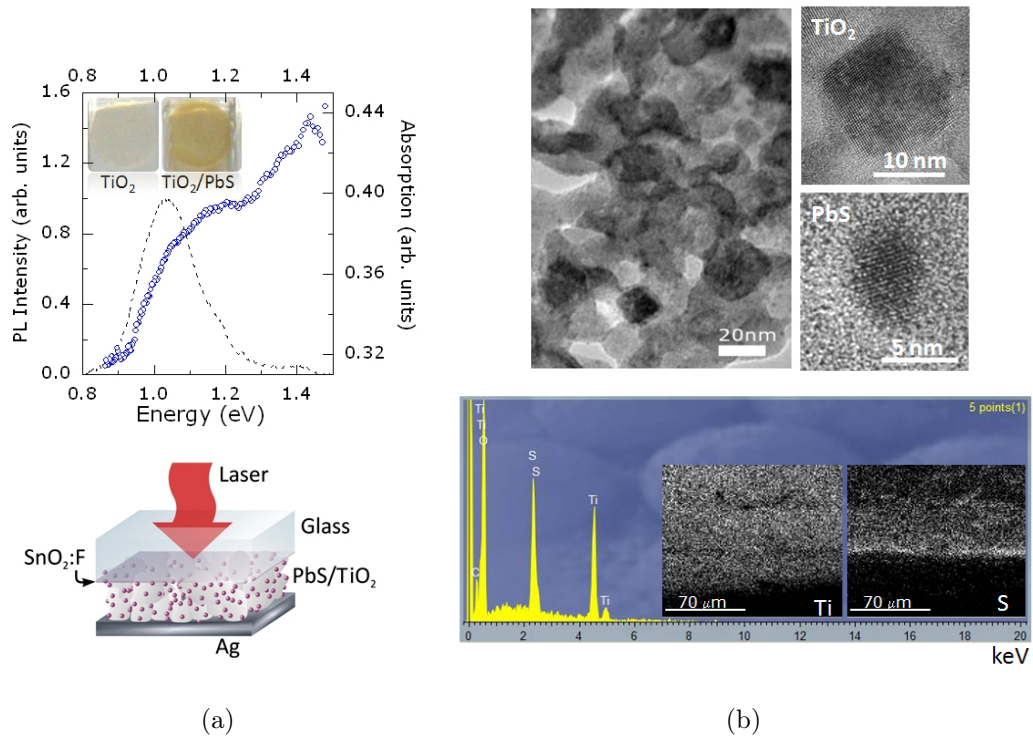


Figure 7.7: a) PL intensity (dashed black line) and absorption (blue circles) spectra of PbS/TiO₂ film. The inset shows an optical microscopy image of a TiO₂ film with (a yellowish brown) and without (white) PbS QDs. The bottom of the graph is a sketch of the device. b) TEM image of a cross-section of a PbS/TiO₂ film. The insets on the right show HRTEM images of a TiO₂ nanoparticle (top) and a PbS QD (bottom). The bottom graph is the EDX spectrum that shows the presence of S in the TiO₂ matrix. The two insets are EDX maps indicating the level of S compared to the level of Ti in the TiO₂ matrix.

image of a single TiO₂ nanoparticle. This has a round shape with a diameter $d = 20 \pm 2$ nm. The clearly defined lattice fringes have a spatial separation $a = 3.6 \pm 0.1$ Å, which is in good agreement with the interplanar distance of the (101) planes of bulk anatase ($a = 3.7$ Å) [109]. The bottom inset of Figure 7.7b shows a HRTEM of a single PbS QD with a diameter $d = 5 \pm 2$ nm, and lattice fringes whose spatial separation is of 2.05 Å. This corresponds to the interplanar distance of the (220) planes of bulk PbS.

7.2.2 Photovoltaic effect

The dark current and the photocurrent of a pure TiO_2 film, i.e. without PbS QDs, was observed to be approximately symmetric under forward and reverse biases, and to remain very small over an extended range of biases. On the other hand, the current increases by up to two orders of magnitude in the PbS/ TiO_2 film.

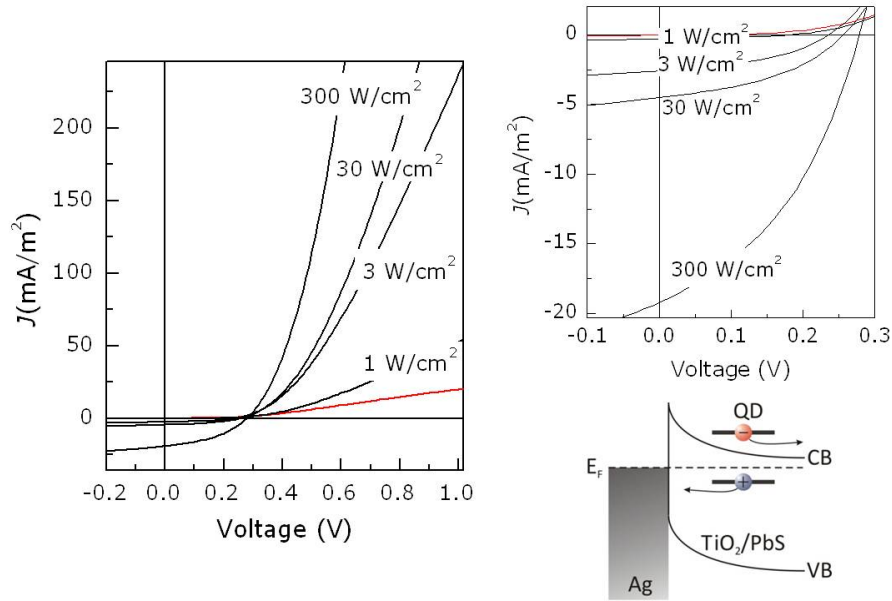


Figure 7.8: $J(V)$ characteristics of the PbS/ TiO_2 device in the dark (red line) and under laser illumination ($\lambda = 633\text{nm}$) with power densities in the range between 1 to 300 W/cm^2 . The top inset reveals the $J(V)$ curves of the same device zoomed to the fourth quadrant area. The bottom inset is a sketch of the energy band diagram at zero bias.

Figure 7.8 shows the room temperature current density-voltage $J(V)$ characteristics of one of the PbS/ TiO_2 devices in the dark and under illumination with powers up to 300 W/cm^2 from a He-Ne laser ($\lambda = 633\text{nm}$). The photoexcitation of the PbS/ TiO_2 film produces a photovoltaic effect (see the inset of Figure 7.8), which is not observed in the TiO_2 film. For the sample shown in Figure 7.8, the open-circuit voltage is $V_{OC} \simeq 0.27\text{ V}$ and the short circuit cur-

rent density is $J_{SC} = 19 \text{ mA/m}^2$. The value of J_{SC} increases by increasing the power of the incident light. A photovoltaic effect is also observed for excitation of the PbS/TiO₂ film with a NIR light with λ up to 1000 nm, which is close to the absorption onset of the PbS QDs. Devices based on QDs of different size and/or with different capping ligands (i.e. thioglycerols and dihydrolipoic acids) exhibit similar $J(V)$ characteristics, although J_{SC} tends to be larger for smaller QDs ($d < 3 \text{ nm}$). The dependence of the $J(V)$ at RT on the laser power at low biases is shown in the inset of Figure 7.8. The curves give an indication about the solar cell performance under different illumination conditions. The conversion efficiency was found to be less than 1%.

The rectification effect in the $J(V)$ indicates the existence of a Schottky barrier at the interface between the PbS/TiO₂ film and the Ag-electrode. The bottom inset of Figure 7.8 shows the a sketch of band bending of the film-metal junction at zero bias. Since the work function of Ag is $q\phi_m \sim 4.5 \text{ eV}$ [115] and the electron affinity of TiO₂ is $q\chi \sim 3.9 \text{ eV}$ [116], the height of the Schottky barrier is $\phi_b = (\phi_m - \chi) = 0.6 \text{ V}$. The built-in potential for the n-type PbS/TiO₂ film should be smaller than ϕ_b , which is consistent with the open-circuit photovoltage $0.3 \text{ V} < \phi_b < 0.6 \text{ V}$ measured in all our samples. Since the position of the QD levels in TiO₂ is not known, we use simple arguments to provide a rough estimate. We use the energy of the absorption band of our PbS QDs and the electron affinity χ and energy gap (E_g) of bulk PbS ($q\chi = 4.6 \text{ eV}$ and $E_g = 0.42 \text{ eV}$ at $T = 300 \text{ K}$) and of TiO₂ ($q\chi = 3.9 \text{ eV}$) to estimate the energy position of the QD electron ground state relative to the conduction band minimum (CBM) of TiO₂. We expect that the QD electron ground state lies below or above the CBM of TiO₂ depending on the QD size, see Figure 7.8. Thus electrons on the QD ground and/or excited states can be resonantly transferred into the CB of TiO₂. These electrons are hence swept by the built-in electric field at the Schottky junction

into the positively biased FTO contact, whereas the holes move towards the negatively biased Ag-electrode.

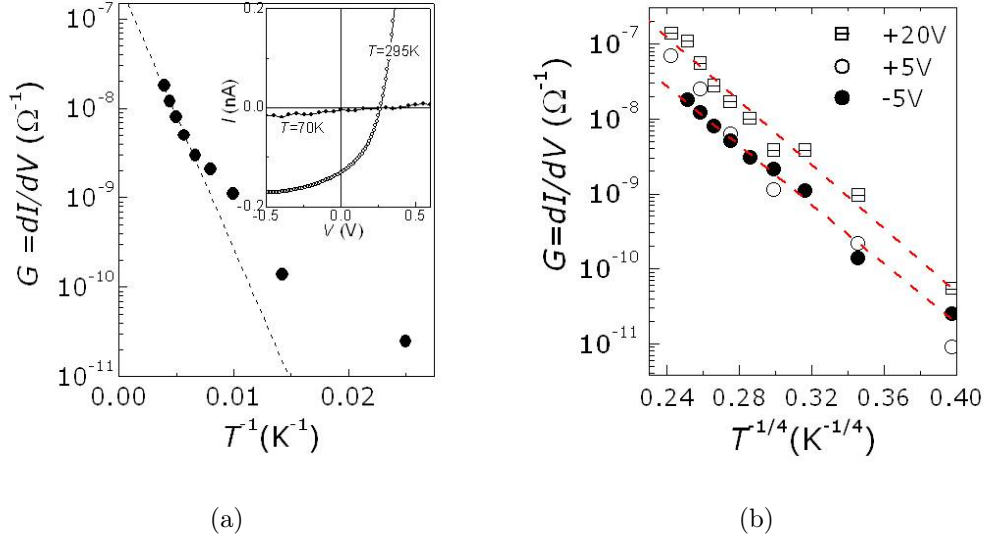


Figure 7.9: a) T -dependence of the differential conductance $G=dI/dV$ of the TiO_2/PbS film at $V=-5$ V. The dotted line represents the exponential dependence $\exp(-E_b/k_B T)$, where $E_b=55$ meV. The inset is the $I(V)$ at different temperatures. b) Differential conductance G as a function of $T^{-1/4}$ at different biases.

Hall conductivity measurements of the PbS/TiO_2 layers indicate that the contribution of the photogenerated holes to the current is much smaller than that of the electrons. Also, the photoconductivity is strongly sensitive to temperature and exhibits an exponential dependence of the type $\exp(-E_b/k_B T)$, see Figure 7.9. This dependence is a characteristic property of disordered crystals in which the conductivity is limited by grain crystal boundaries [117]. For our mesoporous TiO_2 matrix we find that the characteristic energy barrier for carrier transport is $E_b \simeq 55$ meV. However, this dependence does not fit the whole curve. To describe the whole T -range we consider the Mott's model of variable range hopping (VRH).

In the regime of VRH conduction, an electron tends to hop between levels with similar energy and the shortest possible hopping path. In the VRH, the

conductivity is directly proportional to the hopping probability P :

$$P \propto \exp\left(\frac{-2r}{a} - \frac{\Delta E}{k_B T}\right), \quad (7.3)$$

where r is the hopping distance and ΔE is the energy difference between energy states [118]. If the value of r is constant, this model represents the *nearest neighbour hopping* (NNH) mechanism where electrons hop to the closest energy level in the nearest particle. The separation between energy levels is $\Delta E \sim 3/g_0 4\pi r^D$, where D the dimensionality of the system and g_0 represents the density of states. With some approximations detailed in reference [119], the differential conductance $G = dI/dV$ can be expressed as:

$$G \propto P \propto \exp\left(-\frac{T_0}{T}\right)^{1/(D+1)}, \quad (7.4)$$

where T_0 is a constant temperature. This is known as Mott's law and according to this model, with an assistance of a phonon, an electron may hop to a remote energy level that is closer in energy than the one in the vicinity, if the latter has a larger energy difference. Mott VRH conduction (M-VRH) mechanism in 3D gives $G \propto T^{-1/4}$.

As shown in Figure 7.9b the differential conductance, $G = dI/dV$, shows a good agreement with the Mott's model, i.e. $G \sim \exp(-\frac{T_0}{T})^{-1/4}$. The VRH conduction mechanism was also reported before for a pure TiO_2 film [120]. This study indicates that the conduction is limited by the properties of TiO_2 .

The long-term exposure to the laser light and/or white light (halogen lamp) does not alter the properties of our devices. The structures remain stable and reproducible, and do not reveal the degradation phenomena reported previously in Schottky solar cells based on PbS QD films, which can undergo oxidation phe-

nomena [121]. This stability can be attributed to several factors: the presence of the nanoporous matrix around the nanocrystals limits the exposure of the PbS QDs to oxygen; the fabrication of our PbS/TiO₂ film does not require high-temperature treatment that would alter the stability of the capping ligands around the dots; also, our devices do not incorporate chemically aggressive electrolytes.

7.2.3 Summary

To sum up, our transport studies of thin films of PbS QDs revealed a non-linear dependence of the current on the applied bias, which we interpreted in terms of carrier transport in a random network of nanoparticles. To explain the measured data, we considered different effects: charging of the quantum dots, macroscopic capacitance effects and carrier trapping into defect states. No photocurrent was observed in these studies. We have also produced PbS/TiO₂ solar cell devices. These have revealed a stable and reproducible photovoltaic effect associated with the Schottky junction that forms at the interface between the PbS/TiO₂ film and a metallic contact. In all structures investigated, we have found a very poor conversion efficiency (<1%). This is associated with the poor conductivity properties of TiO₂. Thus further work is required to improve carrier conduction in this material system as well as to develop new approaches for an efficient electronic coupling of PbS quantum dots to the TiO₂ matrix.

Chapter 8

Conclusions and Prospects for Future work

This thesis provides valuable information about fundamental electronic and optical properties of thiol-capped, apoferritin encapsulated and DHLA-capped colloidal PbS QDs. It describes the photoluminescence, the magneto-photoluminescence and the temperature dependence of the photoluminescence for different PbS nanocrystals. Also, the electronic conduction is investigated for thin films of PbS QDs and TiO₂ matrices incorporating PbS QDs.

We have shown how thermal treatment of thiol-capped PbS colloidal quantum dots red-shifts their photoluminescence (PL) emission with respect to that of the as-grown QDs. We have also investigated the effect of the thermal treatment on the morphological properties of the QDs. The main observations can be summarized as follows. At low annealing temperatures (< 80°C), the annealing provides a simple strategy for controlling and narrowing the QD size distribution and photoluminescence emission; at higher annealing temperatures, the displacement of the thiol-ligands promotes the fusion of nearby quantum dots

thus leading to interconnected nanocrystals. This work was published in Nanotechnology (Nanotech. **20**, 315604 (2009)). These studies have contributed to identify the strong sensitivity of the QDs to high temperatures and the potential limitations in their implementation in devices operating at high temperatures. However, post-synthesis annealing to control the photoluminescence emission energy of the QDs still has great benefits in low temperature applications, for example in bioimaging studies.

Under magnetic fields up to 30T, the PL emission of PbS QDs has shown a large degree of circular polarization ($DCP=25-35\%$ at $B=30$ T and $T < 10$ K) and no diamagnetic energy shift. The data have indicated a strong exciton confinement in the QD and the existence of a population of spin-polarised excitons. Also, although the degree of PL polarization does depend on the QD size, the g -factor of the exciton exhibits a systematic dependence on the nanocrystal size with values that range from 0.1 to 0.3 at low temperature. Exciting PbS QDs resonantly does not reveal any narrowing in the FWHM of the PL spectra. These results were published in Physical Review B (Phys. Rev. B **82** 193302(4) (2010)).

The magneto-PL studies reported in this thesis have not included the DHLA-PbS QDs, which have smaller sizes and thus stronger confinement in comparison to thiol-capped QDs. Extending these studies to these QDs will be interesting for several reasons. These dots are smaller ($d < 3.5$ nm) and could be more suitable for single QD experiments because of the better sensitivity of the CCD detectors in the λ -range of the QD emission ($\sim 800-900$ nm).

The electronic conduction in PbS QD films was found to be strongly affected by capacitance effects and no photocurrent was observed in these systems. Thus to improve the photoconductivity of the films, a new system was explored. This

comprises a TiO_2 matrix impregnated with PbS QDs.

We have reported in this system a stable and reproducible photovoltaic effect. Further work is now required to improve carrier conduction in this material system as well as to develop new approaches for an efficient electronic coupling of PbS quantum dots to the TiO_2 matrix. This work was published in *Physica Status Solidi A* (*Phys. Status Sol. A.* **208** 2450-2453 (2011)). The relatively easy and cheap fabrication cost of this kind of device make TiO_2/PbS QDs a promising candidate for solar cell applications.

DHLA-PbS QDs, which were produced in the last year require further studies. The tendency of thiol-capped QDs to cluster after deposition, on a substrate, or after spin-coating, has inhibited the successful fabrication of samples containing a low density of QDs. Being smaller in size and with longer passivation ligand lengths, DHLA-PbS QDs could provide a better candidate for single quantum dot samples and spectroscopy studies. Single QD experiments will assist us in understanding the electronic properties of PbS QDs further and provide an insight about the exciton fine structure.

Finally, we have discovered that the encapsulation of a PbS nanocrystal into the hollow core of the apoferritin (Aft) protein provides a route for the self-assembly of the Aft-PbS nanocomposites into ordered arrays. The spherical shape of apoferritin and its uniform size can facilitate a crystalline packing of the PbS nanocrystals. Further work is required to control this process and exploit it in new device architectures.

Bibliography

- [1] Rogach, A. L., Eychmuller, A., Hickey, S. G., and Kershaw, S. V. *Small* **3**(4), 536–557 (2007).
- [2] Alivisatos, A. P. *Science* **271**(5251), 933–937 (1996).
- [3] Hollingsworth, J. and Klimov, V. *Semiconductor and Metal Nanocrystals: synthesis and Electronic and Optical properties*, chapter 'Soft' Chemical Synthesis and Manipulation of Semiconductor Nanocrystals, 1–64. New York: Marcel Dekker, Inc. (2004).
- [4] Zrenner, A. *Journal of Chemical Physics* **112**(18), 7790–7798 (2000).
- [5] McDonald, S. A., Konstantatos, G., Zhang, S. G., Cyr, P. W., Klem, E. J. D., Levina, L., and Sargent, E. H. *Nature Materials* **4**(2), 138–U14 (2005).
- [6] Hyun, B.-R., Chen, H., Rey, D. A., Wise, F. W., and Batt, C. A. *Journal of Physical Chemistry B* **111**(20), 5726–5730 (2007).
- [7] Zhao, X. S., Gorelikov, I., Musikhin, S., Cauchi, S., Sukhovatkin, V., Sargent, E. H., and Kumacheva, E. *Langmuir* **21**(3), 1086–1090 (2005).
- [8] Moriarty, P. *Reports on Progress in Physics* **64**, 297 (2001).

- [9] An, J. M., Franceschetti, A., Dudiy, S. V., and Zunger, A. *Nano Letters* **6**(12), 2728–2735 (2006).
- [10] Wei, S. H. and Zunger, A. *Physical Review B* **55**(20), 13605–13610 (1997).
- [11] Madelung, O. *Semiconductors: Data Handbook*. Springer, 3rd edition, (2004).
- [12] Butler, J. F., Calawa, A. R., and Rediker, R. H. *IEEE Journal of Quantum Electronics* **QE 1**(1), 4–7 (1965).
- [13] Kittel, C. *Introduction to Solid State Physics*. John Wiley and Sons Inc., 8th edition, (2005).
- [14] Hook, J. R. and Hall, H. E. *Solid state Physics*. John Wiley and Sons Inc., 2nd edition, (1995).
- [15] Bastard, G. *Wave mechanics applied to semiconductor heterostructures*. Halsted Press, les edition edition, (1988).
- [16] Bryant, G. W. *Physical Review B* **37**(15), 8763–8772 (1988).
- [17] Norris, D. J. *Semiconductor and Metal Nanocrystals: Synthesis and Electronic and Optical Properties*, chapter Electronic Structure in Semiconductor Nanocrystals, 65–102. Marcel Dekker Inc. (2004).
- [18] Marin, J. L., Riera, R., and Cruz, S. A. *Journal of Physics-Condensed Matter* **10**(6), 1349–1361 (1998).
- [19] Wise, F. W. *Accounts of Chemical Research* **33**(11), 773–780 (2000).
- [20] Brus, L. *The Journal of Physical Chemistry* **90**(12), 2555–2560 (1986).
- [21] Wang, Y., Suna, A., Mahler, W., and Kasowski, R. *Journal of Chemical Physics* **87**(12), 7315–7322 (1987).

- [22] Yoffe, A. D. *Advances in Physics* **50**(1), 1–208 (2001).
- [23] Sargent, E. H. *Advanced Materials* **17**(5), 515–522 (2005).
- [24] Yin, Y. and Alivisatos, A. P. *Nature* **437**(7059), 664–670 (2005).
- [25] Murray, C. B., Sun, S. H., Gaschler, W., Doyle, H., Betley, T. A., and Kagan, C. R. *Ibm Journal of Research and Development* **45**(1), 47–56 (2001).
- [26] Guzelian, A. A., Banin, U., Kadavanich, A. V., Peng, X., and Alivisatos, A. P. *Applied Physics Letters* **69**(10), 1432–1434 (1996).
- [27] Bakueva, L., Gorelikov, I., Musikhin, S., Zhao, X. S., Sargent, E. H., and Kumacheva, E. *Advanced Materials* **16**(11), 926–929 (2004).
- [28] Hines, M. A. and Scholes, G. D. *Advanced Materials* **15**(21), 1844–1849 (2003).
- [29] Harrison, M. T., Kershaw, S. V., Burt, M. G., Rogach, A. L., Kornowski, A., Eychmuller, A., and Weller, H. *Pure and Applied Chemistry* **72**(1-2), 295–307 (2000).
- [30] Tang, J. and Sargent, E. H. *Advanced Materials* **23**, 12–29 (2011).
- [31] Ellingson, R. J., Beard, M. C., Johnson, J. C., Yu, P. R., Micic, O. I., Nozik, A. J., Shabaev, A., and Efros, A. L. *Nano Letters* **5**(5), 865–871 (2005).
- [32] Ji, M. B., Park, S., Connor, S. T., Mokari, T., Cui, Y., and Gaffney, K. J. *Nano Letters* **9**(3), 1217–1222 (2009).
- [33] Du, H., Chen, C. L., Krishnan, R., Krauss, T. D., Harbold, J. M., Wise, F. W., Thomas, M. G., and Silcox, J. *Nano Letters* **2**(11), 1321–1324 (2002).

- [34] Abel, K. A., Shan, J., Boyer, J.-C., Harris, F., and van Veggel, F. C. J. M. *Chemistry of Materials* **20**, 3794 (2008).
- [35] Qu, F. Y., Silva, R. S., and Dantas, N. O. *Physica Status Solidi B-Basic Research* **232**(1), 95–99 (2002).
- [36] Dantas, N. O., Qu, F. Y., Monte, A. F. G., Silva, R. S., and Morais, P. C. *Journal of Non-Crystalline Solids* **352**(32-35), 3525–3529 (2006).
- [37] Lu, W., Kamiya, I., Ichida, M., and Ando, H. *Applied Physics Letters* **95**(8) (2009).
- [38] Turyanska, L., Patane, A., Henini, M., Hennequin, B., and Thomas, N. R. *Applied Physics Letters* **90**(10) (2007).
- [39] Hennequin, B., Turyanska, L., Ben, T., Beltran, A. M., Molina, S. I., Li, M., Mann, S., Patane, A., and Thomas, N. R. *Advanced Materials* **20**(19), 3592 (2008).
- [40] Cao, H. Q., Wang, G. Z., Zhang, S. C., and Zhang, X. R. *Nanotechnology* **17**(13), 3280–3287 (2006).
- [41] Lee, S. M., Jun, Y. W., Cho, S. N., and Cheon, J. *Journal of the American Chemical Society* **124**(38), 11244–11245 (2002).
- [42] Gfroerer, T. H. *Photoluminescence in Analysis of Surfaces and Interfaces: Encyclopedia of Analytical Chemistry*. John Wiley & Sons, Ltd, (2006).
- [43] Fox, M. *Optical Properties of Solids*. Oxford University Press, (2004).
- [44] Chamarro, M. A., Gourdon, C., and Lavallard, P. *Semiconductor Science and Technology* **8**(10), 1868–1874 (1993).
- [45] Giessibl, F. J. *Reviews of Modern Physics* **75**(3), 949–983 (2003).

- [46] Champness, P. *Microscopy Handbooks. Electron diffraction in the transmission electron microscope*, i–xiv, 1–170 (2001).
- [47] Goldstein, J., Lyman, C., Newbury, D., Lifshin, E., Echlin, P., Sawyer, L., Joy, D., and Michael, J. *Scanning Electron Microscopy and X-Ray Microanalysis*. Kluwer Academic, Plenum Publishers, 3rd edition, (2003).
- [48] Egelhaaf, S., Olsson, U., Schurtenberger, P., Morris, J., and Wennerstrom, H. *Physical Review E* **60**(5), 5681–5684 (1999).
- [49] Deng, D. W., Zhang, W. H., Chen, X. Y., Liu, F., Zhang, J., Gu, Y. Q., and Hong, J. M. *European Journal of Inorganic Chemistry* (23), 3440–3446 (2009).
- [50] Iwahori, K. and Yamashita, I. *Recent Research Developments in Biotechnology and Bioengineering* **7**, 41–68 (2005).
- [51] Junkin, M., Watson, J., Geest, J. P. V., and Wong, P. K. *Advanced Materials* **21**(12), 1247 (2009).
- [52] Lee, S. W., Mao, C. B., Flynn, C. E., and Belcher, A. M. *Science* **296**(5569), 892–895 (2002).
- [53] Storhoff, J. J., Mucic, R. C., and Mirkin, C. A. *Journal of Cluster Science* **8**, 179–216 (1997).
- [54] Rabani, E., Reichman, D. R., Geissler, P. L., and Brus, L. E. *Nature* **426**(6964), 271–274 (2003).
- [55] Solomon, G. S. *Journal of Electronic Materials* **28**(5), 392–404 (1999).
- [56] Dedigamuwa, G., Lewis, J., Zhang, J., Jiang, X., Mukherjee, P., and Witanachchi, S. *Applied Physics Letters* **95**(12) (2009).

- [57] Ma, W. Q., Sun, Y. W., Yang, X. J., Jiang, D. S., and Chen, L. H. *Nanotechnology* **17**(23), 5765–5768 (2006).
- [58] Liu, C., Kwon, Y. K., and Heo, J. *Applied Physics Letters* **90**(24) (2007).
- [59] Olkhovets, A., Hsu, R. C., Lipovskii, A., and Wise, F. W. *Physical Review Letters* **81**(16), 3539–3542 (1998).
- [60] Kim, D., Kuwabara, T., and Nakayama, M. *Journal of Luminescence* **119-120**, 214 – 218 (2006).
- [61] Sanguinetti, S., Poliani, E., Bonfanti, M., Guzzi, M., Grilli, E., Gurioli, M., and Koguchi, N. *Physical Review B* **73**, 125342 (2006).
- [62] Fomin, V. M., Gladilin, V. N., Devreese, J. T., Pokatilov, E. P., Balaban, S. N., and Klimin, S. N. *Physical Review B* **57**(4), 2415–2425 (1998).
- [63] Peterson, J. J. and Krauss, T. D. *Nano Letters* **6**(3), 510–514 (2006).
- [64] Uskov, A. V., Jauho, A. P., Tromborg, B., Mork, J., and Lang, R. *Physical Review Letters* **85**(7), 1516–1519 (2000).
- [65] Zhang, L. G., Shen, D. Z., Fan, X. W., and Lu, S. Z. *Chinese Physics Letters* **19**(4), 578–580 (2002).
- [66] Klem, E. J. D., Shukla, H., Hinds, S., MacNeil, D. D., Levina, L., and Sargent, E. H. *Applied Physics Letters* **92**(21) (2008).
- [67] Flores-Acosta, M., Sotelo-Lerma, M., Arizpe-Chavez, H., Castellon-Barraza, F. F., and Ramirez-Bon, R. *Solid State Communications* **128**(11), 407–411 (2003).
- [68] Meli, L. and Green, P. F. *ACS Nano* **2**(6), 1305–1312 (2008).

- [69] Hanrath, T., Veldman, D., Choi, J. J., Christova, C. G., Wienk, M. M., and Janssen, R. A. J. *ACS Applied Materials & Interfaces* **1**(2), 244–250 (2009).
- [70] Turyanska, L., Elfurawi, U., Li, M., Fay, M. W., Thomas, N. R., Mann, S., Blokland, J. H., Christianen, P. C. M., and Patane, A. *Nanotechnology* **20**(31), 315604 (2009).
- [71] Cho, K.-S., Talapin, D. V., Gaschler, W., and Murray, C. B. *Journal of the American Chemical Society* **127**(19), 7140–7147 (2005).
- [72] Prasad, B. L. V., Stoeva, S. I., Sorensen, C. M., and Klabunde, K. J. *Chemistry of Materials* **15**(4), 935–942 (2003).
- [73] Liu, C., Kwon, Y. K., and Heo, J. *Chemical Physics Letters* **452**(4-6), 281–284 (2008).
- [74] Lewis, J. E., Wu, S., and Jiang, X. J. *Nanotechnology* **21**(45) (2010).
- [75] Umezu, I., Ogawa, T., and Arai, T. *Japanese Journal of Applied Physics Part 1-Regular Papers Brief Communications & Review Papers* **28**(3), 477–483 (1989).
- [76] An, J. M., Franceschetti, A., and Zunger, A. *Nano Letters* **7**(7), 2129–2135 (2007).
- [77] Fradkin, L., Langof, L., Lifshitz, E., Gaponik, N., Rogach, A., Eychmuller, A., Weller, H., Micic, O. I., and Nozik, A. J. *Physica E-Low-Dimensional Systems & Nanostructures* **26**(1-4), 9–13 (2005).
- [78] Johnston-Halperin, E., Awschalom, D. D., Crooker, S. A., Efros, A. L., Rosen, M., Peng, X., and Alivisatos, A. P. *Physical Review B* **63**(20), 205309 (2001).

- [79] Klotz, F., Jovanov, V., Kierig, J., Clark, E. C., Rudolph, D., Heiss, D., Bichler, M., Abstreiter, G., Brandt, M. S., and Finley, J. J. *Applied Physics Letters* **96**(5), 053113 (2010).
- [80] Kleemans, N., van Bree, J., Bozkurt, M., van Veldhoven, P. J., Nouwens, P. A., Notzel, R., Silov, A. Y., Koenraad, P. M., and Flatte, M. E. *Physical Review B* **79**(4), 045311 (2009).
- [81] Zutic, I., Fabian, J., and Das Sarma, S. *Reviews of Modern Physics* **76**(2), 323–410 (2004).
- [82] Lee, S., Yang, S. R. E., Dobrowolska, M., and Furdyna, J. K. *Semiconductor Science and Technology* **19**(9), 1125–1130 (2004).
- [83] Dyakonov, M. I. *Physica E-Low-Dimensional Systems & Nanostructures* **35**(2), 246–250 (2006).
- [84] Walsh, A. *Proceedings of the Royal Society A-Mathematical Physical and Engineering Sciences* **467**(2131), 1970–1985 (2011).
- [85] Woods, L. M., Reinecke, T. L., and Lyanda-Geller, Y. *Physical Review B* **66**(16) (2002).
- [86] Miura, N., Matsuda, Y. H., Uchida, K., and Arimoto, H. *Journal of Physics-Condensed Matter* **11**(31), 5917–5928 (1999).
- [87] Furis, M., Hollingsworth, J. A., Klimov, V. I., and Crooker, S. A. *The Journal of Physical Chemistry B* **109**(32), 15332–15338 (2005).
- [88] Wijnen, F. J. P., Blokland, J. H., Chin, P. T. K., Christianen, P. C. M., and Maan, J. C. *Physical Review B* **78**, 235318 (2008).
- [89] Chamarro, M., Gourdon, C., and Lavallard, P. *Journal of Luminescence* **70**, 222–237 (1996).

- [90] Langof, L., Fradkin, L., Ehrenfreund, E., Lifshitz, E., Micic, O., and Nozik, A. *Chemical Physics* **297**(1-3), 93 – 98 (2004).
- [91] Bernick, R. and Kleinman, L. *Solid State Communications* **8**(7), 569 – 575 (1970).
- [92] Schaller, R. D., Crooker, S. A., Bussian, D. A., Pietryga, J. M., Joo, J., and Klimov, V. I. *Physical Review Letters* **105**, 067403 Aug (2010).
- [93] Rinaldis, S. D., Rinaldi, R., Cingolani, R., D’Amico, I., Biolatti, E., and Rossi, F. *Physica E: Low-dimensional Systems and Nanostructures* **13**(2-4), 624 – 629 (2002).
- [94] Middleton, A. A. and Wingreen, N. S. *Physical Review Letters* **71**(19), 3198–3201 Nov (1993).
- [95] Fan, H., Yang, K., Boye, D. M., Sigmon, T., Malloy, K. J., Xu, H., Lapez, G. P., and Brinker, C. J. *Science* **304**(5670), 567–571 (2004).
- [96] Roux, S. and Herrmann, H. J. *EPL (Europhysics Letters)* **4**(11), 1227 (1987).
- [97] Ancona, M. G., Kruppa, W., Rendell, R. W., Snow, A. W., Park, D., and Boos, J. B. *Physical Review B* **64**(3), 033408 Jun (2001).
- [98] Romero, H. E. and Drndic, M. *Physical Review Letters* **95**(15) (2005).
- [99] Ou, Y. C., Cheng, S. F., and Jian, W. B. *Nanotechnology* **20**(28) (2009).
- [100] Bargeman, D. and Vader, F. V. V. *Journal of Electroanalytical Chemistry* **37**, 45 – 52 (1972).
- [101] Damos, F. S., Luz, R. C. S., and Kubota, L. T. *Langmuir* **21**(2), 602–609 (2005).

- [102] Murgatroyd, P. N. *Journal of Physics D-Applied Physics* **3**(2), 151 (1970).
- [103] Simmons, J. G. *Physical Review* **155**, 657–660 (1967).
- [104] Woellner, C. F. and Freire, J. A. *Journal of Chemical Physics* **134**(8) (2011).
- [105] Leatherdale, C. A., Kagan, C. R., Morgan, N. Y., Empedocles, S. A., Kastner, M. A., and Bawendi, M. G. *Physical Review B* **62**(4), 2669–2680 (2000).
- [106] Gratzel, M. *Journal of Photochemistry and Photobiology C-Photochemistry Reviews* **4**(2), 145–153 (2003).
- [107] Sargent, E. H. *Advanced Materials* **20**(20), 3958–3964 (2008).
- [108] Koleilat, G. I., Levina, L., Shukla, H., Myrskog, S. H., Hinds, S., Pattantyus-Abraham, A. G., and Sargent, E. H. *ACS Nano* **2**(5), 833–840 (2008).
- [109] Anthony, John, W., Bideaux, R. A., Bladh, K. W., and Nichols, M. C. *Handbook of Mineralogy*. (2004).
- [110] Breckenridge, R. G. and Hosler, W. R. *Physical Review* **91**(4), 793–802 (1953).
- [111] Solis, D., Viguera-Santiago, E., Hernandez-Lopez, S., Gomez-Cortes, A., Aguilar-Franco, M., and Camacho-Lopez, M. A. *Science and Technology of Advanced Materials* **9**(2) (2008).
- [112] Ginger, D. and Greeham, N. *Semiconductor and Metal Nanocrystals: Synthesis and Electronic and Optical Properties*, chapter Electrical Properties of Semiconductor nanocrystals synthesis and Electronic and optical properties, 239–284. New York: Marcel Dekker, Inc. (2004).

- [113] Weller, H. *Advanced Materials* **5**(2), 88–95 (1993).
- [114] Pattantyus-Abraham, A. G., Kramer, I. J., Barkhouse, A. R., Wang, X., Konstantatos, G., Debnath, R., Levina, L., Raabe, I., Nazeeruddin, M. K., Gratzel, M., and Sargent, E. H. *ACS Nano* **4**(6), 3374–3380 (2010).
- [115] Sze, S. M. *Semiconductor Devices, Physics and Technology*. John Wiley & Sons, Ltd, (1985).
- [116] Konenkamp, R. *Physical Review B* **61**(16), 11057–11064 (2000).
- [117] Seto, J. Y. W. *Journal of Applied Physics* **46**(12), 5247–5254 (1975).
- [118] Yu, D., Wang, C. J., Wehrenberg, B. L., and Guyot-Sionnest, P. *Physical Review Letters* **92**(21) (2004).
- [119] Morigaki, K. *Physics of amorphous semiconductors*. World Scientific Publishing Company, (1999).
- [120] Yildiz, A., Lisesivdin, S., Kasap, M., and Mardare, D. *Journal of Non-Crystalline Solids* **354**(45-46), 4944 – 4947 (2008).
- [121] Tang, J., Brzozowski, L., Barkhouse, D. A. R., Wang, X., Debnath, R., Wolowiec, R., Palmiano, E., Levina, L., Pattantyus-Abraham, A. G., Jamakosmanovic, D., and Sargent, E. H. *ACS Nano* **4**(2), 869–878 (2010).